

UNIVERSITY OF TRENTO
DOCTORAL SCHOOL IN CIVIL, ENVIROMENTAL AND
MECHANICAL ENGINEERING

XXX cycle



**Design and Microfabrication of Multifunctional
Bio-Inspired Surfaces**

PhD candidate: Simone Ghio

Supervisors: Nicola M. Pugno, Maurizio Boscardin

Submitted in partial fulfilment of the requirements
of the degree of Doctor of Philosophy, 2018.

Abstract

In this thesis, we used CMOS-like technologies to produce improved, hierarchical multifunctional bioinspired surfaces. Different natural surfaces have been surveyed including well-known lotus leaf, sharkskin, back of the Namib Desert beetle, butterfly wings, and legs of water-walking insects. The lotus leaf features superhydrophobicity, which leads to low adhesion and self-cleaning. Sharkskin is composed of ripples that manage to reduce skin-friction and thus drag resistance. The Namib Desert beetle, harvests water from the heterogeneous pattern having hydrophilic/hydrophobic bumps on his back. Butterfly wings have re-entrant structures that manage to reach superhydrophobicity from a hydrophilic substrate. Hairy legs of water-walking insects are superhydrophobic with low adhesion that allows them to fight and jump on water.

In chapter 1, we have undertaken a review of bioinspired surfaces that emulate the abilities of such natural surfaces.

Then, in chapter 2 we have described the innovative CMOS-like techniques used for generating several hierarchical and re-entrant microstructures.

Chapter 3 depicts the analysis of surfaces with hierarchical structures generated with a fast and easy process; this latter forms a second hierarchical level composed of random

pyramidal elements using wet etching. Surfaces realized with this process manage to reach remarkably high contact angle and low contact angle hysteresis. Additionally, in this chapter we have introduced an analytical model to study the stability of Cassie-Baxter state over Wenzel state for these hierarchical surfaces.

In chapter 4 the fabrication and analysis of surfaces composed of controlled hierarchical levels, which combine sharkskin with single-level lotus leaf-inspired pillared structures are reported. These particular hierarchical surfaces are demonstrated to hold high superhydrophobic properties along with low skin-friction. The superhydrophobicity of these surfaces has been characterized in a series of tests on an inclined plane. The data extrapolated from this measurement was used to evaluate the total dissipated energy of the sliding drop. Combining the data collected during this experiment with contact angle and contact angle hysteresis measurements we propose a global parameter that evaluates the superhydrophobic “level” of a surface.

Furthermore, in chapter 5 similar hierarchical surfaces have also been tested for water harvesting together with single-level pillared surfaces that feature heterogeneous chemistry with hydrophilic/hydrophobic spot on every single pillar.

In chapter 6 a series of tests have also been performed on butterfly-inspired surfaces. Although the substrate of such surfaces is hydrophilic, thanks to the re-entrant structures the surfaces reach high level of hydrophobicity. An implemented mathematical model and experimental test confirm the stability of this hydrophobic state.

In chapter 7, we describe two sets of surfaces inspired by the hairy legs of water walking insect the first is composed of stretchable pyramidal-pillars and the second of truncated-conical silicon pillars. The ability of sharp structures to easily detach from water surfaces is exploited to change the contact angle value of a water drop deposited on this fast type of stretchable micropatterned surface. A mathematical model has been implemented and experimental tests have been carried out to evaluate the stability of the water-air composite interface on both types of microstructured surfaces. In particular, in the polymeric surfaces elasto-capillarity seems to influence the metastability of the Cassie-Baxter state.

Aknoledgements

The work presented in this thesis would not have been possible without the support of many people. First, I would like to thank my supervisors, Professor Nicola M. Pugno and Maurizio Boscardin, who helped and supported me throughout my PhD studies. I would like to thank my friend and colleague Eugeny Demenev that helped improving my researches with his expertise and patience. I also would like to thank many lab and office mate at the Fondazione Bruno Kessler.

Furthermore, I would like to express gratitude to my entire family who has encouraged and supported me during these last three years, and my love to my life partner Tiffany Paulin and my two kids.

Table of Contents

1	Bioinspired surfaces.....	11
1.1	INTRODUCTION	11
1.2	SUPERHYDROPHOBIC SURFACES	12
1.2.1	<i>Contact angle and contact angle hysteresis</i>	<i>12</i>
1.2.2	<i>Contact angle predictions.....</i>	<i>15</i>
1.2.3	<i>Stability of intrinsically hydrophobic surface</i>	<i>18</i>
1.2.4	<i>Stability of intrinsically hydrophilic surfaces.....</i>	<i>22</i>
1.3	DRAG REDUCTION	23
1.4	WATER HARVESTING	28
2	Hierarchical microfabrication techniques	33
2.1	INTRODUCTION	33
2.2	NON-HIERARCHICAL STRUCTURE FABRICATION	33
2.2.1	<i>Initial Cleaning</i>	<i>33</i>
2.2.2	<i>Thermal Oxidation.....</i>	<i>34</i>
2.2.3	<i>Lithography.....</i>	<i>36</i>
2.2.4	<i>Dry Etches.....</i>	<i>39</i>
2.2.5	<i>Scanning Electron Microscopy</i>	<i>47</i>
2.2.6	<i>Hydrophobic chemical coating.....</i>	<i>47</i>
2.3	SOFT STRUCTURES FABRICATION.....	48
2.4	HIERARCHICAL STRUCTURES FABRICATION.....	49
2.4.1	<i>Wet Etch Hierarchical surfaces</i>	<i>50</i>
2.4.2	<i>Two Steps Lithography Hierarchical surfaces</i>	<i>52</i>
2.4.3	<i>Re-entrant structure.....</i>	<i>55</i>
2.4.4	<i>Cyclic re-entrant structures.....</i>	<i>59</i>
3	Hierarchical surfaces for improving wetting	62
3.1	ABSTRACT	62
3.2	INTRODUCTION	63

3.3	EXPERIMENTAL ANALYSIS	66
3.3.1	<i>Surface generation</i>	67
3.4	WETTABILITY ANALYSIS	69
3.4.1	<i>Non-hierarchical pillars</i>	70
3.4.2	<i>Hierarchical pillars</i>	74
3.5	THEORETICAL ANALYSIS	77
3.5.1	<i>Non-hierarchical pillars</i>	77
3.5.2	<i>Hierarchical pillars</i>	79
3.6	RESULTS AND DISCUSSION	90
3.7	CONCLUSION	94
4	Combining sharkskin and lotus leaf ability	96
4.1	ABSTRACT.....	96
4.2	INTRODUCTION	97
4.3	MATERIALS AND METHODS.....	98
4.4	RESULTS.....	109
4.5	DISCUSSION	116
4.6	CONTACT ANGLE VARIATION ON DIRECTIONAL PATTERNS	138
4.7	CONCLUSION	142
5	Homogeneous hydrophobic/hydrophilic surfaces for water harvesting	
	144	
5.1	ABSTRACT.....	144
5.2	INTRODUCTION	144
5.3	MATERIALS AND METHODS	147
5.4	RESULTS.....	155
5.4.1	<i>Contact angle</i>	155
5.4.2	<i>Contact angle hysteresis</i>	157
5.4.3	<i>Dynamics of moving drops</i>	159

5.4.4	<i>Harvesting</i>	168
5.5	CONCLUSION	171
6	From Hydrophilic to Superhydrophobic.....	173
6.1	ABSTRACT	173
6.2	INTRODUCTION	173
6.3	EXPERIMENTAL PROCESSES.....	176
6.3.1	<i>Surface Fabrication</i>	177
6.3.2	<i>Wettability test</i>	179
6.4	THEORY PREDICTION AND ANALYSIS	179
6.5	RESULTS	182
6.6	THEORETICAL DISSERTATION	185
6.6.1	<i>Flat-topped cylindrical pillars.....</i>	<i>185</i>
6.6.2	<i>Textured hierarchical pillars</i>	<i>186</i>
1.1.1	<i>Butterfly re-entrant inspired structures.....</i>	<i>187</i>
6.6.3	<i>Experimental test.....</i>	<i>191</i>
6.6.4	<i>Butterfly inspired wear test</i>	<i>192</i>
6.7	MUSHROOMS LIKE RE-ENTRANT SURFACES	198
6.8	CONCLUSIONS.....	202
7	Water-walking-like tuneable surfaces	203
7.1	ABSTRACT	203
7.2	INTRODUCTION	203
7.3	POLYDIMETHYLSILOXANE SAMPLES WITH PYRAMIDAL PILLARS.	206
7.3.1	<i>Samples Preparation</i>	<i>206</i>
7.3.2	<i>Wettability test under stretch condition.....</i>	<i>208</i>
7.3.3	<i>Data analysis of pyramidal soft pillars</i>	<i>209</i>
7.3.4	<i>Stability of pyramidal pillars</i>	<i>212</i>
7.4	SMALL ANGLE SPIKES.....	215
7.4.1	<i>Stability of spikes pillars</i>	<i>216</i>
7.4.2	<i>Data analysis of spike pillars.....</i>	<i>218</i>
7.5	CASSIE-WENZEL TRANSITION THROUGH COMPRESSION.....	223

7.5.1	<i>Compression of PDMS pyramidal pillars</i>	225
7.5.2	<i>Compression of silicon low angle spikes.....</i>	227
7.6	CONCLUSION	229
8	Conclusion	230
8.1	ARTIFICIAL SURFACES	231
8.1.1	<i>Lotus leaf-inspired random hierarchical surfaces.....</i>	231
8.1.2	<i>Lotus leaf-inspired deterministic hierarchical surfaces..</i>	232
8.1.3	<i>Sharkskin-inspired structures</i>	232
8.1.4	<i>Hierarchical combination of sharkskin and single-level lotus leaf surfaces.....</i>	232
8.1.5	<i>Namib Desert beetle-inspired surfaces, with heterogeneous chemistry</i>	233
8.1.6	<i>Butterfly-inspired surfaces, with re-entrant structures..</i>	234
8.1.7	<i>Water walking-inspired stretchable surfaces, with pyramidal-like structures</i>	235
8.1.8	<i>Water walking-inspired surfaces, with truncated-conical silicon structures.....</i>	235
8.2	OUTLOOK AND FUTURE WORK.....	236
9	References	237

1 Bioinspired surfaces

1.1 Introduction

Plants, insect, and animals had adapted for millennia to survive in their ambient. A peculiar result of this evolution is the development of micropatterned surfaces that, combined with specific chemistry, show peculiar properties in contact with water. It exists a growing and broad interest in the use of such properties for the development of bioinspired surfaces. In particular, those that show specific properties in contact with liquids: superhydrophobicity/oleophobicity, low-drag resistance, and water harvesting. Ability to control and tune specific properties of a surface plays a fundamental role in many practical applications: from a self-cleaning window to a low flow resistant drone. This Chapter focuses on the properties and characteristics of bioinspired surfaces, which reproduce natural structures in order to enhance physical properties of synthetic surfaces. Superhydrophobic properties are present in several plants [1] and insects [2]. A typical example of a low-drag resistance surface is inevitably the sharkskin. The darkling beetle, on the other hand, harvests water from morning fog in the Namib Desert thanks to a remarkable combination of hydrophobic and hydrophilic structures on its back.

1.2 Superhydrophobic surfaces

The potential widespread interest of superhydrophobicity on industrial applications has driven the application research effort in this area. Current effort targets to improve reliability and manufacturability for a cost-effective industrialization of such materials. A car windshield that can be cleaned and allows to see perfectly during heavy rain, a pair of gloves that can be immersed in mud and come out clean as new, or even a boat hull that does not need to be cleaned from biofouling and molluscs, are examples of near-to-market products based on superhydrophobic materials. The research effort that can bring the fabrication technology to a mature phase needs to address the fundamental characteristics that define a surface to be superhydrophobic: contact angle (static and hysteresis), and the stability of intrinsically hydrophobic and hydrophilic substrates.

1.2.1 Contact angle and contact angle hysteresis

Contact angle (CA) and contact angle hysteresis are direct expressions of the wettability of a surface. A surface is defined superhydrophobic if the contact angle is greater than 150° [3] and its hysteresis is low. This means that a small drop deposited on a superhydrophobic surface will have a quasi-perfect spherical shape and great mobility. We learned from the natural

world that superhydrophobicity can only arise from a precise combination of substrate chemistry and surface roughness.

Since a perfectly smooth and flat surface cannot exceed at best 120° of contact angle value, micro-patterning is fundamental in order to attain the required threshold of hydrophobicity.

The physical limitation of contact angle value is given by the Young equation, a thermodynamic equilibrium between the vapour, solid, and liquid phase at the triple line. This equilibrium defines the contact angle value for flat surfaces:

$$\cos\theta = \frac{\gamma_{SV} - \gamma_{SL}}{\gamma_{LV}} \quad (1)$$

Where represents the interfacial surface tension and S, L, and V stands for solid, liquid, and vapour phase. Surfaces with contact angle values greater than 90° are considered hydrophobic, while surfaces with contact angle values lower than 90° are considered hydrophilic. Figure 1 illustrates the contact angle of a drop deposited on a flat hydrophobic or hydrophilic surface, measured between the liquid-solid interface and the vapour-liquid interface at the triple line (Solid-Liquid-Vapour).

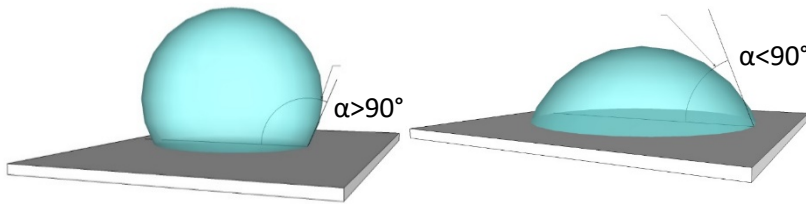


Figure 1: From left to right: drop deposited on a hydrophobic flat surface and a hydrophilic flat surface. Surfaces are considered hydrophobic if the contact angle is higher than 90° and hydrophilic if the contact angle is lower.

The use of a steady state condition, where a drop is gently deposited on the surface, allows for the measurement of the so-called static contact angle. Such method is commonly called sessile drop, and the value of the angle can be estimated from the processing of an optical image of the drop, using commonly available commercial evaluation kits or open-source software. The value of the static contact angle for a flat surface is close to Young's contact angle. The mobility of a drop deposited on the surface allows for the quantification of a dynamic contact angle. This measurement is based on the principle that when the deposited drop changes its volume, the contact area adjusts

accordingly. However, this procedure needs to account for the hysteresis during the triple line advancing or receding movement. This hysteresis can be evaluated through the advancing (ϑ_a) and receding (ϑ_r) dynamic contact angles, where the advancing CA is always greater than the static contact angle and the receding always smaller. These angles are measured by observing both the growth and shrinking of a drop on the surface under test. Advancing contact angle represents the largest possible angle at which the drop can be found on the surface, while the receding CA refers to the smaller. To express the adhesion of a drop on a surface, we use the contact angles' hysteresis, defined as the difference between advancing and receding contact angle $\Delta\vartheta = \vartheta_a - \vartheta_r$ [4]–[6], or more commonly the difference between the cosine of the two angles $\Delta\cos\vartheta = \cos\vartheta_r - \cos\vartheta_a$ [7]–[12]. The use of confocal microscopes allowed to demonstrate that the advancing angle of drops on superhydrophobic surfaces, at the microscale, it is always 180° [10], [13], [14]. The equation for the contact angle hysteresis becomes $\Delta\cos\vartheta = \cos\vartheta_r + 1$, hence drop adhesion on the surface depends only on receding angle.

1.2.2 Contact angle predictions

As stated before, the thermodynamic contact angle cannot become larger than $\sim 120^\circ$ [15]. As a consequence, the production of a superhydrophobic surface combines the

chemical properties of the substrate with a precise micro or even nanopatterning. The contact angle measured on micro-structured surface is called apparent contact angle, and its validity range on the models used to predict contact angle is limited by the dimension of the drop radius in respect to the specific roughness of the surfaces [16], [17]; recent work shows how to adapt this theory to small drops [18].

Theoretical equations able to predict the apparent contact angle have been developed by Wenzel and Cassie-Baxter. Wenzel equation predicts the contact angle value in case of impalement of the drop on the micropattern, there is full wetting of the surface below the drop [19], [20].

$$\cos \vartheta_w = r \cos \vartheta \quad (2)$$

In this condition, the surface cannot be considered superhydrophobic since the contact angle hysteresis is high. On the contrary Cassie-Baxter equation predicts the contact angle for a heterogeneous media.

$$\cos \vartheta_c = f_1 \cos \vartheta_1 - f_2 \cos \vartheta_2 \quad (3)$$

Hence, if the drop lays in fakir-like state, floating over the micropatterned structure, the apparent contact angle can be predicted by this equation. The original Cassie-Baxter equation

was developed in order to predict the apparent contact angle value over a textile surface. When the drop sees different media, this equation allows to compute the contact angle as a function of the fraction of these media [21], where f_1 and f_2 are area fraction of each phase; $f_1 + f_2 = 1$, and the thermodynamic contact angles are ϑ_1 and ϑ_2 . When the drop is in fakir state on the asperities, the surface is homogenous, and of the phase is air, $\vartheta_2 = 180^\circ$. In these conditions, the previous equation becomes:

$$\cos \vartheta_c = f(1 + \cos \vartheta) - 1 \quad (4)$$

Where $\vartheta = \vartheta_1$ is the thermodynamic contact angel of solid phase, and $f = f_1$ is the solid/liquid area fraction.

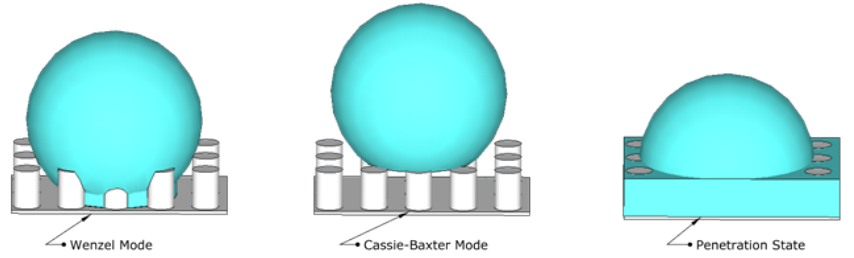


Figure 2: From left to right: drop find in the impaled state (Wenzel), the fakir state (Cassie-Baxter), and the penetration state (hemi-wicking). The images are schematic, as a matter of fact, the drop dimension has to be much larger than the pillars

diameter. The picture for clarity purpose use similar size for pillars and drop radius.

For hydrophilic rough surfaces, the water can be absorbed in the asperity of the surface. This phenomenon is called hemi-wicking [22] and consists in a progressive imbibition of the surface from the deposited drop [23], [24]. The equation that describes this state is similar to Cassie-Baxter equation, and both apply to the scenario of an air-water interface.

$$\cos \theta_p = f \cos \theta + 1 - f \quad (5)$$

where θ_p is the apparent contact angle for the penetration mode. Fixing a geometry and ideally sweeping the base contact angle of the substrate from 0 to π , the surfaces would be first in penetrate mode, then at Wenzel and finally in Cassie-Baxter [18]. Several works address the stability of these states [25]–[27].

1.2.3 Stability of intrinsically hydrophobic surface

The drop can be in Cassie-Baxter mode even if Wenzel mode has lower energy, and in this case, the Cassie-Baxter is a metastable state. This is not the case of intrinsically hydrophilic surfaces, which have Young contact angle lower than $\pi/2$. Such surfaces can reach superhydrophobicity thanks to re-entrant structures [28], [29]. Cassie-Baxter to Wenzel transition has different

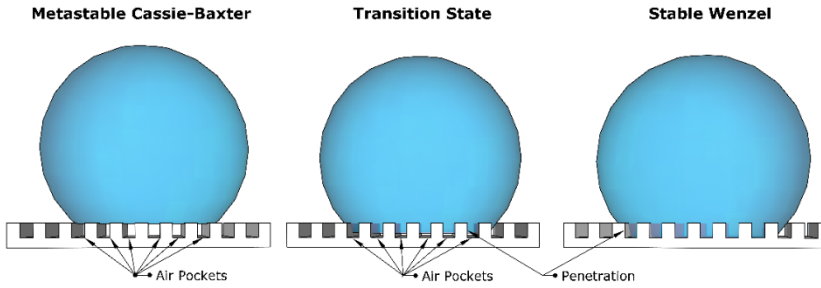
mechanisms if the substrate is intrinsically hydrophilic or hydrophobic. In the case of an intrinsically hydrophobic surface, the air pockets under the drop are stable only if the energy variation associated with Cassie-Baxter state is lower than the one associated with Wenzel state. This leads to a relationship between Young contact angle, the roughness of the surface and solid-liquid area fraction [22]:

$$\cos \vartheta_{yt} < \frac{f - 1}{r - f} \quad (6)$$

Equation 6 describes, for a given geometry, the value of the Young CA that the substrate needs to reach in order to have thermodynamically stable Cassie-Baxter state. If $\pi/2 < \vartheta_y < \vartheta_{yt}$ Cassie-Baxter state is not an absolute but a local minimum: the composite interface is metastable, and as a matter of fact, multiple Gibbs local energy minima exist [30]. In the case of metastable superhydrophobicity, the Cassie-Baxter state is the higher of the local Gibbs energy minima [31], [32]. To be thermodynamically stable, the drop needs to overcome the energy barrier that separates it from energy minima [33]–[37]. The drop have to pass from Cassie-Baxter to Wenzel mode through an energy maximum, which corresponds to a composite state where the asperities are almost completely filled with water and the liquid-air interface under the drop still exists. Under this hypothesis, it is possible to estimate the value of the

energy to estimate for a drop of contact area length a deposited on a simple geometry composed of parallel strips of pitch distance l and height h [38] as:

$$W_{barrier} = 2\pi a^2 \frac{h}{l} (\gamma_{SL} - \gamma_{SA}) = -2\pi a^2 \frac{h}{l} \gamma_{LA} \cos \vartheta_y \quad (7)$$



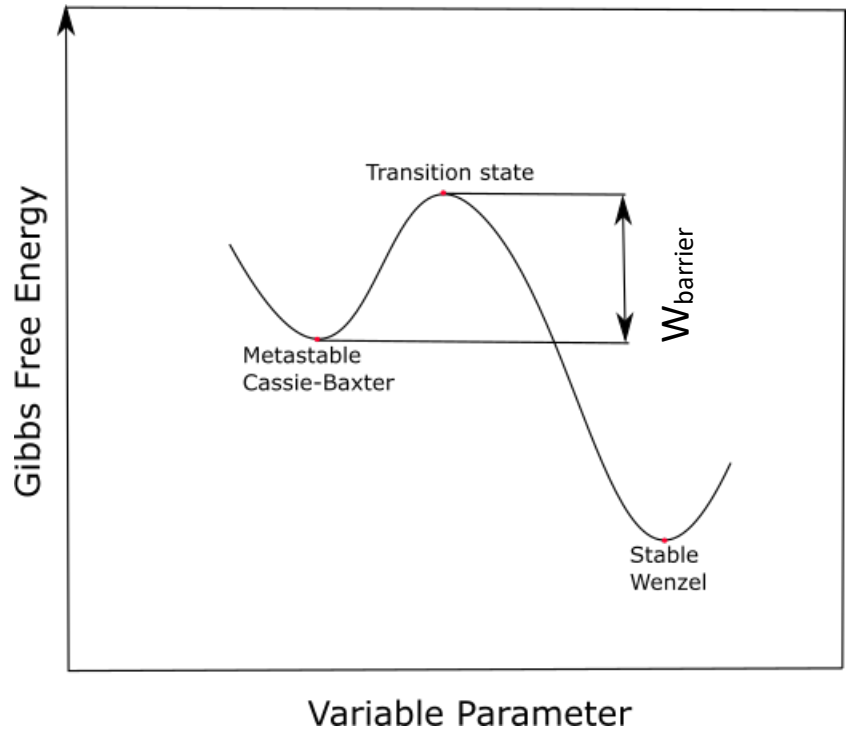


Figure 3: The graph shows a schematic image of metastable Cassie-Baxter state and stable Wenzel state; W_{barrier} corresponds to the energy barrier to overcome to jump from meta-stability to stability for intrinsic hydrophobic surfaces. Top images show the condition in which the drop is found at different moments of the transition.

To overcome this energy barrier a variety of methods are were previously proposed: drop bouncing on the surface [39]–[41], evaporation[42]–[44], vibration [25], and even pressure [45].

The sketch of Gibbs energies in Figure 3 shows the asymmetry of existing between the two minima. As a matter of fact, the energy barrier to pass from stable to metastable state has been demonstrated to be one order of magnitude greater than W_{barrier} [32]. The probability of a reverse transition from stable Wenzel to metastable Cassie-Baxter is close to zero, showing the irreversibility of the process. In contrast, if Cassie-Baxter is stable a Wenzel to Cassie-Baxter transition can be performed [25].

1.2.4 Stability of intrinsically hydrophilic surfaces

It is possible to realize superhydrophobic surfaces from intrinsically hydrophilic surfaces [23], [46]. The stability of such surfaces cannot be addressed with the theory used for hydrophobic substrates. In fact, if a cosine of the Young angle for a hydrophilic surface, $0 \leq \vartheta_y \leq \pi/2$, is insert in equation (7), the energy barrier is lower than zero. Hence Wenzel state it always energetically favorable for intrinsically hydrophilic surfaces. Superhydrophobic surfaces can arise from hydrophilic substrate

thanks to the specific geometry of the structures that compose the surface.

The formulation of theoretical analysis and experimental comparison of intrinsically hydrophilic substrates with re-entrant cavity have been already studied elsewhere [47], but this formulation cannot be applied at re-entrant pillars since the base of this theory is air trapping. The problem of pillars with intrinsically hydrophilic substrate have been approached by other authors: surfaces with microscopic spheres [48], or with re-entrant structures [49]. The curvature of such structures generates an energy barrier between the metastable Cassie-Baxter state and the stable Wenzel. These phenomena will be discussed in more detail in Chapter 6.

Similar concepts are exploited for superoleophobic surfaces; low-surface-energy liquid is repelled by intrinsically oleophilic ($\vartheta_Y < 90^\circ$) surfaces thanks to peculiar shape of the pillars that compose it [50], [51].

1.3 Drag reduction

Superhydrophobic surfaces have the peculiar feature of having a gas cushion under the liquid; this property results in self-cleaning, low adhesion, and high mobility of the drop over a dry surface. Furthermore, this property helps to reduce skin friction of fluid moving on the surface. In the process the liquid next to

surface behaves as viscous and generates friction [52], hydrophilic flat surfaces are considered having a no-slip condition: the velocity of a fluid in contact with the surface is zero. The no-slip condition increases the shear stress at the wall, and consequentially influences drag. The air trapped between the structure that composes a superhydrophobic surface generates a zero shear stress region, perfect slip, that can considerably reduce skin friction drag [53], [54]. Particular attention in designing these structures can avoid a condition in which the air bubbles protrude in the liquid and interfere with the flow enhancing drag instead of reducing it [55]. Several studies show that there is a no-slip condition on hydrophilic flat surfaces [56], [57], and also this condition is absent on hydrophobic flat surfaces [58], [59]. Slip condition on hydrophobic flat surfaces seems to be linked with the presence of air bubble trapped on the surface [60]–[62].

A completely different mechanism is used by fast swimming shark to reduce skin friction. The skin of the shark is completely covered with riblets that can reduce the friction at high velocities (turbulent flow). The first studies to consider the riblets of shark skin for drag reduction were performed in the eighties [63], [64].

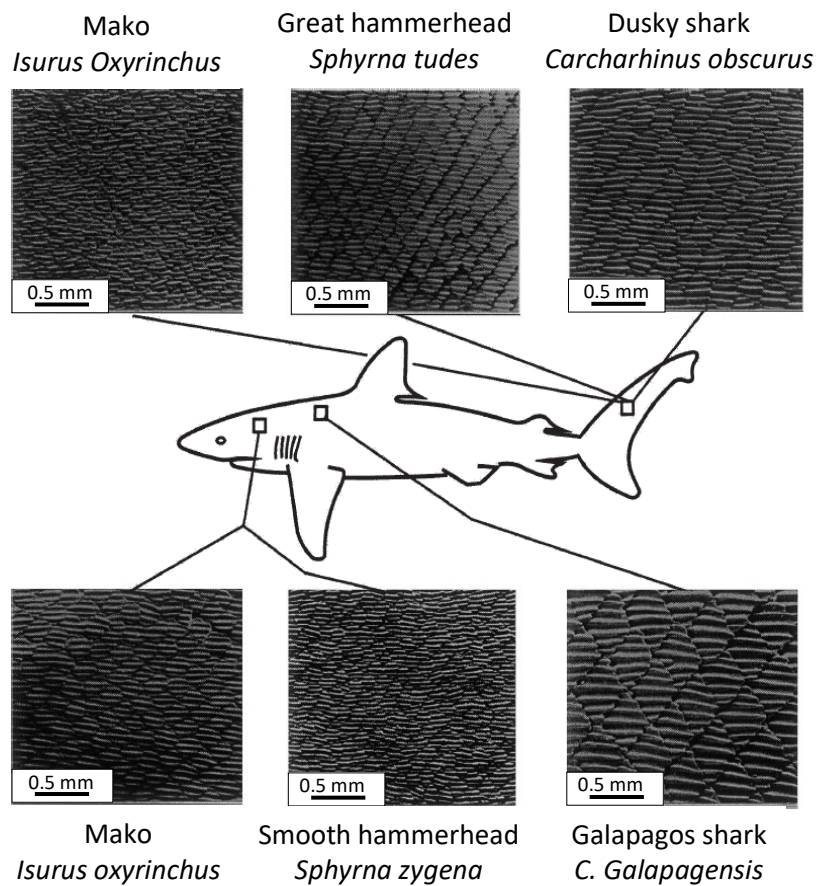


Figure 4: Scale of patterns in fast-swimming shark, adapted from [63].

A fully developed turbulent flow can be analyzed dividing it into two distinct regions: the viscous sublayer (the closest to the wall) and the outer layers. The velocity distribution in the outer layer is chaotic, while in the viscous sublayer a defined pattern of velocities can be observed. On a flat surface, the viscous sublayer has single velocities that diverge significantly to respect the mean flow direction [52]. A normal exchange between the low-velocity region next to the wall and the high velocity in the outer layer enhance the shear stress that results in skin friction. These exchanges generate vortices that require movement also in the direction perpendicular to the fluid motion. Sharkskin peculiar structure (riblets aligned to mean flow velocity) manages to channel this momentum transfer in the flow direction.

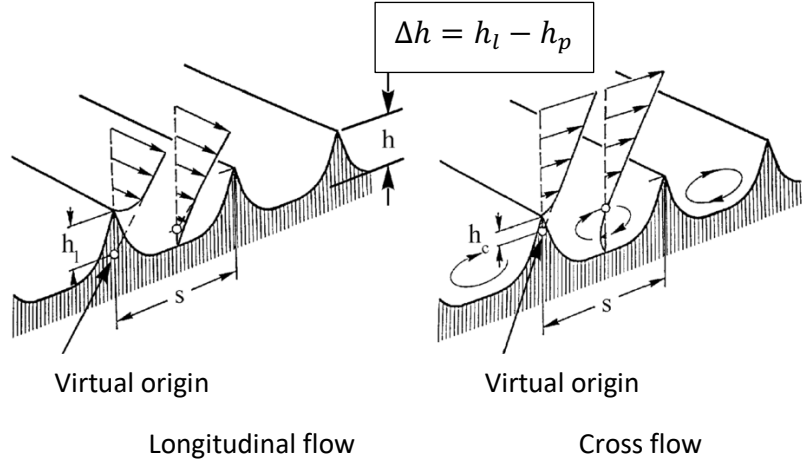


Figure 5: Schematic representation of fluid-flow parallel or perpendicular to the riblets, adapted from [52].

To explain the channelling of the different velocities on the mean flow direction one has to consider what happens in the viscous sublayer in the case of a flow longitudinal and perpendicular to riblets direction. Thanks to the viscous theory has been demonstrated that riblet surfaces appear to the flow as a smooth surface located above the real surface, Figure 5. For longitudinal flow, the origin is located further from the surface of riblets tip than for perpendicular flow. This situation generates a height difference between the two virtual surfaces: $\Delta h = h_l - h_p$. Due to this difference, the vortex generated by flux exchanges in vertical direction will experience greater

resistance to move laterally in respect the riblets direction than longitudinally [52]. It has been demonstrated experimentally that sharkskin replica reduce drag even in laminar flow [65], especially if the skin replica is coated with hydrophobic layer [66].

1.4 Water harvesting

Biological species that live in environments with low availability of liquid-phase water have potentiated mechanisms of water harvesting from air humidity. Water harvesting is particularly challenging because of the contrasting properties that are required to the surfaces. A hydrophilic surface is required for an efficient nucleation of liquid on the surface, and a rapid growth of the nucleated drop [67]. A superhydrophobic surface is then required to make easily slide down the drop to the reservoir. An interesting solution to this problem has been explored by the darkling beetle. This species is native to the Namib Desert, South Africa. In an area characterized by strong wind and fog condition [68], the darkling beetle manages to harvest the fogs on its forewings, and directs the collected water to its mouth to drink it [69], [70]. This is achieved by a particular pattern of the beetles back, which is covered with hydrophilic bumps. The surface between the bumps is superhydrophobic, similar to the lotus leaf

one, easing the detachment of the water drops. Similar processes of vapour condensation and water harvesting are used in many industrial applications (thermal manipulation [71], [72], water desalination [73], [74], power generation [75]).

On hydrophilic flat surfaces, the initial nucleation is fast, followed by a filmwise condensation: the liquid is accumulated on the surfaces as an immobile film. On hydrophobic flat surfaces, the nucleation is inhibited by the surface chemistry, and the condensed liquid forms mobile drops. By thoughtfully designing the surface to reach superhydrophobicity, the droplet mobility can be significantly enhanced [76]–[78] by the reduced contact line of condensed droplets [79]–[83]. The advantage of having greater mobility of drops comes with a price: the energy barrier for the first nucleation to appear is considerably higher than on hydrophilic surfaces, leading to a low droplet nucleation density [84]. Furthermore, during condensation the droplets tend to transit from Cassie-Baxter to Wenzel state [85]–[87]. This transition negatively influences the mobility of the drops.

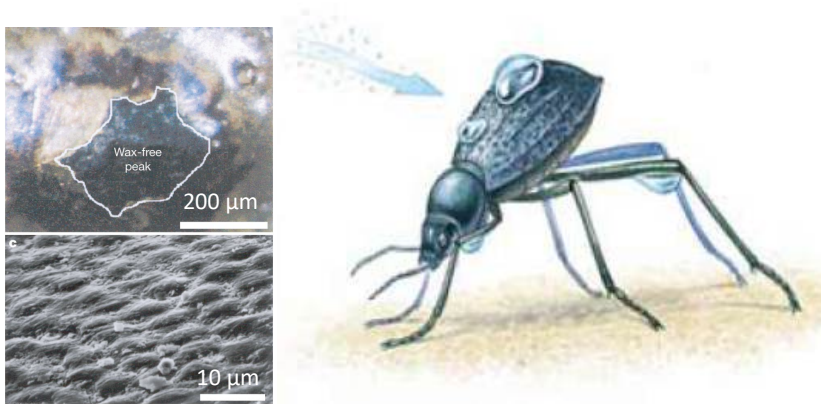


Figure 6: A) The bump of Stenocara free from wax, the surfaces underwent a treatment that shows the presence of wax on a surface (adapted from [88]). B) Image of a beetle harvesting water from the fog (adapted from AskNature.org). C) SEM image of the depressed area between the hydrophilic surfaces, the structures remember the one on lotus leaf (adapted from [88]).

In order to maximize water nucleation and maintain high mobility of small condensed, one is required to combine the ability of filmwise and dropwise condensation: a surface which such requirement has already been exploited by the Namib Desert beetle. The hydrophilic bumps on his back have filmwise condensation properties, while the superhydrophobic regions

maintain dropwise condensation properties [88]. The filmwise condensation on the hydrophilic bumps experiences different fate compared to flat hydrophilic surface, where the liquid spread on the entire surface. Drops grow confined on hydrophilic patch between small bumps with a constant contact line and an increasing contact angle. Thanks to this unique composition, drops on hydrophilic area grow initially with a filmwise regime, to then switch to a dropwise regime as soon as the hydrophilic area is completely wet. On the superhydrophobic surface, the condensation is driven by heterogeneous, low-density nucleation. This time the growth of the drop is done at constant contact angle, the drops rest in fakir state over the microstructure.

Different surfaces inspired by Namid Desert beetle have been already realized [46], [89], in particular with a focus on understanding the mechanism of this composite state [90]. They first generated the synthetic surfaces with c-moss like process and the growth of liquid drops on the surface comparing it with the classical law $r = \rho t^\alpha$ [91], [92] was measured.

The drop growth at constant contact angle, on the superhydrophobic surface, can be easily matched with the theoretical model. However, on hydrophilic zones, the droplet growth cannot be modelled with the same model, which suggest the existence of a different growth mechanism on this hybrid

surface. As a matter of fact, drops on a hybrid surface have a faster growth rate with respect to the hydrophobic one, especially in the early phase [90]. The surfaces that are going to be investigated within this work are inspired by *Stenocara* beetle. It differs from the one that can be found in nature, or in artificial surfaces that mimic the natural one. The present work describes the development of a silicon-based surface composed of micrometric pillars, where every pillar is chemically heterogeneous. The top part of the cylindrical pillars is hydrophilic, while the lateral side and the bottom part of the surface are coated with hydrophobic fluorinate. This has been done in order to achieve the higher possible hydrophobic properties of the surface between the hydrophilic spots, air. Air has contact angle equal to 180° representing the perfect hydrophobicity. Chapters 8, depict in details the details of the process, experimental apparatus, and theoretical dissertation.

2 Hierarchical microfabrication techniques

2.1 Introduction

In this chapter, we briefly introduce the standard microfabrication equipment and techniques used to generate our superhydrophobic surfaces on a silicon substrate. Surfaces are realized using a CMOS pilot line. Fabrication processes are carried out in class 100 clean room. First, we describe the clean room processes we used to generate non-hierarchical structures, it follows the description of chemical coating used to make hydrophobic the native oxide of silicon, and then moulding process that involves the use of Polydimethylsiloxane (PDMS). Finally, we describe in details the innovative techniques used to generate our hierarchical and cyclic structures.

2.2 Non-hierarchical Structure Fabrication

In order to realize structures on silicon substrate (pillar, holes or texturing) we used the following fabrication steps.

2.2.1 Initial Cleaning

Initial cleaning: The process to fabricate our surfaces starts with an initial cleaning of the silicon wafer. The procedure consists of four consecutive baths: the first one is composed of hot sulfuric acid-hydrogen peroxide, and the second bath is diluted hydrofluoric acid, it is used to remove the silicon dioxide. The procedure leaves a hydrogen passivated silicon surface that

results hydrophobic. the following two baths consist of a standard procedure called RCA cleaning. The whole procedure ensures that no metallic or organic contaminants are present on the wafer surface. The perfect cleaning of the surface ensures the reproducibility and the success of further microfabrication process.

RCA cleaning: This procedure is used to ensure cleanness and absence of contaminant on a wafer before introducing it into a furnace. The process consists of two consecutive baths, spaced by cleaning in deionized water. The first step consists of an ammonia peroxide mixture: the objective of this bath is to remove particles of organic contamination from the silicon surface. The second and last step consists of a hydrochloric acid peroxide mixture, the bath removes the metal contaminant from silicon oxidized surfaces.

2.2.2 Thermal Oxidation

The chemical process where silicon dioxide (SiO_2) is grown at elevated temperatures is called thermal oxidation. Silicon dioxide is one of the key factors that are at the base of the success of the planar technology in the semiconductor industry. In particular, it has different uses: is used as hard mask for an implant or an etch, as a dielectric layer in the MOS devices, as an

insulator, and also as a passivation layer. A thin film of silicon dioxide already grows at room temperature. This native oxide grows as oxygen diffuses at room temperature when silicon is exposed to air. This native oxidation at room temperature involves a tiny layer, 0.5-1 nm thick. The oxidation process ends in few hours, with a final thickness of 2-3 nm: the energy of oxygen atoms at room temperature is too small to diffuse further through the already formed dioxide layer. To grow a thicker layer of silicon dioxide, high-temperature diffusion is needed. The process itself is complex, since diffusion of oxidant, chemical reaction, and volume increase take place concurrently to form silicon dioxide from the silicon substrate. The process strongly depends on oxidant species, pressure and temperature of oxidation ambient, and silicon crystal orientation. To guarantee repeatability and quality of the silicon dioxide these parameters need to be controlled. Oxidant species can be pure oxygen (dry oxidation), or a mix of oxygen and hydrogen (wet oxidation). Dry oxidation is slow, normally lower than 100nm/h, and final thickness can be easily controlled. The oxide has high-quality properties. Wet oxidation is much faster than dry oxidation, it can be up to 600 times faster (in volume growth). This process is used to produce thick layers of silicon oxide. The oxide quality is lower than for dry oxidation: it has lower dielectric properties and greater porosity that leads to impurity penetration. In our processes, we have always used wet

oxidation. Indeed, we employed silicon dioxide as hard mask for etching or texturing steps, and we do not need high-quality dioxide, but rather a thick layer.

2.2.3 Lithography

The photolithography process is used to generate a patterned protective layer on silicon substrate. This pattern is then transferred on the silicon substrate with an etching step. The photolithography process is composed of the following main steps: wafer cleaning, photoresist spin coating, soft baking, mask alignment, photoresist exposure and developing, and hard baking. The wafer is then etched and the photoresist is finally removed. We will describe the cleaning procedure of the wafer more in detail in next section. Before photoresist coating, a deposition of a primer is needed: it enhances the hydrophobicity of the substrate allowing constant thickness of photoresist on the wafer area. The photoresist is a photosensitive material applied to the wafer on liquid state. The wafer is then spun at high angular velocity (1000-5000 rpm) for few seconds (30 -60 s). The spinning spreads the resist in a uniform layer that, in our case, can vary from 10 μm to 110 nm depending on photoresist physical characteristics and spin velocity. The wafer is then posed on a hotplate for soft baking: the process improves the

adhesion and removes the solvent. Typically the temperatures of soft baking are about 80 to 90 Celsius applied for a time span of a few minutes. The mask alignment is used only in case of multiple lithographies, the first mask impresses a marker on the silicon surface that is then transferred to the substrate by the etcher. The next masks will be automatically or manually aligned on this marker. After photoresist deposition, a step of exposure with high-density UV light (wavelength vary from 150 to 500 nm) is needed to impress the protective layer. The radiation of UV light changes the photoresist solubility and transfers the mask image onto the resist in the form of a latent image. The step of development dissolves selectively the resist and transforms the latent image into a relief image. The developer is normally sprayed on the substrate. Two types of photoresist exist: negative and positive. Positive photoresist becomes soluble in the developer after UV irradiation and negative becomes almost insoluble in developer. In our processes, we always used positive photoresist, as is for most of the semiconductor processes. Hard bake is used to harden the photoresist and make it more resistant to the following etch steps. The bake can be made in a vacuum or ambient oven, for 30 to 120 minutes at temperatures between 120 and 180 Celsius. This last step always relaxes the border of structures that have been defined with photoresist. This relaxation of the border, if excessive, may lead to incorrect pattern transfer on silicon substrate. A solution to this problem

is to use vacuum bake, as it prevents the border relaxation, but it is less effective in hardening the resist. After the etching step, the removal of remaining photoresist can be made with wet or dry processes. Wet etch uses resist strippers that cause the photoresist to lose adhesion and leave the substrate. The dry process is an oxygen plasma that burns (oxidize) the photoresist.

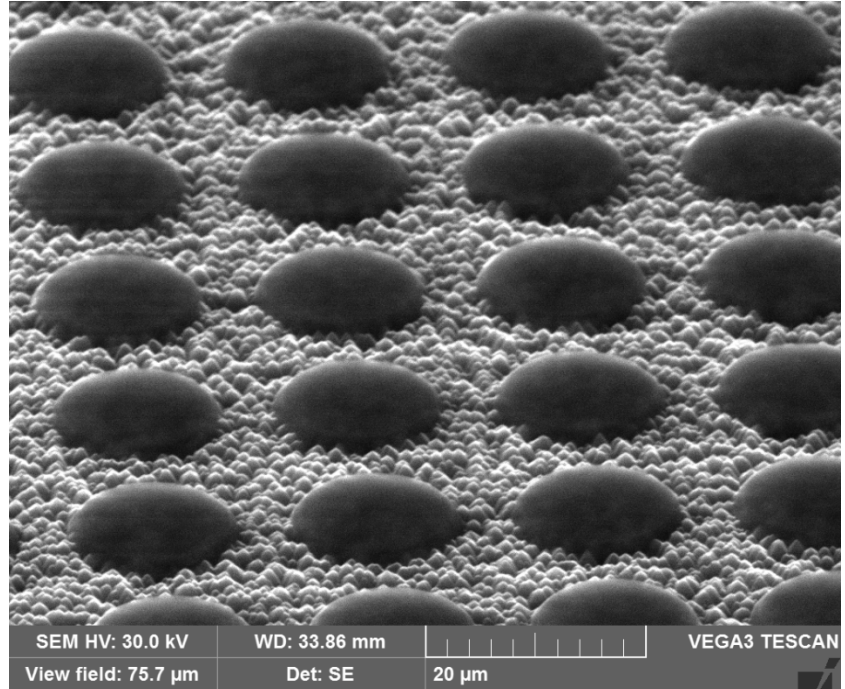


Figure 7: SEM image of photolithography on textured surface. The round “island” are impressed photoresist, it can be seen how the photoresist is not well defined but has round edges.

2.2.4 Dry Etches

2.2.4.1 Deep Reactive Ion Etching (DRIE)

The high aspect ratio pillars that have been realized in the thesis are fabricated with a deep reactive-ion etching process (DRIE). DRIE process is typically used to generate high aspect ratios

structures, such as holes, trenches, or pillars. The highly anisotropic etch process used by DRIE has been originally developed for MEMS devices, and gradually became of broad use in microfabrication. The peculiar technology used to maintain high aspect ratio is called Bosch process [93]. Bosch process uses two alternated phases to generate vertical trenches:

- The first step consists of a nearly isotropic plasma etch. The plasma is mainly composed of SF₆-ions, a silicon etchant, that is accelerated towards the silicon surface by a radio frequency (RF) bias. This generates a physiochemical etch.
- The second step is the deposition of a passivation layer of C₄F₈, a chemically inert substance similar to Teflon that isotopically covers all the surfaces.

The two phases have a different time span, in the order of seconds. The passivation layer is deposited on the whole surface and protects it from chemical etching. The accelerated ion impact on the bottom of the surface destroys the passivation layer and allows the chemical etch of SF₆ on the silicon surface. This does not happen on the lateral side of the surface, where the passivation layer protects the walls from chemical etching.

This sequence is repeated many times, this leading to nano-step of isotropic etch that happens only on the bottom of the surface. Depending on the time span of the etching step, the sidewall presents a periodic undulation with period between 100nm and 500nm. The etch time span and impact energy can be tuned according to the results that we want to obtain: short time and lower RF power imply smoother walls but also small steps in the vertical direction, longer time and high RF power imply rough surface but fast etch rate. For deep etch a thick photoresist is needed to protect areas that we do not want to etch. In fact, also the photoresist is etched during the process, the etching rate of the photoresist being lower than that of silicon. This introduces a limitation on structure depth that depends on the thickness and etch rate of the photoresist. To overcome this problem a hard mask of aluminium can be used; aluminium has an etching rate that can practically be considered as zero. Despite this advantage, the use of aluminium as hard mask brings a series of technological issues [94], that limited its adoption in microelectronic fabrication.

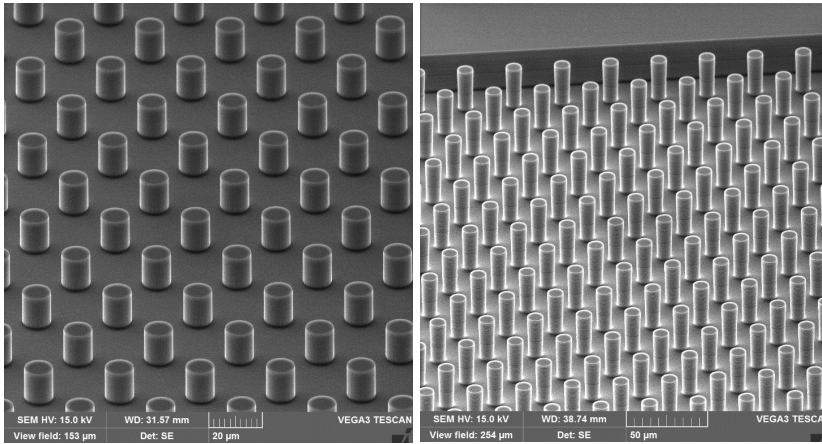


Figure 8: SEM images of pillars generated with DRIE process using Bosch technology. On the left a low roughness process and on the right, a fast etch process is used. The pillars generated by a fast etch process have scallops that can be clearly seen at this magnification, while on the low roughness process the scallops are not visible at this magnification.

2.2.4.2 Reactive Ion Etching (RIE)

Reactive Ion Etching (RIE) is a process similar to DRIE. It is an ion-assisted etch method that does not use the Bosch process. It is used in the manufacturing of micro- and nano- systems to reproduce the pattern defined by a previous photolithography step. It is highly precise in pattern transfer thanks to the control

of homogeneity, etch rate and profile. RIE is possible due to accelerated plasma with ions of chemical reactive gasses pumped into the reactive chamber. The ions are accelerating towards the surfaces where the chemo-physical attack etches the substrate. The etching can be isotropic or anisotropic, but always for shallow etches. In our processes, we used a combination of SF₆ and CHF₃ to etch the hard mask of silicon dioxide before the silicon DRIE etch.

2.2.4.3 Texturing

The process used to increase roughness on silicon surface is called texturing. This process is commonly used to decrease reflectiveness of the substrate in silicon solar cells. In that field, it is fundamental to control the morphological properties of the textured surface to maximize the cell efficiency. Different techniques are used to texture the surface: mechanical scratching, plasma etching, and chemical etching. Chemical etching is commonly used on silicon for his efficiency/cost ratio. The most common wet etch solutions used for texturing silicon surface are potassium hydroxide (KOH), sodium hydroxide (NaOH), and tetramethylammonium hydroxide (TMAH). These alkaline solutions have different etch rate, depending on crystallographic planes. Using these solutions on single silicon crystal wafer with specific orientation (100) generates small square based pyramids on the surface.

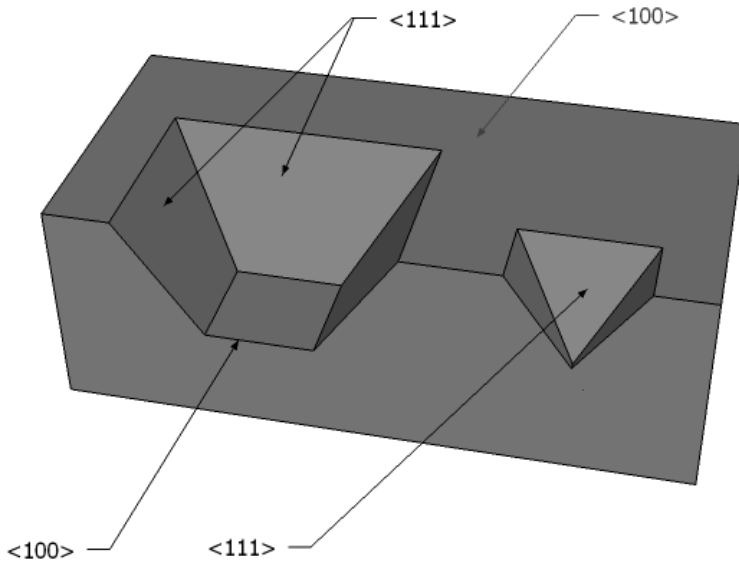


Figure 9: The sketch in the image shows how TMAH-etch works on silicon substrate. It etches faster the plane with 100 orientation than 111 orientation.

KOH and NaOH are highly toxic, furthermore, the sodium and potassium contamination are deleterious for microelectronic devices. We then focus on TMAH solution for our processes. Even if the surfaces that we generate are not used as

microelectronic devices, the facility we used to generate the surfaces has multiple users: hence, only clean room compatible items are allowed. In addition to being clean room compatible, TMAH is also non-toxic and easy to handle [95]. As a plus, TMAH has high etching rate, good anisotropic etching, and it is extremely selective on silicon oxide. This last property allows for the use of silicon oxide masks. Our textured solution is composed of 2% in volume of TMAH, 8% of isopropyl alcohol (used as surfactant) and deionized water. The etching time was 10 minutes and temperature 70°C. The process allows the formation of pyramids thanks to the formation of hydrogen bubbles on the silicon surface. Bubbles block the chemical reaction and acting as a mask allow the generation of pyramidal structures. Bubbles dimensions are controlled by the temperature of the liquid; therefore by regulating the temperature, we control the dimension of pyramidal elements.

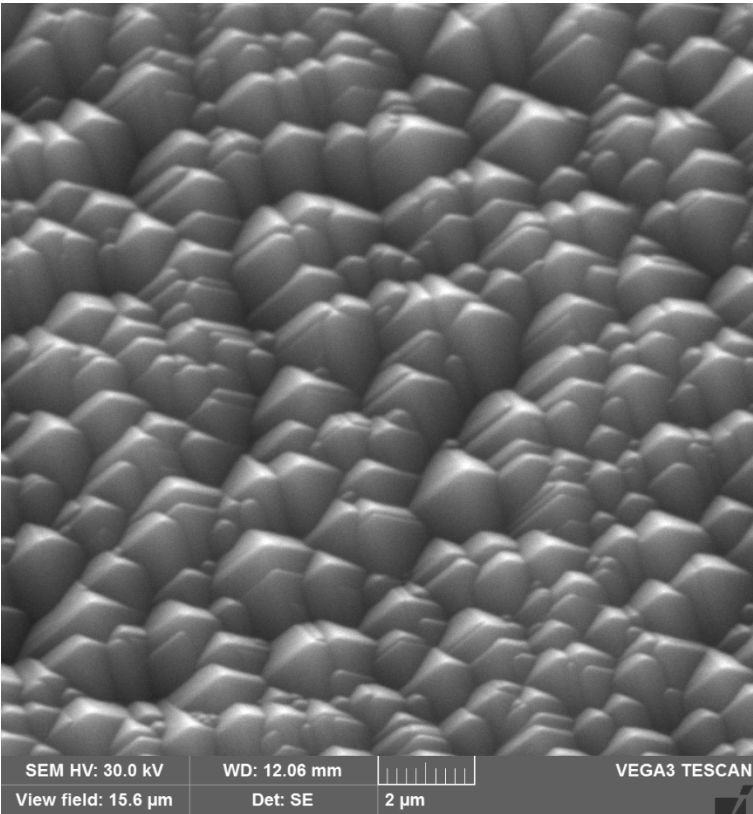


Figure 10: SEM image of textured surface, silicon wafer was immersed for 10 minutes at 70 Celsius in 2% TMAH solution.

2.2.5 Scanning Electron Microscopy

The Scanning Electron Microscopy (SEM) uses a focused beam of electrons to generate images at high magnifications. A beam of primary focused electrons impacts the sample, and in scanning mode, it defines a rectangular area. The interaction between the electron beam and sample's surface generates a secondary electron beam. An electron detector captures the secondary beam, the information collected by the detector is converted into electrical pulses and sent to the monitor. The resulting image is a grayscale representation of the analyzed specimen. We used the SEM images to geometrically characterize our surfaces before physically testing them. This step is fundamental for microfabrication of 3D structures: as a matter of fact, the SEM analysis is time-consuming and requires advanced skills with respect to the use of a simple optical microscope, but it allows to visualize the 3D structures of the realized surface with a resolution on the order of nanometer.

2.2.6 Hydrophobic chemical coating

Silicon surfaces have been coated with 1H,1H,2H,2H-Perfluorodecyltriethoxysilane (PDTS or PF3). This silane is known to make silicon substrates hydrophobic [96] with a contact angle on flat surface of about 109° [97]. A controlled flow of inert gas (N₂) is used as carrier gas for the silane. N₂ is introduced in the silane bubbler (maintained at 80°C), then the silane-N₂ mixture

reaches the sample chamber, maintained at a constant temperature of 150°C. The reaction time was typically 50 minutes.

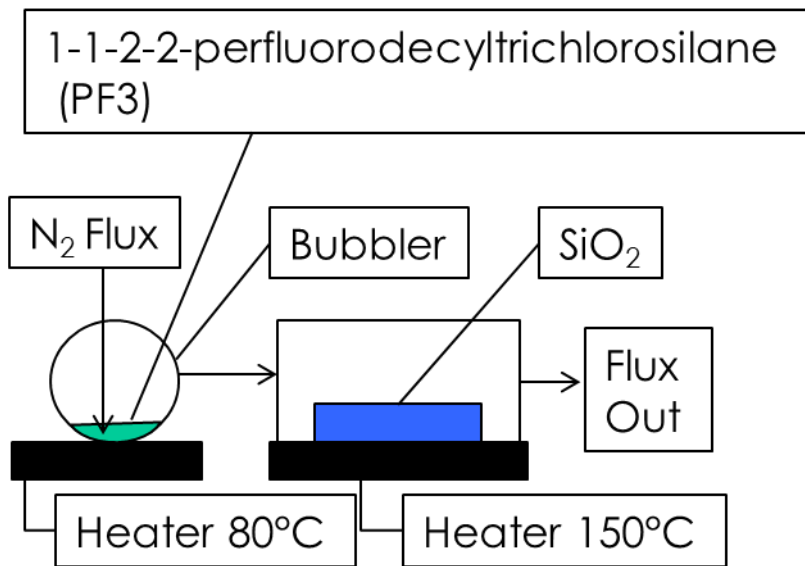


Figure 11: The image shows the process used to apply the self-assembly monolayer on the silicon substrate.

2.3 Soft Structures Fabrication

Polydimethylsiloxane (PDMS) is an elastomer able to accurately reproduce micro- and nanopatterns that have been produced

with soft lithography and micromachining [98], [99]. We used our micropatterned silicon surfaces as a mould for PDMS. PDMS is supplied as two liquid components: a pre-polymer base and a cross-linking curing agent. When the two liquids are mixed together at a given ratio, the compound becomes curable at room temperature or in the oven (up to 200 Celsius). Datasheet indicates the curing time depending on given temperature. Before the moulding process itself, some pretreatment has to be performed. The silicon substrates have to be coated with Trimethylchlorosilane (TMCS) to avoid the sticking of liquid PDMS on the surface. After mixing, and before curing the PDMS compound have to be degassed for 30 minutes, then deposited on silicon substrate, and degassed again for 30 minutes. After curing the sample is allowed to cool down at room temperature and then the PDMS-copy is removed from the surfaces by peeling. The PDMS-copy is then observed under SEM microscope to ensure the quality of the result.

2.4 Hierarchical Structures Fabrication

In this section, the processes that we used to generate hierarchical surfaces are described in detail. First, we describe a process that combines wet etch (TMAH texturing) with dry etch (DRIE process), the DRIE process generates defined pillars while TMAH texturing generates a second hierarchical level with random pyramidal elements. We then describe the two-

lithography process that generates a non-random two-level hierarchical surfaces. Finally, the last paragraph presents the process used to generate re-entrant surfaces. These surfaces are used to generate superhydrophobic surfaces from intrinsically hydrophilic substrate. We generated also surfaces with several hierarchical re-entrance, such surfaces present several energy barriers to the liquid penetration of the surface.

2.4.1 Wet Etch Hierarchical surfaces

This process has been designed to produce hierarchical surfaces on large area with an inexpensive and fast process. The process requires only one lithographical step and uses a combination of TMAH texturing and DRIE process. TMAH texturing is used to realize a textured surface that represents the second hierarchical level. Soft lithography is used to precisely define pillars, and the pillars were realized with a low roughness DRIE process. The use of low roughness process in the dry etching step is important to guarantee the flatness on the side of the pillars, this allows the texturing to equally etch the pillars side. By exchanging the order of dry and wet etches two surfaces with different morphology are realized. In Figure 12 are represented the two different processes, the A-sequence reproduce the process where the steps flow is: soft lithography-DRIE-texturing.

The B-sequence reproduce the process where the steps flow is: texturing-soft lithography-DRIE. On the right part of the figure, SEM images of the real structures are represented, realized with the two methods. The texturing has been performed at 70 Celsius for 10 minutes in an aqueous solution (deionized water) with 2% solution of TMAH, and 8% of IPA (used as bubble surfactant). The DRIE process consists of 180 cycles, each cycle having 3.3s of etching (SF6 plasma) and 0.8s of passivation layer (C4F8). Process A (Figure 12) generates structures with hierarchical level also on the lateral side of the pillars while process B generates structures with hierarchical level present only on the top part of the pillars.

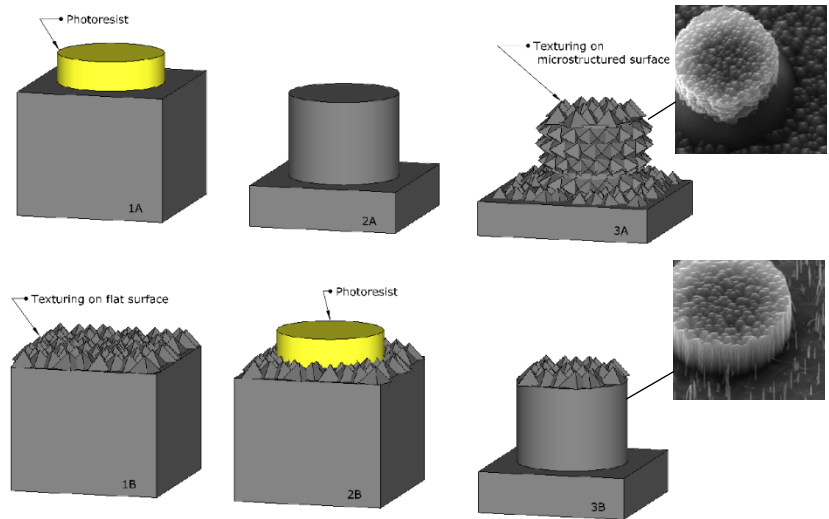


Figure 12: The sketch shows the process flow to generate the two wet-etched hierarchical surfaces. The A-sequence reproduces the process where the steps flow is soft lithography-DRIE-texturing. The B-sequence reproduces the process where the steps flow is texturing-soft lithography-DRIE. On the right, SEM images of surfaces are displayed, produced with the presented methods.

2.4.2 Two Steps Lithography Hierarchical surfaces

To realize hierarchical surfaces with precise morphology on both first and second hierarchical level a two-steps lithography is needed. The process flow is more complex with respect to the process described in the previous paragraph but presents the advantage of controlling exact aspect ratio, pitch distance, and pillars diameter on the second hierarchical level. This feature seems trivial, but it is fundamental to generate robust Cassie-Baxter state [22]. The major issue in a two steps lithography process is represented by the presence of structure on the wafer substrate that can affect the second photoresist coating. In our process, we use a thick photoresist for the first hierarchical level, 2.1 μm or 10 μm depending on the structures dimension, and a thin photoresist, 700 nm, for the second hierarchical level. Furthermore, structures of the first hierarchical level have to be at least 20 to 40 μm high, while the structures of the second level

need to reach a height of 10 μm . Such values are definitely not compatible with a substrate spin coating. In fact, if there are structures on the substrate their height need to be lower than resist thickness to guarantee uniformity in the resist coating. To overcome this problem, we used a hard mask of silicon dioxide (thickness 200 nm) to generate the second hierarchical level [100]. The process is described in detail in Figure 13. The wafer is first cleaned and then oxidized in a wet diffusion process (975 Celsius for 20 minutes) to grow 200nm of silicon dioxide. The structures of the second level are then defined on the silicon dioxide through soft lithography and RIE etch of the dioxide. The resist is then removed with dry O_2 plasma. The first hierarchical level is then defined with soft lithography, and BHF wet etch used to remove silicon dioxide structures that have not been coated with the second photoresist. High aspect ratio DRIE process is used to define structures of first hierarchical level on silicon. The remaining resist is removed in O_2 plasma, and a second DRIE is performed. The silicon dioxide that has been patterned at the beginning of the process is used in this step as hard mask. A low roughness process is used to define the small pillars of the second hierarchical level, that have typical dimension of 1 μm in our case. The remaining silicon dioxide on top of the pillars is removed with a BHF wet etch.

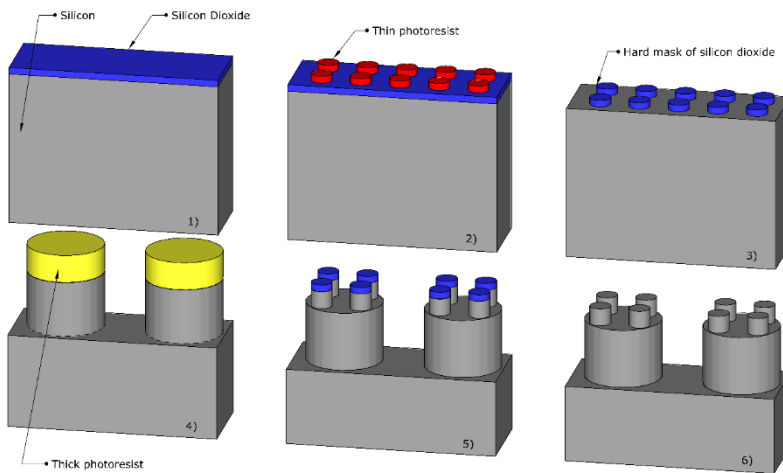


Figure 13: The sketch shows the process flow to generate precise hierarchical surfaces on silicon substrate with CMOS pilot line. 1) Thermal silicon dioxide is grown on silicon substrate. 2) Definition of the second hierarchical level. 3) Silicon dioxide hard mask for the second hierarchical level. 4) deposition of thick resist and DRIE etch to realize first hierarchical level. 5) Second DRIE etch to realize the second hierarchical level, silicon dioxide hard mask is used in this etching step. 6) The surfaces have been cleaned by the remaining silicon dioxide with a BHF etch. (drawing not in scale).

2.4.3 Re-entrant structure

Re-entrant surfaces are particularly useful to realize superhydrophobic surfaces from an intrinsically hydrophobic substrate. The basic process to generate re-entrant surfaces is derived from an already known process developed to generate optical resonators [101]–[103]. We did not only replicate this process, but we tried to reproduce similar structures improving production time. Furthermore, we generate cyclic surfaces, in which the re-entrant surfaces are piled one over the other, preserving the dimensions. Every re-entrant level of these structures represents an obstacle to water penetration.

2.4.3.1 *One level re-entrant structure*

Different methods are used to generate surfaces with re-entrant structures. Furthermore, we can consider two different families of re-entrant structures: biphasic and monophasic structures. The biphasic structures are composed of a silicon dioxide “hat” and a silicon pillar, the monophasic structures are composed of silicon.

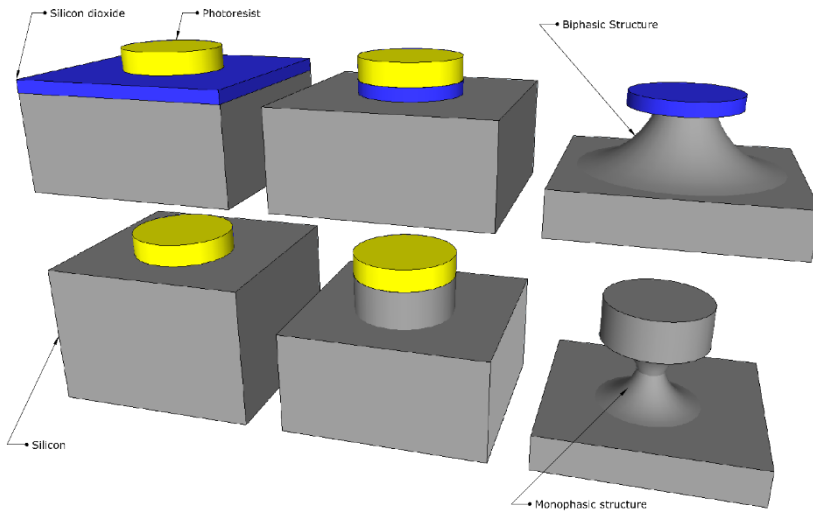


Figure 14: The sketch shows the two processes used to generate re-entrant structures. The top structure is biphasic (silicon + silicon dioxide). The lower structure is monophasic (silicon).

2.4.3.1.1 Biphasic re-entrant structures

The biphasic surfaces are realized using the following steps: silicon thermal oxidation, soft lithography, etch step. Thermal oxidation is made in wet condition, and a 200nm thick layer of silicon dioxide is grown. We use soft lithography and RIE technology to define the upper surface of the re-entrant surfaces. To generate the cavity of re-entrant structures we

explored different options. As a first option, we used a wet etch, extremely selective on silicon: this etch step is rather cheap but highly time-consuming. Furthermore, the wet etch is perfectly isotropic; hence the depth of the etch is limited by pillar diameter. Since the aspect ratio is important for such surfaces, we explored other possibilities. We then used DRIE process, at first tuning a process that does not use Bosch technology, but a continuous etch. The polarization of the plasma towards the surface was reduced to a minimum to obtain an isometric etch. The process results to be much faster than the wet etch, and less isometric. This feature allows generating higher aspect ratio structures. To improve further the process speed, we increased the plasma polarization: this process is commonly called Tapered, it is faster than the previous and generates higher aspect ratio structures, Figure 15.

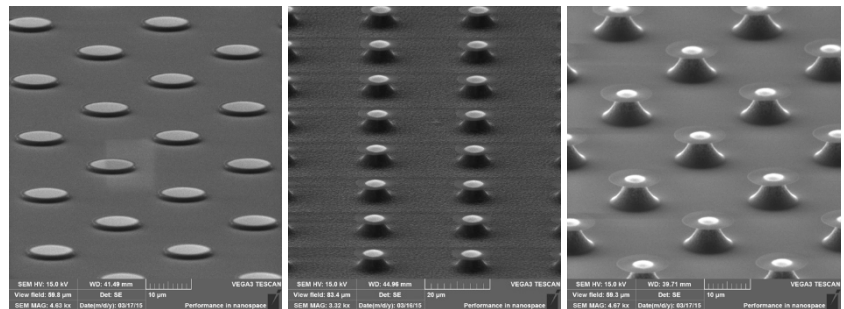


Figure 15: SEM image of re-entrant structures generated with different methods. From left to right: 5 minutes of wet etch, 5

minutes of DRIE isotropic process, and 1 minute of DRIE Tapered process.

2.4.3.1.2 Monophasic re-entrant structures

Monophasic structures are realized on silicon wafer with soft lithography and DRIE. After defining the surface morphology with soft lithography, a low roughness DRIE process was used to generate a vertical wall, then a long passivation step of C4F8 (3s) was followed by a highly isotropic SF6 step. The combination of the last two steps protects the vertical wall and frees from the passivation the bottom part. Following is a step of Tapered or isotropic process that generates the cavity. As can be seen in Figure 16 the use of Tapered process is more effective for the production of these surfaces.

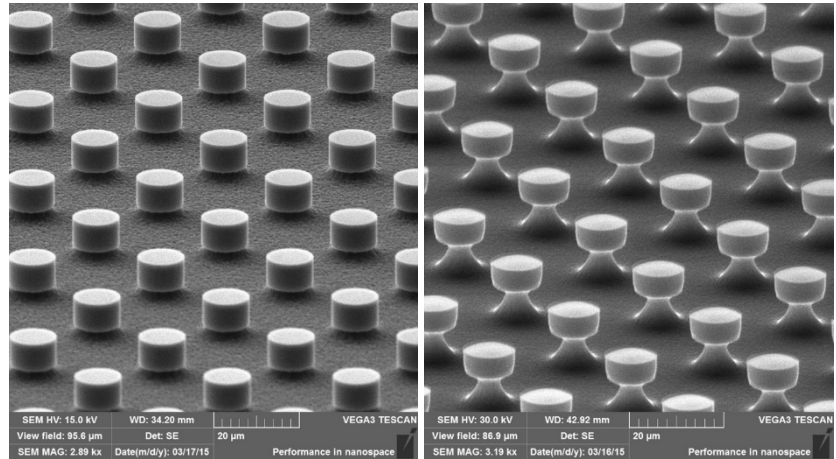


Figure 16: SEM image of surfaces generated with DRIE processes. Low roughness Bosch process is used for the vertical walls (2 minutes) and the cavity is realized on the left with 2 minutes of isotropic process and on the right with 40 seconds of Tapered process.

2.4.4 Cyclic re-entrant structures

Cyclic re-entrant surfaces are realized by iterating the single-level processes used to generate re-entrant surfaces. For both biphasic and monophasic structures, an intermediate step between one iteration and another is necessary to prevent from destroying the part of the structure that has already been shaped. The step is composed of a passivation of C4F8 (3 seconds) and a highly directional SF6 etch step. The passivation

covers identically all the surfaces with a layer of polymer (similar to Teflon) that is inert to chemical etch of SF₆. The directional SF₆ etch step physically destroys the layer of polymer deposited on the bottom of the surface. This last step allows the next step: etch the silicon on the bottom to produce a new structure.

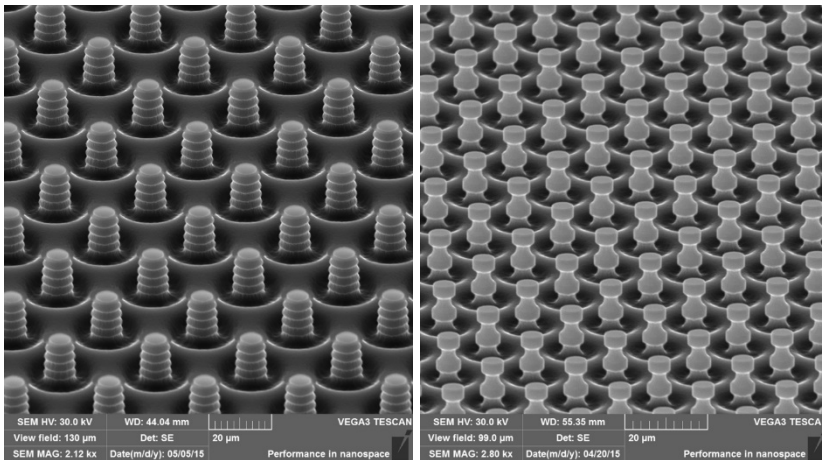


Figure 17: SEM image of hierarchical re-entrant surfaces. On the left biphasic structures and on the right monophasic structures.

As can be seen in Figure 15, the biphasic structures have numerous levels, while the monophasic have only two levels. This is due to a technological problem: profile of these structures is harder to maintain, since the low roughness vertical wall

increases the height of the pillar, making it harder for the next etch to maintain the morphology of the structure. Figure 18 shows the saturation problem that occurs when more than two levels of the hierarchy are realized for monophasic surfaces.

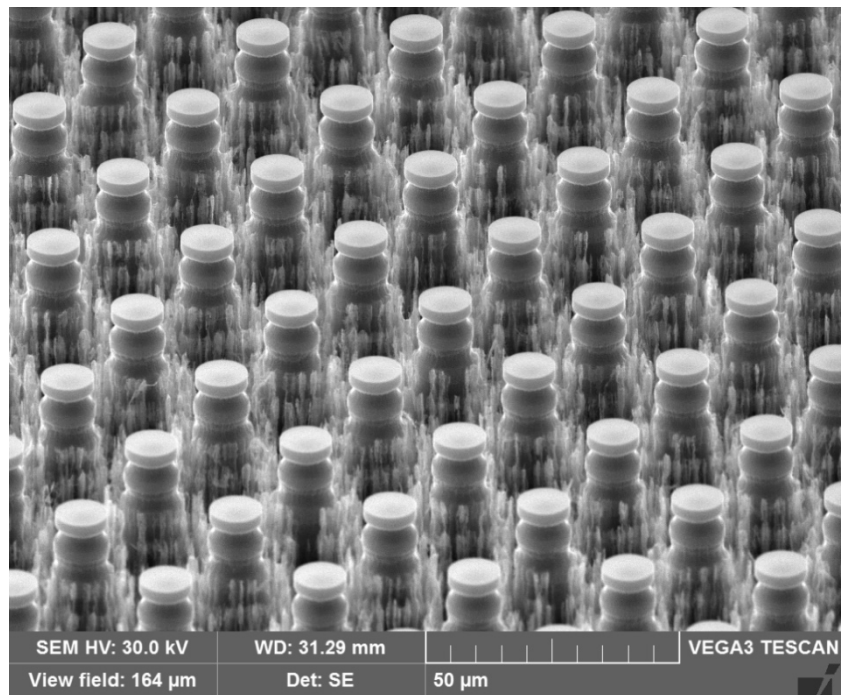


Figure 18: SEM image that shows the saturation problem of producing more than two levels for monophasic surfaces.

3 Hierarchical surfaces for improving wetting

3.1 Abstract

In this work, we present a new method to generate on a silicon substrate hierarchical surfaces inspired by lotus leaf. Mimicking leafs with particular properties, such as low adhesion, water repellency and self-cleaning, is an interesting case of study in the branch of bioinspired materials. These properties arise from a combination of surface chemistry and topography. The lotus leaf surface exhibits a highly controlled specific roughness, which has been studied and imitated by several researchers. The great challenge that has still to be solved is to reproduce lotus-inspired surfaces rapidly and on large areas. Our method consists of a combination of wet and dry etch combined with soft lithography, able to generate nano- and micro- hierarchical structures on silicon surfaces. Two different kinds of hierarchical structures are generated by changing the order of the etch steps. The surfaces realized were then characterized by measuring both the contact angle and the sliding angle. Finally, to validate experimental results, analytical models were implemented to predict the contact angle. The best surface displayed wetting performances superior even to those of the natural lotus leaf, thanks to the hierarchical structure, with a contact angle of 171° and a tilt

angle of 4° , production time of about 90 minutes per silicon wafer, or 30 s/cm^2 .

3.2 Introduction

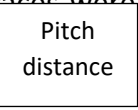
Hierarchical structures, such as the ones found on the lotus leaf [1], [104], are used to improve water repellency of a surface. Specific roughness topologies are in general able to change the wetting property of a surface [105], [106]. Different studies demonstrate theoretically [107]–[109] and experimentally [110], [111] the importance of hierarchy in improving and stabilize superhydrophobic state on the surface. In order to generate hierarchical structures different processes have already been proposed in the literature, typically having in common rather long and complex fabrication processes [65], [110], [112].

The aim of this work is to fabricate hierarchical silicon surfaces with a new and fast method applicable to large areas.

The method presented in this chapter for producing superhydrophobic surfaces is a highly accurate, fast and repeatable microfabrication process realized on silicon substrate. It combines an anisotropic wet etch in a solution based on tetramethylammonium hydroxide (TMAH) [113] and a dry etching performed with a deep reactive ion etching (DRIE). The process herein described requires a minimum 7-minute TMAH processing step plus 9-minutes of dry etching. Depending

on the desired height of the pillars, the maximum processing time is no more than a few hours.

In section 3.3 a detailed description of how the silicon-based micro/nanotextured and hierarchical structures were fabricated is reported. Two different base patterns were used: square-base or hexagonal-base patterns. Surfaces with simple post structures, without hierarchy, were fabricated and used as reference structures in wettability tests. Structures are formed by pillars with different diameters and pitch distances; Figure 19 illustrates the geometries that were fabricated. Surfaces were tested for static contact angle and tilt angle. The flat surface and the textured ones were also tested. Results show that rapidly generated large surfaces display wetting performances superior even to those of the natural lotus leaf, also thanks to hierarchy.



Pitch
distance

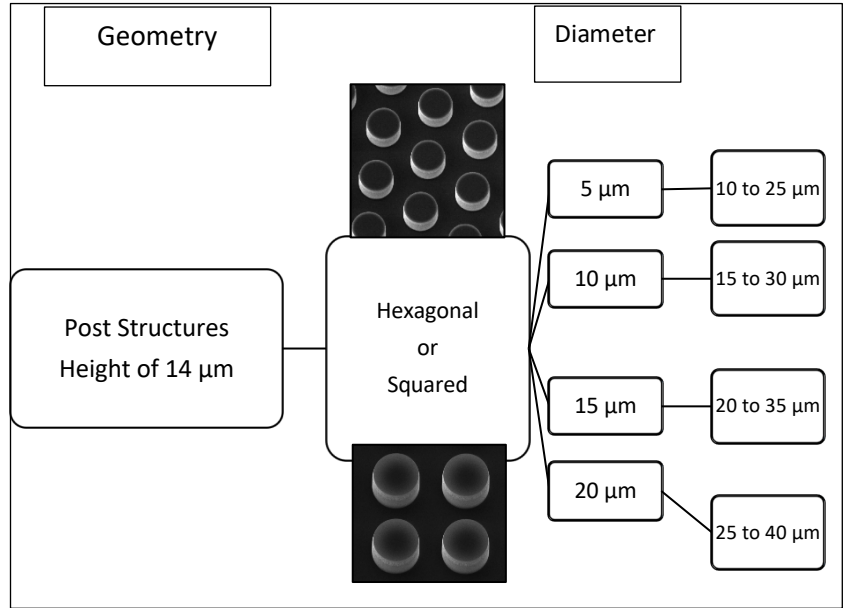


Figure 19: Sizes and shapes of realized structures, we used rectangular or hexagonal base patterns. Diameter of pillars changes from 5 to 20 μm . The gaps between pillars vary from 5 to 20 μm as well, and pitch distances change accordingly.

In Section 3.5 an analytical model, based on Wenzel and Cassie-Baxter models, is implemented to validate the experimental results and to find the most suitable conditions for water-surface interaction for future designs. Section 3.6 and 3.7 close the chapter with the discussion of the results and the conclusions.

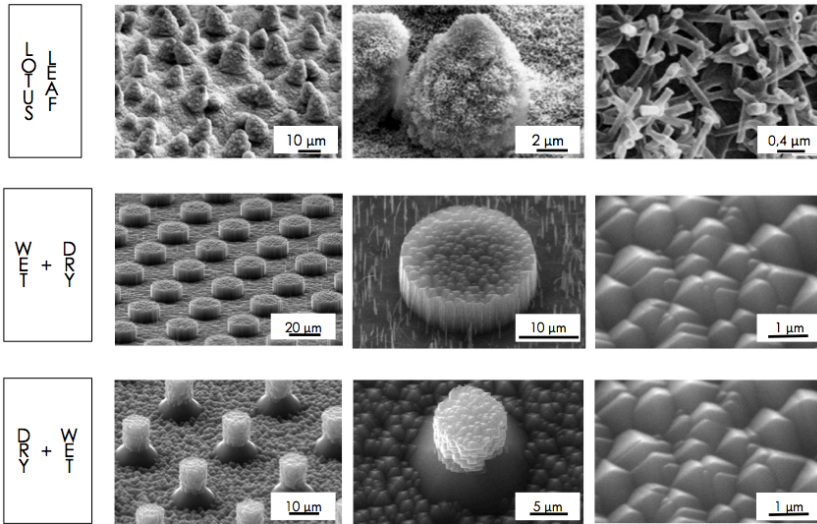


Figure 20: Surface topologies generated with the two processes and compared with the lotus leaf (image of lotus leaf from reference [5])

3.3 Experimental analysis

In this section the experimental part of the work is presented. First, the methods used to generate the surfaces are described, and then the wetting characterizations, for both non-hierarchical and hierarchical structures, are reported.

3.3.1 Surface generation

All the patterns and structures presented in this work were fabricated using a standard CMOS-like process. Post structures were fabricated using a lithographic step followed by dry etching. The dry etching was performed with Deep Reactive Ion Etching (DRIE) equipment, Alcatel AMS 1000.

The sizes and shapes of post structures are summarized in Figure 19. Each pattern presents pillars with different diameters and pitch distances. Diameter goes from $5\mu\text{m}$ up to $20\mu\text{m}$, in steps of $5\mu\text{m}$ and for each value four different pitch distances were considered, from $10\mu\text{m}$ up to $40\mu\text{m}$. Furthermore, two different base patterns were used, square or hexagonal pattern. A constant height of $15\mu\text{m}$ was fixed for all the pillar topologies.

Surface texturing introduces hierarchical substructures in the post structures. A textured surface is obtained by a TMAH solution, which etches the silicon with a high selectivity on the crystalline planes. Hence, by using a $\langle 100 \rangle$ silicon wafer, a heterogeneous and compact pattern of pyramid-like pillars was obtained [113]. The base angle of the pyramid is equal to 54.7 degrees, which corresponds to the angle between $\langle 111 \rangle$ and $\langle 100 \rangle$ planes. The texturing process is composed of two steps; firstly a dip in buffered hydrofluoric acid (BHF) is needed to completely remove the native oxide on the silicon substrate, then a 5 minute wet etch in the TMAH 2% solution is performed;

this process can be considered as the hierarchical module. Combining the hierarchical module and the base process module it is possible to generate two different structures, as shown in Figure 21. In particular, it is possible to obtain a pillar with only the upper part texturized (Figure 21a) or to extend the texturing on the entire structure (Figure 21b), thus including the lateral sides. Due to the presence of a thin native SiO_2 layer, which makes the silicon surface naturally hydrophilic, a self-assembly monolayer (SAM) coating is needed to impose hydrophobicity [96]. In particular, Tetramethylchlorosilane (TMCS) and 1-1-2-2-perfluorodecyltrichlorosilane (PF3) were used for SAM vapor/phase deposition [96].

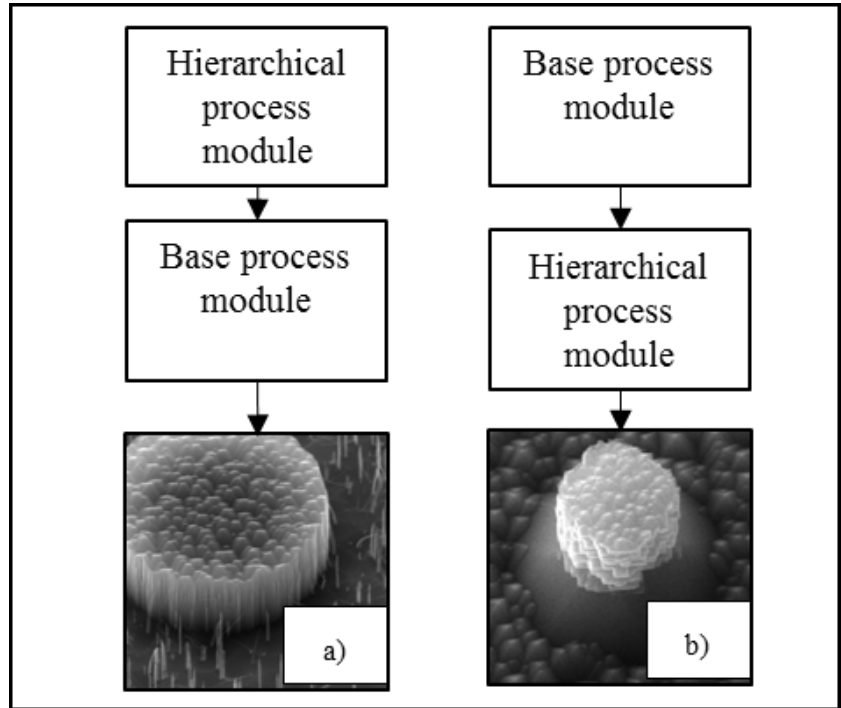


Figure 21: Schematic description of the two processes to generate the hierarchical structures: a) wet plus dry process and b) dry plus wet process.

3.4 Wettability analysis

Wettability measurements were performed using 5 μl drops of deionized water (18 M Ω of resistance). An estimation of drop contact angle was calculated using “drop analysis” software [114]. Experimental results are reported in the next section.

3.4.1 Non-hierarchical pillars

In this section surfaces patterned with pillars, of different diameters and pitch distances, are analysed and compared.

The first results, shown in Figure 22, refer to a comparison between the two different coatings; PF3 has better performance than TMCS.

PF3 coatings renders silicon oxide substrates hydrophobic (CA=109°) in contrast to TMCS coatings (CA=78°) [43], [110]. However, TMCS is quite easy to deposit on the silicon substrate, e.g. the process occurs at room temperature in a closed chamber, while PF3 deposition requires a more complex process, e.g. a well-controlled temperature [96]. Surfaces coated with TMCS in general display an increment of their contact angle, showing Cassie-Baxter interface even if the substrate is intrinsically hydrophilic.

The graphs in Figure 22 provides results of contact or tilt angles for structures coated with TMCS and PF3, respectively. The structures considered have post diameter of 10 μm and pitch distances between 15 and 30 μm .

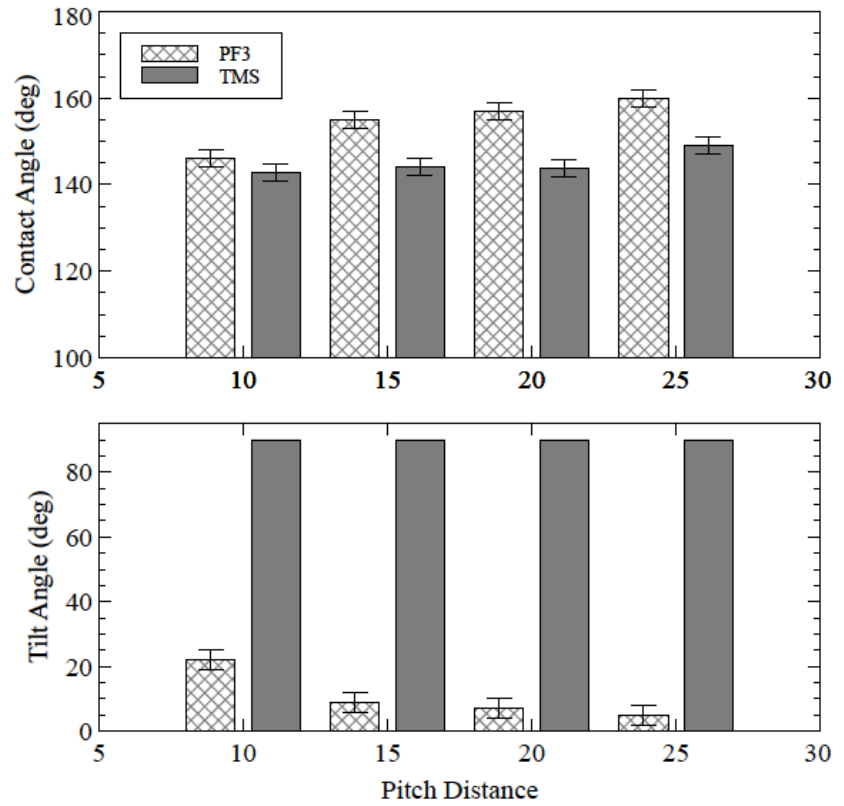


Figure 22: Contact and tilt angle measurements of structures with post diameter of $10\mu\text{m}$ and different pitch distances (microns). Graphs show the comparison between the two types of coatings, i.e. PF3 or TMS. Conventionally here 90° denotes the sticky condition.

Charts on Figure 22 show that not only the contact angle is better for PF3 coating with respect to TMCS coating, but especially the tilt angle. Indeed, TMCS results in a sticky condition, represented in the graph with value of tilt angle equal to 90° , while surfaces coated with PF3 have low tilt angle. For these surfaces the tilt angle decreases as the pitch distance increases. For these reasons all surfaces considered in this work were coated with PF3.

In order to better understand the role of pattern geometries on the surface wettability, square or hexagonal base patterns were generated and analysed. A whole series of structures with pillars of different diameters and different pitch distances were examined. Graphs in Figure 23 show the trend of contact and tilt angles for the two patterns: no significant difference is observable.

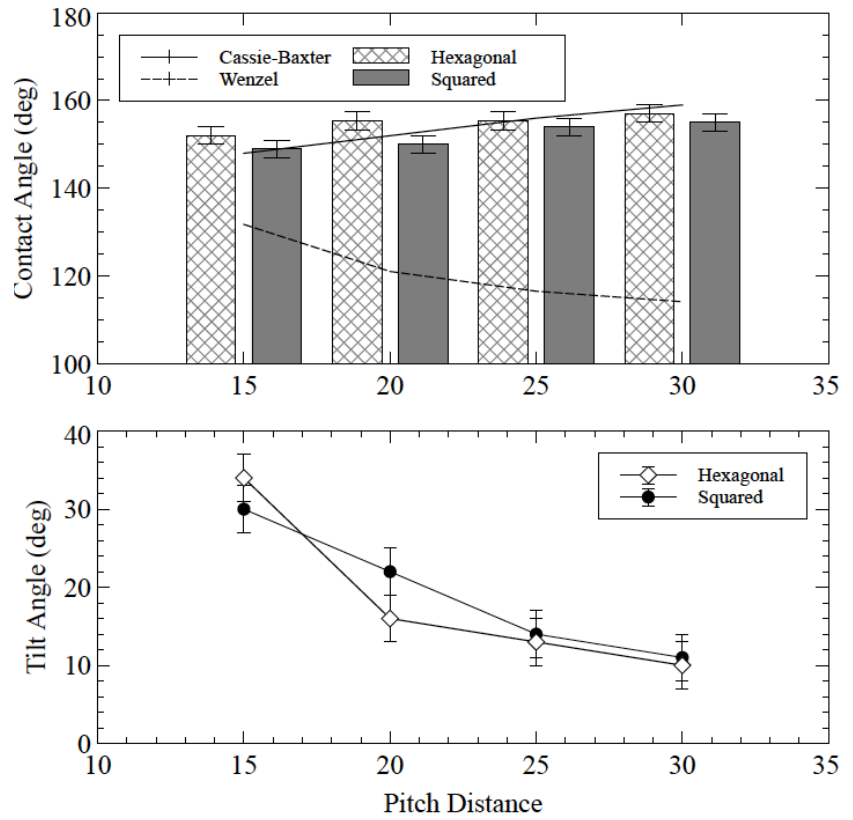


Figure 23: Contact and tilt angle measurements and predictions of structures with post diameter of $10\mu\text{m}$ and different pitch distances (microns): comparison between square and hexagonal base patterns.

In addition Figure 23 presents two analytical predictions for contact angle, where continuous black or dotted lines represent the Cassie-Baxter [21] and the Wenzel [19], [20] predictions respectively. After comparison between analytical predictions and experimental data, it is possible to deduce that surfaces stand in Cassie-Baxter state. Stability of this state has been discussed in Section 3.1.

3.4.2 Hierarchical pillars

In this section similar analyses conducted on the non-hierarchical structures are performed on hierarchical ones (Figure 24 shows below the graphs a sketch of the different structures). Two kinds of hierarchical structures were developed, as illustrated in Figure 24a and Figure 24b. The wet plus dry process generates structures similar to those reported in Figure 24a whereas the dry plus wet process to those reported in Figure 24b. These structures were tested for both contact and tilt angles.

In Figure 24, comparisons between two kinds of hierarchical structures and one kind of pillar structure are reported. Considering surfaces with pillars of 5 μm , four different pitch distances were compared, from 10 μm up to 20 μm . The results reported in Figure 24 refer to those surfaces which reach highest

contact angles and lowest tilt angles. During this study, diameters of 5, 10, 15 and 20 μm were analysed and rationalized according to the Cassie-Baxter equation. The surfaces with a lower solid-liquid interface area fraction ϕ have a greater contact angle, as is the case of pillars with smaller diameters.

Figure 24 also shows how both hierarchical structures present a significant improvement with respect to the post structures in terms of contact angle. Tilt angle varies with the pitch distance for both hierarchical and post structures.

It has been discussed how hierarchy improves the contact angle, however tilt angle does not change significantly with the introduction of a hierarchical level. In some cases, the introduction of an additional level seems almost counter-productive, as can be observed in Figure 24 for the lower pitch distance. This can be due to the partial impalement of the drop on the textured surface, as discussed in the next Section.

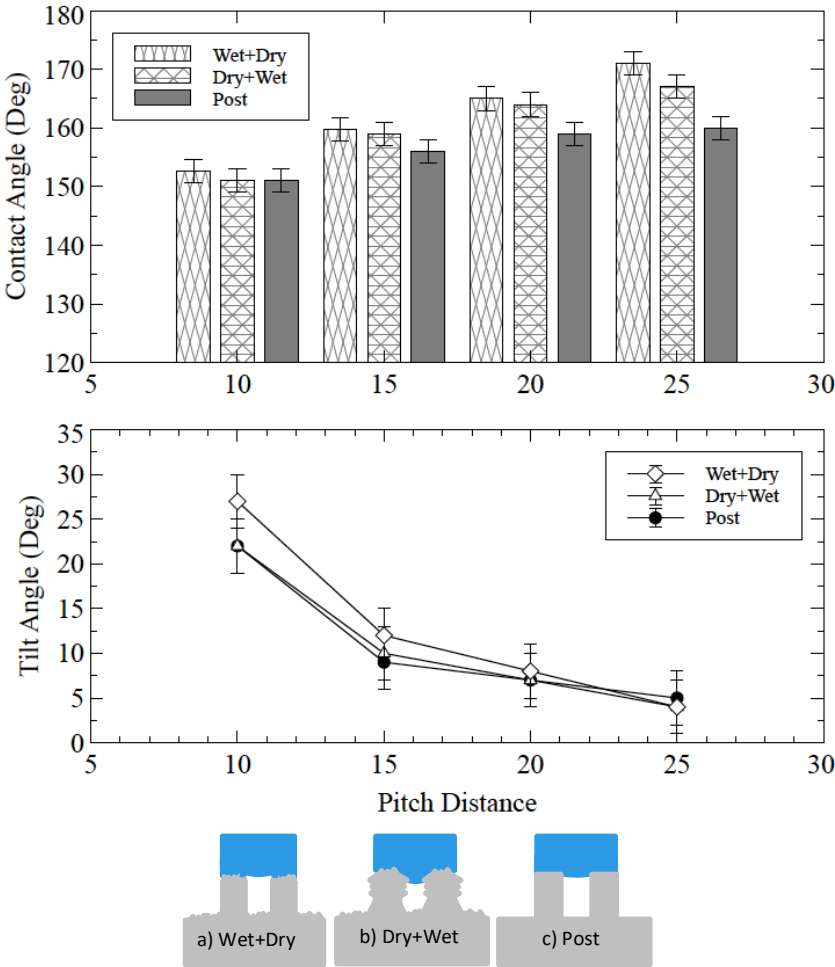


Figure 24: Contact and tilt angle measurements of structures with post diameter of 5 μm and different pitch distances; comparison between the two hierarchical structures a) wet+dry b) dry+wet and the non-hierarchical one c).

3.5 Theoretical analysis

In this section, analytical models are implemented in order to validate the experimental results and consider the stability of the experimental state. Classical theories of Wenzel [17, 18] and Cassie-Baxter [16] are used to fit experimental data for non-hierarchical structures. A general model, combining Cassie-Baxter and Wenzel theories and taking into account hierarchy, is presented developing the hierarchical theory that already exists [107], [108].

3.5.1 Non-hierarchical pillars

It is a straightforward analysis to compute the predictions of the two classical models for surfaces with non-hierarchical pillars, where roughness and area fraction values can be deduced geometrically. Roughness r for a patterned surface is expressed in equation (8), while the solid-liquid area fraction is defined by equation (9), in which P is the pitch distance, H is the pillar height and d is the pillar diameter.

$$r = \frac{A_{real}}{A_{projected}} = 1 + \frac{\pi d H}{P^2} \quad (8)$$

$$\varphi = \frac{A_{solid-liquid}}{A_{total}} = \frac{\pi d^2}{4P^2} \quad (9)$$

It is useful for our purpose to split equation (8) in equations (10) and (11), in this way we can separately consider the lateral and top part of each pillar. In particular equation (10) shows the increase of the effective area due to the lateral sides of the pillars, while equation (11) describes the ratio of the area on top and bottom of pillars and the projected area and for definition this ratio is equal to one for non-hierarchical pillars, namely:

$$r_L = \frac{A_{Lateral}}{A_{projected}} = \frac{\pi dH}{P^2} \quad (10)$$

$$r_{TB} = \frac{A_{Top} + A_{Bottom}}{A_{projected}} = \frac{P^2}{P^2} = 1 \quad (11)$$

Then it is straightforward to define $r = r_L + r_{TB}$.

Experimentally drops on the surfaces appear in Cassie-Baxter state, as can be deduced by comparing experimental results with analytical predictions, Figure 23. This state is stable if equation (12) is true [22] for the intrinsic contact angle ϑ_0 :

$$\cos\vartheta_0 < \frac{\varphi - 1}{r - \varphi} \quad (12)$$

	10	15	20	25	30	35	40
5	104.7	117.8	128.1	136.0	-	-	-
10	-	103.7	113.9	122.5	129.5	-	-
15	-	-	103.9	112.8	120.4	126.7	-
20	-	-	-	104.4	112.5	119.4	125.2

Table 1: Minimum intrinsic contact angle (degrees) to achieve stable Cassie-Baxter states for different pitch distances (columns) and pillar diameters (rows), measured in microns.

Table 1 shows the minimum value of intrinsic contact angle at which the structure has a stable Cassie-Baxter interface for the corresponding geometrical parameters. The surface base contact angle for the PF3 coating is $\vartheta_0 = 109^\circ$. It can be seen that most of the structures analysed are theoretically not stable in Cassie-Baxter configuration. However, secondary effects generate an energy barrier between the Cassie-Baxter and Wenzel state, making the first state metastable rather than unstable [115], as it is observable in our experiments.

3.5.2 Hierarchical pillars

The wetting state becomes more difficult to predict for hierarchical structures. Indeed, hierarchical surfaces can have more complex interfaces. Typical examples of a complex natural interface is that of the rose petals [116].

Two different hierarchical structures are considered here: one with hierarchy on the top and the bottom of the pillars, Figure 25a, and one with hierarchy only around the lateral side of the pillars, Figure 25b. More complex structures, as shown in Figure 26 and

Figure 27, can be easily manufactured with our process. Figure 26 is a schematic representation of the wet plus dry process, while

Figure 27 represents the surface generated with dry plus wet

$$\cos\vartheta_{ww} = r_L r_l \cos\theta_0 + r_{TB} r_g \cos\theta_0 \quad (17)$$

$$\begin{aligned} \cos\vartheta_{wc} = r_L (\varphi_l (\cos\theta_0 + 1) - 1) \\ + r_{TB} (\varphi_g (\cos\theta_0 + 1) - 1) \end{aligned} \quad (18)$$

$$\cos\vartheta_{cw} \equiv \varphi (r_l \cos\theta_0 + 1) - 1 \quad (19)$$

$$\cos\vartheta_{cc} \equiv \varphi \varphi_l (\cos\theta_0 + 1) - 1 \quad (20)$$

$$+ r_{TB} (\varphi_g (\cos\theta_0 + 1) - 1) \quad (18)$$

$$\cos\vartheta_{cw} = \varphi (r_g \cos\theta_0 + 1) - 1 \quad (19)$$

$$\cos\vartheta_{cc} = \varphi \varphi_g (\cos\theta_0 + 1) - 1 \quad (20)$$

process. The roughness parameter and area fraction can again be found with geometrical considerations for both cases,

allowing the analysis of different kinds of hierarchical structures thanks to equations from (13) to (16).

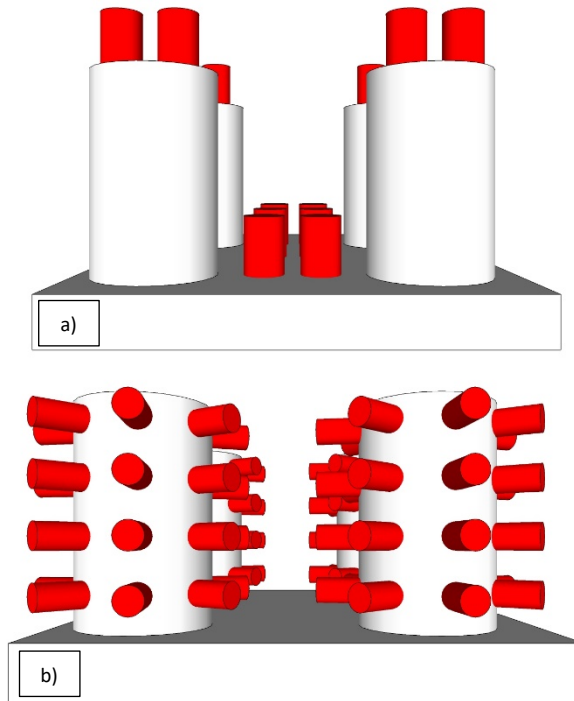


Figure 25: Sketches of the fabricated hierarchical structures a) with hierarchy on the top and bottom of the pillars and b) with hierarchy only on the lateral side of the pillars.

equations (13) and (14) describe the area fraction and the roughness parameter for the first order level hierarchical structures, i.e. (red) sub-pillars in Figure 25a:

$$\varphi_g = \frac{\pi d'^2}{4p^2} \quad (13)$$

$$r_g = 1 + \frac{\pi d' h}{p^2} \quad (14)$$

where d' , h , and p are diameter, height and pitch distance of the sub-pillars. Similarly, to describe the hierarchical structures in Figure 25b, we obtain geometrically:

$$\varphi_l = \frac{\pi d'^2}{4p^2} \quad (15)$$

$$r_l = 1 + \frac{\pi d' h}{p^2} \quad (16)$$

With the two hierarchical levels experimentally considered, four different wetting configurations are possible for each structure, Figure 26 and

Figure 27. Each configuration represents a combination of Wenzel and Cassie-Baxter states at different hierarchical levels, where the first letter of the subscript indicates the state of the base level and the second letter indicates the state of the hierarchical level, W stand for Wenzel state and C for Cassie-

$$\cos\vartheta_{ww} = r_L r_l \cos\theta_0 + r_{TB} r_g \cos\theta_0 \quad (17)$$

$$\begin{aligned} \cos\vartheta_{wc} = r_L (\varphi_l (\cos\theta_0 + 1) - 1) \\ + r_{TB} (\varphi_g (\cos\theta_0 + 1) - 1) \end{aligned} \quad (18)$$

$$\cos\vartheta_{cw} = \varphi (r_g \cos\theta_0 + 1) - 1 \quad (19)$$

$$\cos\vartheta_{cc} = \varphi \varphi_g (\cos\theta_0 + 1) - 1 \quad (20)$$

Baxter state. Stable configuration will be the one with lower energy, for non-hierarchical surfaces this is the state with lower contact angle.

In the following section the equations that predict contact angles in the different wetting configurations are presented. Following [5] each wetting state is shown in Figure 26 or

$$\cos\vartheta_{ww} = r_L r_l \cos\theta_0 + r_{TB} r_g \cos\theta_0 \quad (17)$$

$$\cos\vartheta_{wc} = r_L (\varphi_l (\cos\theta_0 + 1) - 1) \quad (18)$$

Figure 27 is described by $\cos\vartheta_{cw} = \varphi(r_g \cos\theta_0 + 1) - 1$ (19)

equations from $\cos\vartheta_{cc} = \varphi\varphi_g(\cos\theta_0 + 1) - 1$ (20)
 (17) to (20),

corresponding respectively to the contact angles denoted by ϑ_{ww} , ϑ_{wc} , ϑ_{cw} , and ϑ_{cc} .

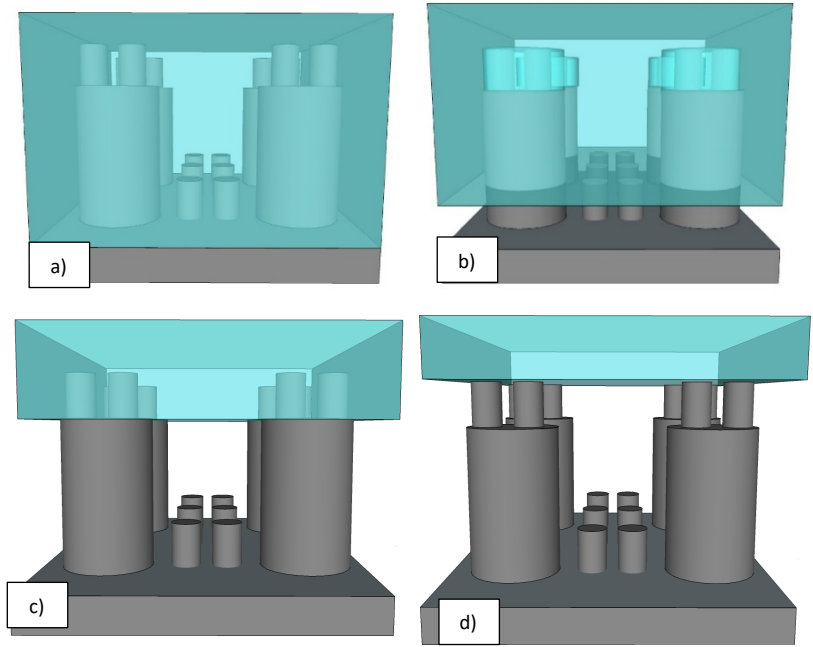
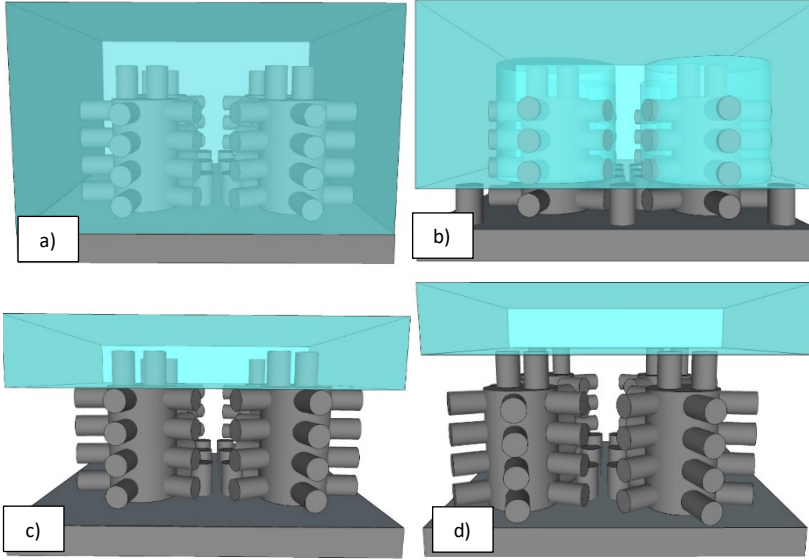


Figure 26: Different wetting states of hierarchical structures of type 1: a) complete wetting or Wenzel state, b) Wenzel state on the surface and Cassie-Baxter state on the pillars, c) Cassie-Baxter state on the surface and Wenzel state on pillars, d) complete Cassie-Baxter state.



b)

d)

$$\cos\vartheta_{ww} = r_L r_l \cos\theta_0 + r_{TB} r_g \cos\theta_0 \quad (17)$$

$$\cos\vartheta_{wc} = r_L (\varphi_l (\cos\theta_0 + 1) - 1) + r_{TB} (\varphi_g (\cos\theta_0 + 1) - 1) \quad (18)$$

$$\cos\vartheta_{cw} = \varphi (r_g \cos\theta_0 + 1) - 1 \quad (19)$$

$$\cos\vartheta_{cc} = \varphi\varphi_g(\cos\theta_0 + 1) - 1 \quad (20) \quad \text{Figure 27: Different wetting}$$

states of hierarchical structures of type 2: a) complete wetting or Wenzel state, b) Wenzel state on the surface and Cassie-Baxter state on the pillars, c) Cassie-Baxter state on the surface and Wenzel state on pillars, d) complete Cassie-Baxter state.

Equations (17) and (18) are valid for the general case of hierarchical surfaces. It is possible to apply them to our surfaces in Figure 26 or

Figure 27: Different wetting states of hierarchical structures of type 2: a) complete wetting or Wenzel state, b) Wenzel state on the surface and Cassie-Baxter state on the pillars, c) Cassie-Baxter state on the surface and Wenzel state on pillars, d) complete Cassie-Baxter state. By imposing respectively $r_l = 1$ or

$$\cos\vartheta_{ww} = r_L r_l \cos\theta_0 + r_{TB} r_g \cos\theta_0 \quad (17)$$

$$\cos\vartheta_{wc} = r_L (\varphi_l (\cos\theta_0 + 1) - 1) + r_{TB} (\varphi_g (\cos\theta_0 + 1) - 1) \quad (18)$$

$$\cos\vartheta_{cw} = \varphi (r_g \cos\theta_0 + 1) - 1 \quad (19)$$

$$\cos\vartheta_{cc} = \varphi\varphi_g (\cos\theta_0 + 1) - 1 \quad (20)$$

$\varphi_l = 1$. Equations (19) and (20) are valid for both kind of surfaces [5, 6]. Furthermore it can be seen that equation (20) was already studied as a particular case of Cassie-Baxter Equation [21].

3.5.2.1 *Computing the area fraction φ for pyramidal pillars*

The realized pyramids are square-base pyramidal elements, Figure 28. Physical dimensions of the tips are not easily calculable, giving rise to problems on computing the area fraction for such a surface.

The monocrystalline structure of the silicon substrate and the high selectivity of the TMAH etch to the crystalline plane leads to a base angle for each pyramidal element of $\alpha=54.7^\circ$ [12]. The roughness parameter, define as the ratio between surface area and projected area, is for overlapping pyramidal elements, as in our case (Figure 28), only a function of the base angle, geometrically:

$$R = \frac{1}{\cos\alpha} \quad (21)$$

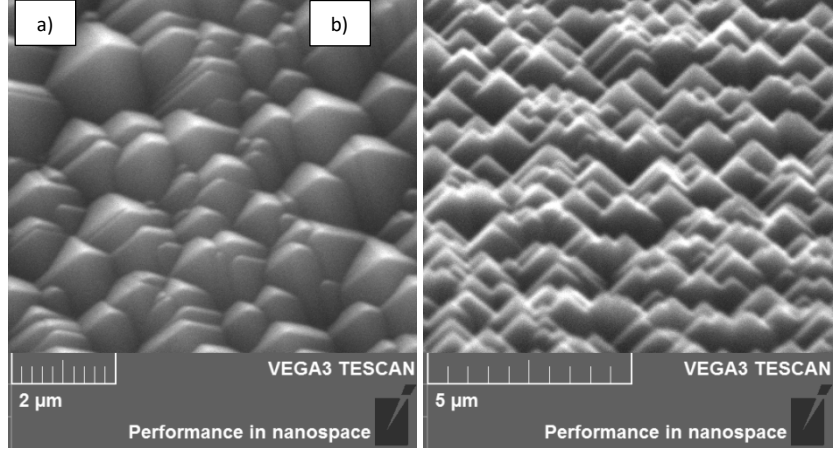


Figure 28: a) Top view of silicon textured surface after five minutes of TMAH. b) 70° tilted view of silicon textured surface.

This fixed value of roughness allow us to predict the apparent contact angle of the textured surfaces in Wenzel state as $\vartheta_w = 124.3^\circ$.

The Cassie-Baxter equation would predict an apparent contact angle of $\vartheta_{CB} \cong 180^\circ$, as the drop is just posed on the top of the pyramidal elements and the area fraction would tend to 0. This situation is described in the following equation:

$$\cos\vartheta_{CB} = \varphi(\cos\vartheta_0 + 1) - 1 \rightarrow -1, \quad (22)$$

if $\varphi \rightarrow 0$

Between these two limits, Equation (23) describes the trend of the apparent contact angle with variable area fraction:

$$\cos\vartheta_{Mix} = \varphi(z)(R\cos\vartheta_0 + 1) - 1 \quad (23)$$

as can be deduced by equation (19).

We define z as the distance between the water surface and the bottom of the pyramidal elements, so that when $z=0$, the system is in the Wenzel state, whereas when $z=h_{max}$ the related hierarchical level is in the Cassie-Baxter state.

Experimentally, the contact angle of the texturized surface is $\vartheta_{Mix} = 135^\circ$. Inserting this value in Equation (23) it is possible to calculate the value of the area fraction. For this configuration the area fraction is $\varphi(z) = \varphi_{Mix} = 0.67$. This value can be used as reference value also in the other Equations (17)-(20). Thus the area fraction value for the hierarchical level is $\varphi_l = \varphi_g = \varphi_{Mix} = 0.67$. Similarly the roughness parameters are $r_l = r_g = R$.

3.6 Results and Discussion

Predictions of contact angles are done inserting the previous values into Equations (17)-(20).

Table 1 shows the predicted contact angle for structures without lateral texturing (of Figure 26). Different structure geometries are analysed and compared with experimental data.

Diameter x Pitch	θ_{ww}	θ_{wc}	θ_{cw}	θ_{cc}	Exp. data
5x10	180.0	180.0	156.1	155.7	160.6
5x15	154.7	180.0	155.9	160.3	161.9
5x20	139.0	180.0	162.0	165.3	164.0
5x25	133.3	180.0	165.6	168.2	171.1

Table 2: Predicted values of contact angle (degrees) compared with experimental data for structures (microns x microns) and configurations of Figure 26.

Non-hierarchical theory shows that the most stable configuration is the one corresponding to the lower contact angle. Hence, the stable states are expected to be described by θ_{cc} , θ_{cw} and θ_{ww} , depending on the geometries. However, experimental data seem to follow the prediction of θ_{cc} even when it is not the most stable state. This behaviour can be explained by the presence of an energy barrier that does not allow the transition from Cassie-Baxter to Wenzel state [26]. The drop is then in a metastable state for these geometries.

Table 3 shows the prediction of contact angles for the surfaces with hierarchy also on the lateral side (

Figure 27), whereas on the rightmost column the experimental data are shown.

$$\cos\vartheta_{ww} = r_L r_l \cos\theta_0 + r_{TB} r_g \cos\theta_0 \quad (17)$$

$$\cos\vartheta_{wc} = r_L (\varphi_l (\cos\theta_0 + 1) - 1) + r_{TB} (\varphi_g (\cos\theta_0 + 1) - 1) \quad (18)$$

$$\cos\vartheta_{cw} = \varphi (r_g \cos\theta_0 + 1) - 1 \quad (19)$$

$$\cos\vartheta_{cc} = \varphi \varphi_g (\cos\theta_0 + 1) - 1 \quad (20)$$

Diam. x Pitch	θ_{ww}	θ_{wc}	θ_{cw}	θ_{cc}	Exp. data
5x10	180.0	180.0	156.1	155.7	160.0
5x15	180.0	180.0	155.9	160.3	158.9
5x20	153.5	180.0	162.0	165.3	164.8
5x25	140.9	180.0	165.6	168.2	167.3

Table 3: Predicted values of contact angle (degrees) compared with experimental data for structures (microns x microns) and configurations of

Figure 27.

Similar considerations valid for the data in Table 2 also apply for those reported in Table 3. In fact, the experimental data are quite similar for the two hierarchical configurations. However,

$$\cos\vartheta_{ww} = r_L r_l \cos\theta_0 + r_{TB} r_g \cos\theta_0 \quad (17)$$

$$\begin{aligned} \cos\vartheta_{wc} = r_L (\varphi_l (\cos\theta_0 + 1) - 1) \\ + r_{TB} (\varphi_g (\cos\theta_0 + 1) - 1) \end{aligned} \quad (18)$$

$$\cos\vartheta_{cw} = \varphi (r_g \cos\theta_0 + 1) - 1 \quad (19)$$

$$\cos\vartheta_{cc} = \varphi \varphi_g (\cos\theta_0 + 1) - 1 \quad (20)$$

the hierarchical configuration with no texturing on the lateral surfaces, Figure 26, display a higher contact angle. This phenomenon could be explained as an increase of the effective upper area due to the presence of the first ring of lateral textured surfaces. Analytical results have shown how the state corresponding to θ_{cc} increases its stability range with respect to that described by θ_{ww} thanks to the presence of the lateral texturing.

From these analyses it is possible to conclude that the experimental results for both hierarchical and non-hierarchical

structures can be validated via the presented hierarchical theory [107], [108]. Furthermore, all the states seem to be metastable Cassie-Baxter configurations.

3.7 Conclusion

In this chapter, a new process to quickly generate large superhydrophobic surface areas composed of hierarchical structures has been presented. By changing the steps order inside the process it is possible to generate two different kinds of structures: patterns with different hierarchical geometries were generated using the two processes. Furthermore, patterns without hierarchy were also generated as references.

All the surfaces were tested for hydrophobicity, and hierarchical structures show a significant improvement of their non-wettability properties with respect to the non-hierarchical ones. Experimental results have been rationalized by applying Wenzel and Cassie-Baxter classical equations extended to consider hierarchy.

Both surfaces composed of hierarchical structures show higher contact angles with respect to surfaces with non-hierarchical posts. The best result shows a contact angle equal to 171° and a tilt angle of 4° , outperforming the wettability of a real lotus leaf.

These values have been observed for the wet plus dry process with pillar diameter of $5\mu\text{m}$ and pitch distance of $25\mu\text{m}$. The production rate of hierarchical surfaces is about 90 minutes per silicon wafer, which leads to an approximate rate of 30 s/cm^2 . Although the best result for tilt angle was obtained from the same surface, it is not possible to deduce significant differences between hierarchical and non-hierarchical surfaces.

This fast and effective method could pave the way to large-scale production of lotus-inspired superhydrophobic surfaces.

4 Combining sharkskin and lotus leaf ability

4.1 Abstract

Hierarchical structures were realized and investigated with the focus on their hydrophobicity and drag-resistance properties. Two lotus leaf-inspired surfaces with different geometrical patterns were realized as a second hierarchical layer on a sharkskin-inspired surface. Properties of hierarchical surfaces have been investigated alongside with both single-level lotus-inspired surfaces and with the bare sharkskin substrate. This paper reports evaluation and cross-comparison of different wettability parameters. Additionally, an energetic theory that addresses losses experienced by a sliding water drop accelerating on a tilted surface has been proposed. Surface analysis is concluded with the measurement of drag resistance under a constant laminar water flow. In all these analyses, hierarchical surfaces showed enhancement of superhydrophobicity and drag reduction. To quantify the overall surface properties a new parameter has been introduced. The hierarchical coupled surface displays superhydrophobicity higher than the lotus leaf itself with a drag resistance almost 3 times smaller than its flat counterpart.

4.2 Introduction

Functional microstructured surfaces that mimic natural ones have been developed for various application in the last few decades, profiting from the advancements in nano- and micro-engineering [109], [110], [117]–[119]. Two particular examples that are widely exploited are superhydrophobic microstructures based on lotus leaves and low drag sharkskin-inspired geometries.

Specifically, the scales of sharks have longitudinal microgrooves that partially suppress a turbulent flow, leading to an increment of swimming speed and lower power consumption. First theoretical models addressing the phenomena were published in early 90s [120] and supporting, during the following two decades, by many experimental studies [65], [66], [121]–[123].

The second class of microstructures addressed in this work is hydrophobic surfaces, inspired by the lotus leaf. This kind of structure features low adhesion, water repellence and self-cleaning (also known as lotus effect [124], [125]). Such properties arise from combination of chemistry and geometrical micropatterns of the surface [25], [45], [115], [126], [127].

In order to combine lotus leaf and sharkskin effects, we designed surfaces that present hierarchical combination of the sharkskin grooves and lotus pillars. Different surfaces composed of

hierarchical and single-level structures have been fabricated and tested. Static contact angle, contact angle hysteresis, tilt angle and pressure drop measured of a water flow along a channel with or without patterned surfaces have been measured. Moreover, energy loss was evaluated observing the acceleration of the sliding water drops along the surface as a function of tilt angle. The results of these measurements supported the development of an energy-base model to predict the behaviour of the drop sliding down a superhydrophobic surface. Finally, a coupled coefficient has been proposed in order to evaluate the superhydrophobic level and drag reduction of a surface. A similar coefficient has been already introduced for superhydrophobic surfaces in [128].

4.3 Materials and Methods

Samples. Our surfaces dataset is composed of five 100 mm long surfaces: three single-level and two hierarchical surfaces. Among single-level surfaces, two are inspired by lotus leaf (L1, L2) and one by sharkskin (Sh). L1 has a square pattern of round pillars of radius $r=0.5\ \mu\text{m}$, and pitch distance $p=4\ \mu\text{m}$. L2 has rectangular base pillars, sides lengths $b_1=0.4\ \mu\text{m}$ and $b_2=1.45\ \mu\text{m}$, and pitch

distances $p_1=2\text{ }\mu\text{m}$ and $p_2=3.25\text{ }\mu\text{m}$. Sh has rectangular base ripples, side lengths $B_1=180\text{ }\mu\text{m}$ and $B_2=40\text{ }\mu\text{m}$, and pitch distances $P_1=200\text{ }\mu\text{m}$ and $P_2=120\text{ }\mu\text{m}$. For rectangular patterns the subscript number 1 identify lengths parallel to the drop or flow motion, whereas the subscript number 2 identify lengths perpendicular to the drop or flow motion. Height of pillars in L1 and L2 is $h=10\text{ }\mu\text{m}$, the height of Sh ripple is $h=40\text{ }\mu\text{m}$. The two hierarchical structures (H1 and H2) are a hierarchical composition of L1 on Sh (H1) and of L2 on Sh (H2). The height of the pillars have been calculated in order to have a stable Cassie-Baxter state [22], using equation (24):

$$\cos \theta = \frac{f - 1}{r_w - f} \quad (24)$$

where θ is the base contact angle, f is the area fraction calculated as $f = \frac{\pi r^2}{p^2}$ for round pillars (r is the radius of the pillar and p the pitch distance), while r_w is the surface roughness calculated as $r_w = 1 + \frac{A_l}{A_a}$, where A_l is the area of the lateral part of the pillar and A_a the apparent area.

The choice of geometrical dimensions for the sharkskin inspired ripples are based on the results obtained by Dean et al. [123].

Surfaces are based on silicon wafers, grain orientation $\langle 111 \rangle$ n-type, using a CMOS pilot line. The CMOS fabrication process is

carried out in a class 100 clean room. Non-hierarchical surfaces are processed using soft lithography and deep reactive ion etching (DRIE) [129]. The process flow for hierarchical structure is more complex, as it requires an oxidation followed by two lithography steps alternate with dry etching steps. Figure 29 illustrates the fabrication flow of hierarchical structures. Quality assessment of the process and features' dimensions is performed using a scanning electron microscope.

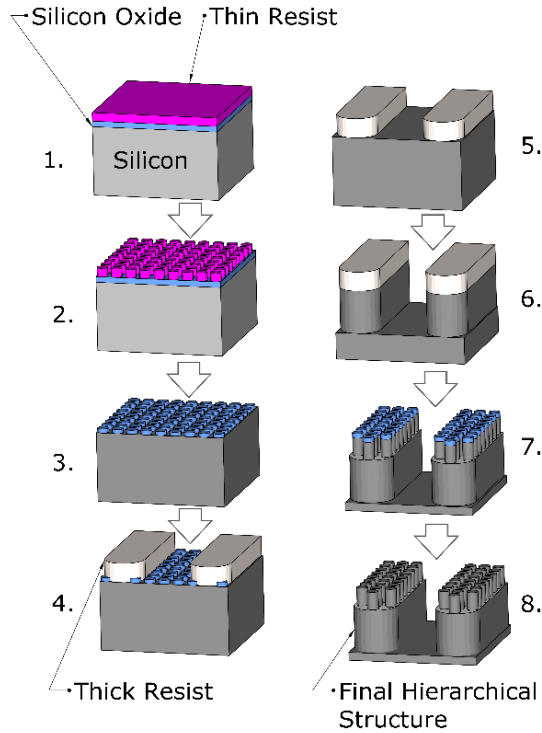
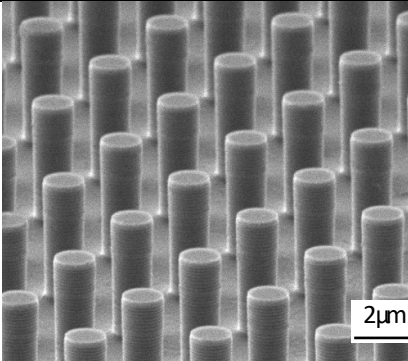
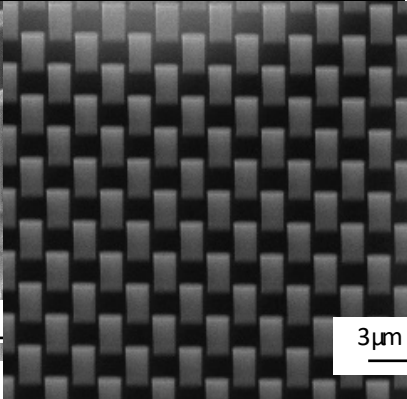
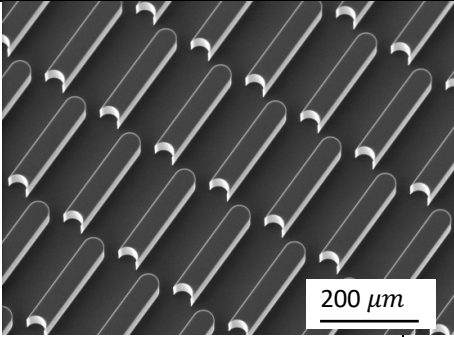


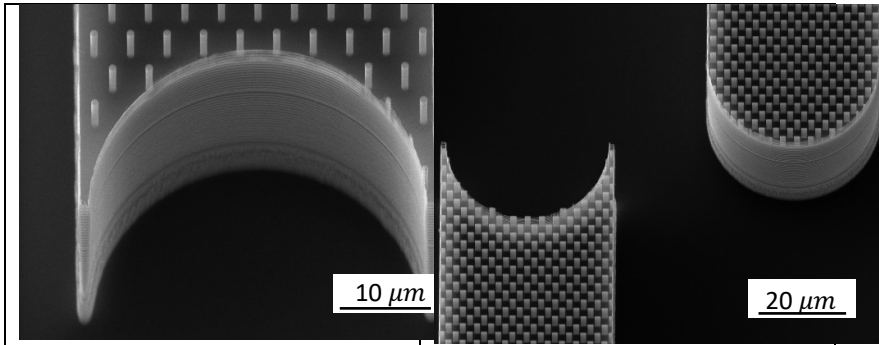
Figure 29: Process flow for fabrication of hierarchical structure on silicon wafer with CMOS-like process. 1. Thermic silicon oxide is grown on the silicon wafer and then coated with thin photoresist, 2. The photoresist is impressed and developed to define the lotus-inspired structure on the second hierarchical level, 3. Silicon oxide is removed with dry etch and the photoresist stripped out with O_2 plasma etching, 4. Thick photoresist is

deposited, patterned and developed to define the sharkskin-inspired structure on first hierarchical level, 5. The silicon oxide is removed by wet etch (HBF), 6. Dry etch of silicon with deep reactive ion etching define the sharkskin-inspired structures, 7. Thick photoresist is stripped with O₂ plasma etching, the pattern of silicon oxide is used as hard mask for define with dry etch the pillar of lotus-inspired structures on the top of sharkskin inspired structure, 8. Silicon oxide is removed by wet etch.

All the surfaces were treated with a self-assembly monolayer of 1-1-2-2-perfluorodecyltrichloro silane (PF3) [96] to enhance the hydrophobicity on the silicon substrate, reaching a base contact angle (CA) of 109°. One sample of sharkskin inspired structure was left uncoated in order to check the dependency of the flow reduction from the substrate hydrophobicity. All the microstructured surfaces have been investigated using a plain silicon surface as a reference. Table 4 summarizes all geometries investigated in this work, three of which are single-level and two of which are hierarchical surfaces.

Table 4: SEM images of surfaces used in this analysis.

L1: 1 μm circle, 10 μm high, 4 μm pitch	L2: 0.4x1.6 μm , 10 μm high, 4 μm pitch
	
SH: 40x200 μm , 40 μm high, 80 μm pitch	
	
H1: SH + L1	H2: SH + L2



Water-surface interaction. The measurements presented in this paper have been performed using deionized water (18 MOhm of resistance). Contact angle measurements were performed on surfaces placed on a flat-levelled base guaranteed the stability of the drop. A fixed focus camera is used to record a grayscale image of a single 3.0 μL drop deposited on the surface. The shape of the drop and the corresponding contact angle was calculated with the Drop analysis plug-in of ImageJ software [114], [130].

Advancing and receding angles were evaluated placing the surfaces on horizontal plane and fixing a needle of a syringe perpendicularly as close to the surface as possible. The volume of water drop deposited on the surface was varied by the syringe while a fixed focus camera was recording the entire process.

These images were analysed to find advancing and receding angles values.

The tilting angle was measured using a tilting plane operated by a stepper motor (resolution 0.18°). 5 µl drops of deionized water were placed on horizontally aligned surface, which then was slowly tilted up to the angle at which the drop starts to roll. For each surface, the measurement was repeated several times for both positive and negative angles (in order to eliminate any systematic error of the 0-angle alignment).

The acceleration of a drop on a tilted plane is measured with a setup based on infrared LED-photodiode pairs. Each pair was placed along the drops path acting as optical gate. The angle of the plane was set by a stepper motor, and the signal from photodiodes was processed with a microcontroller providing time measurements with a 0.7 ns resolution. The distance between 0.5 mm wide gates was calibrated down to 0.1 mm precision. For each surface, the tilting angle was parametrized between 1° and 45°, with 5 measurements per step. Acceleration of the drop was calculated using square equation fit of the time signal from the gates with $\chi^2 > 0.99$.

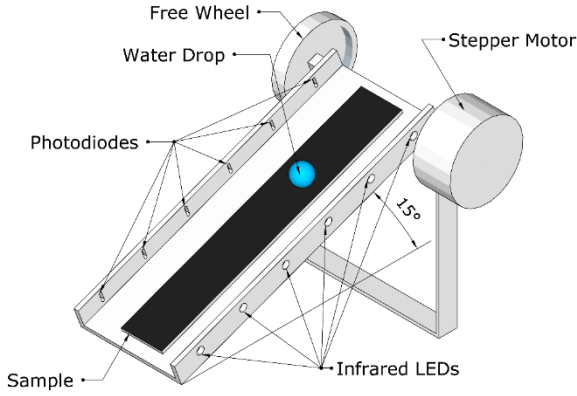


Figure 30: Illustration of the setup used to measure the acceleration of a moving drop on superhydrophobic surfaces at different angles.

Drag measurement. Although drag resistance of a surface cannot be measured directly, it can be estimated through the relationship between drag and pressure loss in fluid (typical dimension is in tens of a Pascal). The relationship is summed up with the following equations [131]:

$$\Delta p = \frac{\rho V^2 f_r L}{2D_H} \quad (25a)$$

$$f_r = \frac{k}{Re} = \frac{k\eta}{VD_H} \quad (25b)$$

where D_H is the hydraulic diameter, ρ the fluid density, V the mean flow velocity, f_r the friction factor, L distance between the two points in which pressure is measured, Δp is the pressure difference between the two points, η is the viscosity and k is a “drag resistance” constant, measured for laminar flow in a squared channel composed of flat hydrophilic surfaces as $k = \frac{64}{\frac{2}{3} + \frac{11H}{23W} \left(2 - \frac{H}{W}\right)}$. Hydraulic diameter is a geometrical property of a chamber and for a rectangular section $D_H = \frac{2WH}{W+H}$.

The experimental setup is shown in Figure 31. The chamber was designed to host two microstructured silicon chips at a precise distance in-between ($H=0.75$ mm) with the constant width ($W=5$ mm) along all the channel. The total length of the chamber is 110 mm and the distance $L=70$ mm. The total length of the chamber exceeds the measuring distance in order to guarantee a fully developed flow between the two measurement points. A 50 cc glass syringe driven by an automatic syringe pump was used to generate constant water flow through the chamber. The pressure drop was registered with an air-to-air differential manometer with a digital interface at ~ 1 kcps sampling rate and resolution of 0.1 Pa.

The experimental measurements included 3 different stages with different flowrates: 100, 200, and 300 $\mu\text{l/s}$. A hydrophilic flat surface has been tested together with the microstructured ones in order to match the theoretical prediction of the formula of equation (25b) and validate the experimental setup.

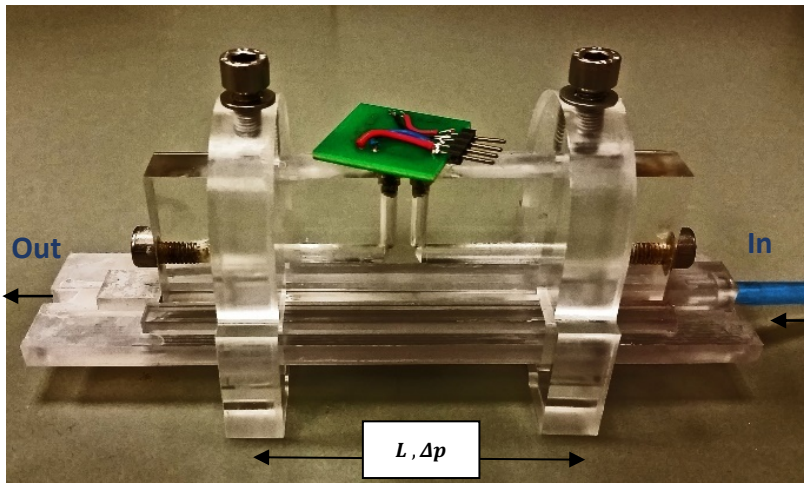


Figure 31: Experimental chamber for the measurement of the pressure drop along rectangular channel.

4.4 Results

Values of contact angles measured with the sessile drop method have been compared with the contact angle values calculated with the Cassie-Baxter equation [21], comparison is shown in Figure 32. Surfaces that have been coated with PF3 match the trend of theoretical values. On the other hand, sharkskin sample without PF3 coating does not, and as expected it wets completely the surface [45].

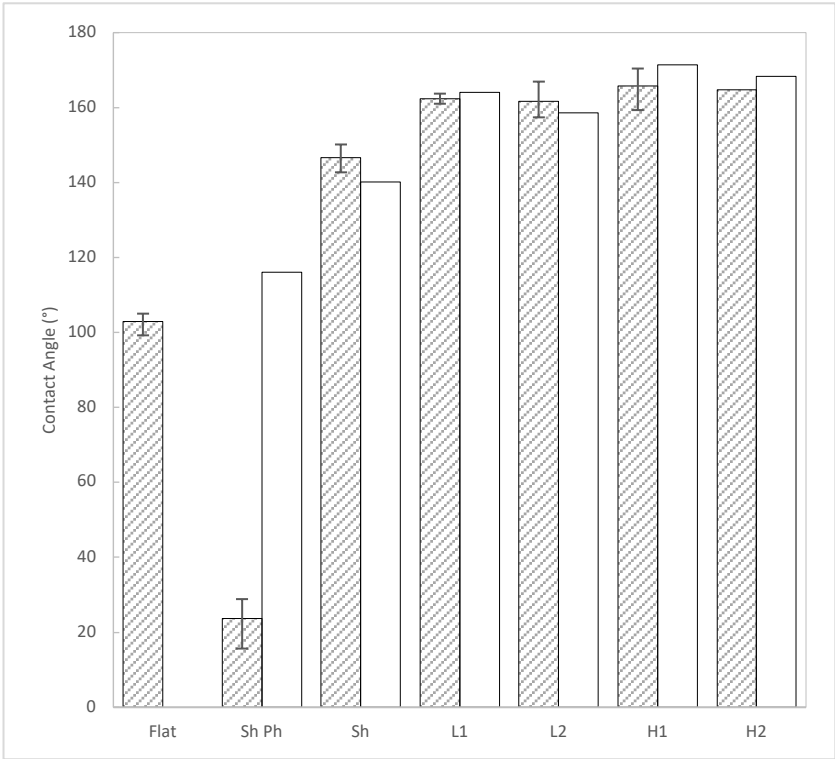


Figure 32: Contact angle values (stroked bars) compared with the values predicted by Cassie-Baxter equation (blank bars).

The first bar on the left of the graph shows the values of contact angle on flat silicon surface coated with our hydrophobic

coating. Sharkskin inspired structures do not reach the hydrophobicity threshold of 150° [132], while the microstructured surface (L1, L2) and hierarchical surfaces (H1, H2) have contact angle values between 160° and 170° . As expected, range of angles reported for the values in the hierarchical structures is greater than the simple microstructured one. That is in accordance with the concept that hierarchy can enhance the properties of the surfaces [108].

Table 5 reports the values of advancing and receding contact angles (in the next section, on Figure 33: Tilting angles values for different surfaces., these values are cross-compared with the data from the tilting angle).

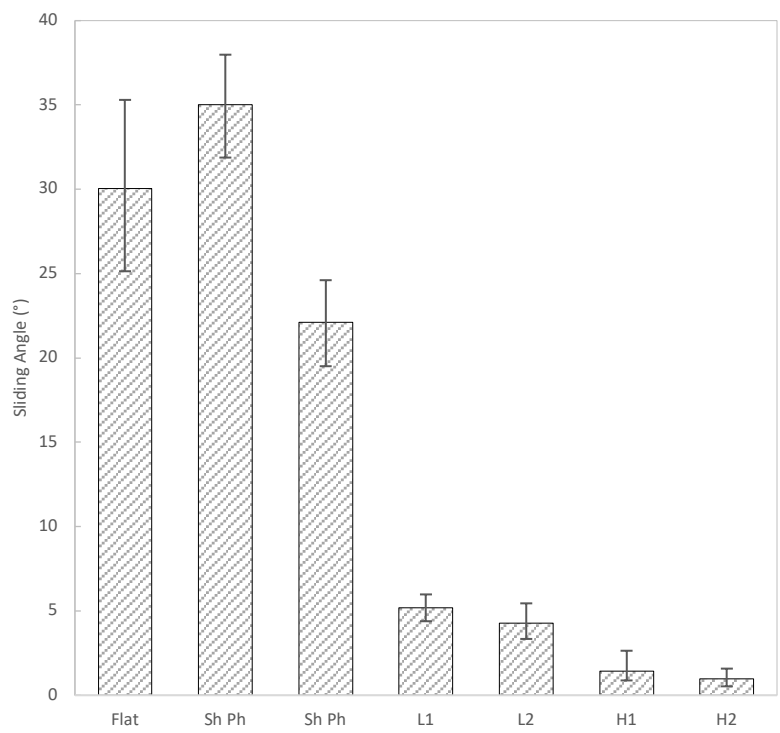


Figure 33: Tilting angles values for different surfaces.

Table 5: Advancing and receding angle values.

	AVERAGE-CA (°)	ADVANCING ANGLE (°)	RECEDING ANGLE (°)
FLAT	99.0	115.4	82.6
SH PH	16	33.9	0
SH	148.8	162.1	135.6
L1	161.4	166.4	156.4
L2	159.3	163.4	155.2
H1	163.1	164.4	161.8
H2	164.0	165.0	163.0

The flat and hydrophilic surfaces (SH, PH) required a significantly bigger drop of 20 μl in order to evaluate the sliding angle. The Sh surface has a tilting angle greater than 20° , meaning that this surface cannot be considered as superhydrophobic. The two lotus structures have good value of a tilting angle below 5° and the hierarchical structures have tilting angle lower than 2° . As expected the wettability properties of complex structures is improved by the hierarchy.

To calculate the acceleration of drops of water on tilted plane, drops were placed on an inclined surface and the acceleration of the drop was measured based on a signal from optical gates. The

plot in Figure 34 shows the experimental data of the acceleration against the angle of inclination.

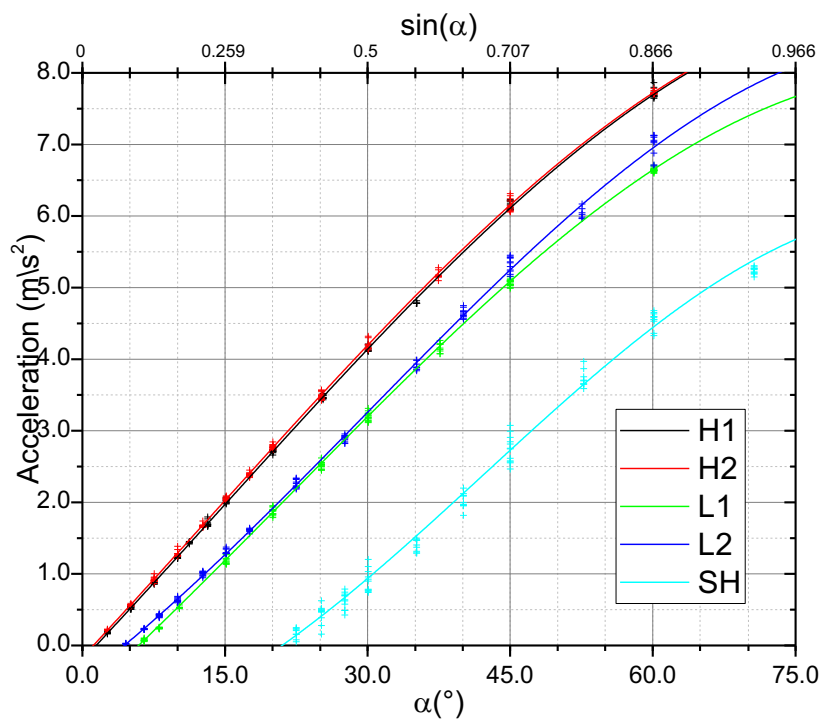


Figure 34: Data and fitting of the acceleration values.

The acceleration increases almost linearly with the tilt angle. The data are then analysed with an energy base approach, covered in the Discussion section.

Water skin-friction on the surfaces was evaluated through the pressure difference between the ends of a rectangular channel. Three constant water flow rates have been evaluated (Figure 35). For a channel with a given constant cross-section, the pressure drop is proportional to the flow rate (equation (25)). For a pipe with hydrophilic smooth walls the friction factor can be calculated analytically (Figure 35, black line).

In order to validate the setup, a hydrophilic flat surface has been tested and compared with this theoretical trend (Figure 35, crosses): it is predicted to be linear, see equation 25, noting that the flow rate is defined as $Q=AV$. As can be seen, the agreement of the data confirms the consistency of the experimental setup. From the different slopes the friction factor or better the drag resistance constant (k) can be evaluated. Sharkskin-inspired surface has low drag resistance and, although it is less hydrophobic than the L1 and L2 surfaces. The best results are given by the hierarchical structures that manage to combine the superhydrophobicity of lotus-inspired structures with the peculiar shape of sharkskin-inspired structures.

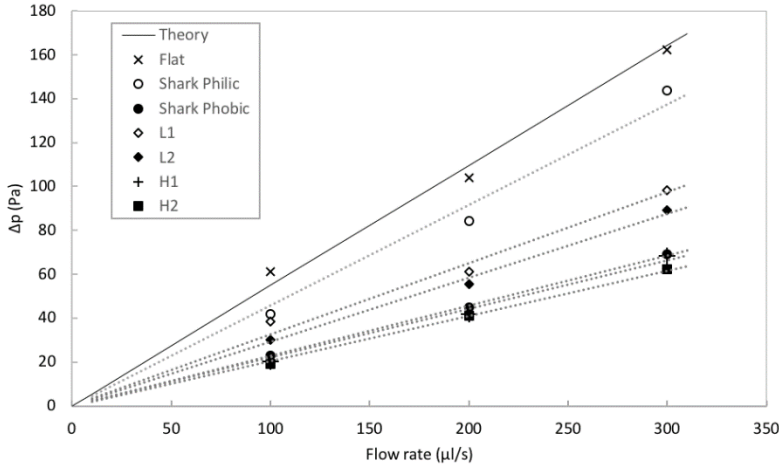


Figure 35: Pressure drop versus flow rate for the different analysed surfaces. The average standard deviation for each measurement is 0.4. The linear experimental trend observed with our apparatus is in agreement with the theoretical prediction of equation (25) and with the theoretical value of the constant k , i.e. 80.7 for our rectangular flat surface of 0.7 mm by 5 mm; from each slope related to a specific patterned surface we thus extract the related drag reduction constant, see inset.

4.5 Discussion

Contact angle hysteresis and tilting. A superhydrophobic surface, in which the drop is floating on the top of the pillars

[133], can be treated as a surface with strong diluted defects [12]. In this case the pinning of the droplet triple line is limited to the pillars' top surface. In order to start moving along an inclined plane, the gravitational force acting on the drop has to overcome the capillary force [134] $\rho V g \sin \alpha \geq \pi d \gamma \Delta \cos \theta$, where α is the inclination of the plane and d is the drop contact radius. The contact radius can be calculated considering that a water drop deposited on superhydrophobic surface presents a nearly (the exact calculation would give a discrepancy of less than 1%) spherical shape if its radius is smaller than the capillary length, k^{-1} . In this condition the radius of the drop can be calculated as $R = \sqrt[3]{\frac{3}{4\pi} V}$, and the drop contact radius as $d = R \sin \theta_{app}$, where θ_{app} is the static apparent (Wenzel or Cassie-Baxter) contact angle.

From these equations the connection between the tilting angle and the contact angle hysteresis $\Delta \cos \theta$ is found by imposing the limit condition on the force equilibrium:

$$\sin \alpha = \frac{\pi d \gamma}{\rho V g} \Delta \cos \theta \quad (26)$$

This equation shows a linear correlation between the contact angle hysteresis and the tilting angle. For a given liquid, the only not-stated variable in this equation is the contact radius that for

small drop ($R < k^{-1}$) can be calculated using the static contact angle. As stated by Cassie-Baxter equation [21] the contact angle depends on the solid-liquid area fraction φ . For a rectangular array of round pillars we can express the area fraction as: $\varphi = \frac{r^2}{p^2}$, where r is the radius of the pillars and p the pitch distance (between two pillars).

We would like now to estimate the hysteresis based on the geometrical parameters of the structures that compose the surfaces. For cylindrical pillars, the theory has already been developed in [12], a set of two equation is used for this analysis:

$$\begin{cases} \gamma \Delta \cos \theta = \frac{\varepsilon}{p^2} \\ \varepsilon \approx \frac{1}{2} a_* A_{sp} \gamma \ln \left(\frac{p}{r} \right) \end{cases} \quad (27)$$

where ε is the energy required to detach water triple line from a single pillar, a_* is a parameter that depends on the line distortions, r is the radius in case of round pillar or half of the length of the pillar width perpendicular to the droplet motion and A_{sp} is the top area of the pillars (πr^2 for circular pillars). From the set of equations (27), it is noteworthy that contact angle hysteresis has a logarithmic dependency from the

pillar/defect density, which justifies how few defects can generating remarkable hysteresis. Furthermore, for a given liquid we can obtain a function that relates contact angle hysteresis with the geometrical parameter of the surface, taking into account the definition of $\varphi = A_{sp}/p^2$:

$$\Delta \cos \theta \approx \frac{1}{2} a_* \varphi \ln \left(\frac{p}{r} \right) \quad (28)$$

Taking into account the area fraction, for cylindrical pillars we can predict the contact angle hysteresis from $\Delta \cos \theta_{L1} \approx \frac{1}{4} a_{L1} \varphi_{L1} \ln \left(\frac{\pi}{\varphi} \right)$ [12]. This equation applies only to cylindrical pillars, i.e. L1 surface. In order to adapt the equation to the rectangular pillars and the hierarchical structures, we have to consider the area fraction of each surface.

For rectangular pillars $\varphi_{L2} = \frac{b_1 b_2}{p_1 p_2}$ where 1 and 2 indicate the direction parallel and perpendicular the drop movement, giving $\Delta \cos \theta_{L2} \approx \frac{1}{2} a_{L2} \varphi_{L2} \ln \left(\frac{2p_2}{b_2} \right)$. Similarly, for sharkskin-inspired structure $\varphi_{Sh} = \frac{B_1 B_2}{P_1 P_2}$, and $\Delta \cos \theta_{Sh} \approx \frac{1}{2} a_{Sh} \varphi_{Sh} \ln \left(\frac{2P_2}{B_2} \right)$. For hierarchical structures the total area fraction can be derived by multiplying the area fraction of each single-level structure [108]. The hierarchical surface H1 has area fraction $\varphi_{H1} = \varphi_{Sh} \varphi_{L1} = \frac{B_1 B_2}{P_1 P_2} \frac{\pi r^2}{p^2}$ leading to $\Delta \cos \theta_{H1} \approx \frac{1}{4} a_{H1} \varphi_{H1} \ln \left(\frac{\pi B_1 B_2}{\varphi_{H1} P_1 P_2} \right)$, where

$a_{H1} = a_{L1}a_{sh}$. For the hierarchical structure H2 the area fraction is $\varphi_{H1} = \varphi_{sh}\varphi_{L1} = \frac{B_1B_2}{P_1P_2} \frac{b_1b_2}{p_1p_2}$ leading to $\Delta\cos\theta_{H2} \approx \frac{1}{2}a_{H2}\varphi_{H2} \ln\left(\frac{B_1B_2}{P_1P_2} \frac{2b_1}{p_1}\right)$, where $a_{H2} = a_{L2}a_{sh}$. Related best fitted values of the line distortion parameters are: $a_{L1} = 1.1$, $a_{L2} = 0.7$ and $a_{sh} = 0.8$ from where we calculate $a_{H1,2} = a_{L1,2}a_{sh}$.

The comparison of data calculated from these equations with the experimental values gives good results, Figure 36.

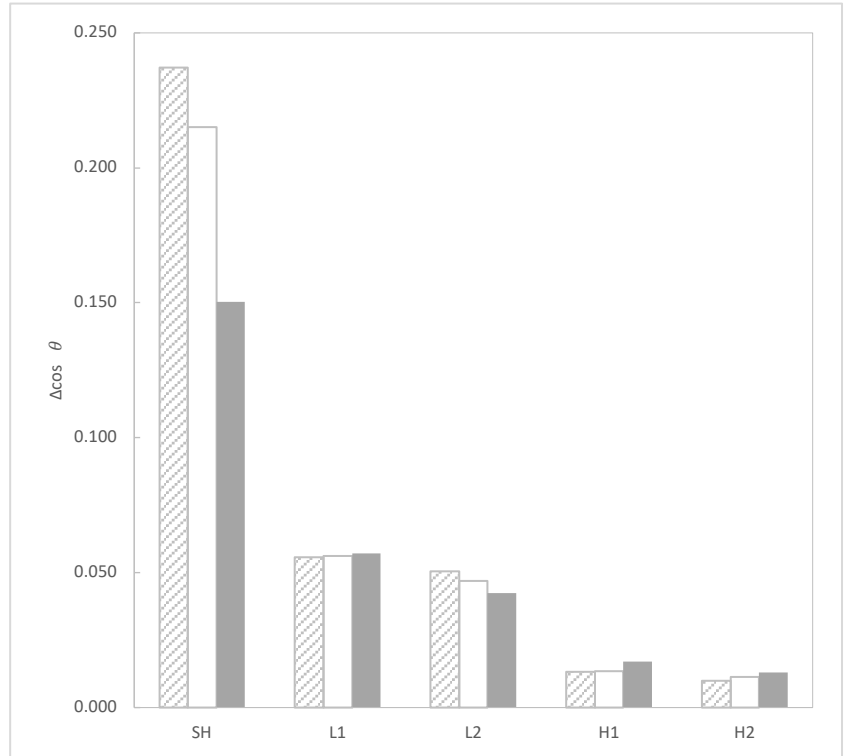


Figure 36: Contact angle hysteresis ($\Delta \cos \theta$) calculated from advancing-receding (stroked bars), from geometrical parameter of the surface (blank bars) and derived from tilting angle analysis (solid-filled bars).

Energy dissipation of a drop rolling on inclined plate. We used an energy approach to evaluate non-conservative energy dissipated by a water drop moving along an inclined plate.

A drop that moves on an inclined plate slides and rolls [135]–[141]. The total energy of moving drop can be described in terms of gravitational energy (E_u), sliding kinetic energy (E_{ks}) and rolling kinetic energy (E_{kr}). The energy dissipated by the movement of the drop along an inclined plate can be described as the difference of the initial total energy and the final total energy of the drop, i.e. $E_{NC}=E_{TOT,f}-E_{TOT,i}$, where E_{NC} is the non-conservative energy and $E_{TOT}=E_u+E_{ks}+E_{kr}$, thus:

$$E_{NC} = (E_{U,f} + E_{KS,f} + E_{KR,f}) - (E_{U,i} + E_{KS,i} + E_{KR,i}) \quad (29)$$

The non-conservative energy of a droplet, on a plate of length l and inclined of an angle α , is described by the following equation:

$$E_{NC} = \frac{1}{2}mv_f^2 + \frac{1}{2}I\omega_f^2 - \frac{1}{2}mv_i^2 - \frac{1}{2}I\omega_i^2 - mgl \sin \alpha \quad (30)$$

where m is the mass of the drop, g is the gravitational acceleration, v is the velocity at initial (i) and final (f) points, I is the inertia of the drop (considered as a sphere, i.e. $I=2/5mr^2$) and ω the corresponding rotational speed.

In our experiment the following parameters were used: 5 μ l drops travelled on 10 cm long inclined plane, at tilting angles α

ranging from 2° to 60° . The capillary length $k^{-1} = \sqrt{\frac{\gamma}{\rho g}} \sim 2.7 \text{ mm}$, where ρ is the liquid density and γ the surface tension at room temperature. Since k^{-1} is greater than the drop radius, the capillary force governs the drop behaviour rather than the gravitational force. Furthermore, the drop shape can be approximated with a sphere [137].

Mahadevan and Pomeau [137] showed that in order to have viscous effects that overcome the inertia (hence the drop rolls instead of sliding), a small Reynold number is required, such as $Re < 1$ [135]. Imposing this condition to a water drop leads to an angular velocity of 0.94 rad/s . Similar low angular velocities have also been observed experimentally using different techniques [139], [140]. At this low angular speed, the kinetic energy linked to rolling is six orders of magnitude lower than the other energetic terms present in equation (30). Neglecting the contribution of rolling kinetic energy in equation (30) becomes:

$$E_{NC} = \frac{1}{2}mv_f^2 - \frac{1}{2}mv_i^2 - mgl \sin \alpha \quad (31)$$

During the movement, the energy of the sliding drop is dissipated through two main mechanisms: internal viscous flow and pinning/depinning of the drop from the surface. At low inclination angles, close to the tilting angles value, the main dissipation mechanism is the depinning of the water triple line

of the rear part of the moving drop. This mechanism has been studied in detail by several authors [12], [128], [142]–[144].

To evaluate the work of the pinning/depinning, we use the energy dissipated by a drop of contact width $w=2r$ that moves at a speed v [142]:

$$P_d = nW_s wv \quad (32)$$

in which $n=1/p^2$, and p is the pitch distance between two pillars orthogonal to the movement direction. The work per unit area can be estimated with the following equation:

$$W_s = \frac{\gamma}{n} (\cos \theta_r^{app} + 1) \quad (33)$$

where θ_r^{app} is the apparent receding angle.

To evaluate the energy losses from pinning/depinning E_{PD} , equation (32) needs to be integrated over the sliding time since the velocity (v) is not constant, namely:

$$E_{PD} = \int_{t_i}^{t_f} P_d dt = nW_s w \int_{t_i}^{t_f} v dt \quad (34)$$

where t_i and t_f are the time instants at which the drop reaches the initial and final measuring points (first and last optical gates).

Since our experiments showed that the drop moves with a nearly constant acceleration a (square equation fit of 10 points yields in $\chi^2 > 0.99$), equation (34) can be solved as:

$$E_{PD} = nW_s w \frac{at^2}{2} \Big|_{t_i}^{t_f} \quad (35)$$

We can calculate the energy spent in viscous dissipation (E_q) using the following equation (36) from [137]. This equation represents the energy balance between potential energy and viscous dissipation:

$$U \frac{4}{3} \pi R^3 \rho g \sin \alpha = \mu \int_{V_d} (\nabla \vec{v})^2 dV \quad (36)$$

where V_d is the volume in which viscous dissipation occurs, μ the dynamic viscosity, U the velocity of the centre of mass, g the gravitational acceleration, ρ the density of the liquid, R the radius of the drop, and $\nabla \vec{v}$ - the gradient of the velocity field in the droplet. To evaluate \vec{v} we consider that the drop slide without rolling, and that the velocity profile inside the drop respects the sticky condition at the wall. This hypothesis is validated by the direct observation of a sliding drop made in [140]. The integral over the volume can be seen as a triple integral over the three principal directions, considering that the velocity inside the droplet is constant on planes parallel to the surface, whereas the

velocity has a gradient only along the direction normal to the surface. Furthermore, if we consider viscous dissipation effects on a volume of height h , the energy rate (power) dissipated by viscous forces can be expressed as [34]:

$$\begin{aligned}\dot{E}_{fl} &= \mu \iiint_{xyz} (\nabla \vec{v})^2 dx dy dz = \mu A_c \int_z (\nabla \vec{v})^2 dz \\ &= \mu A_c \int_0^h (\nabla \vec{v})^2 dz\end{aligned}\tag{37}$$

where x and y are arbitrary perpendicular coordinates on the surface, z is the direction normal to it and A_c is the contact area of the drop. Along the direction normal to the surface, the velocity profile varies linearly from zero to U [128], so we can approximate $|\vec{v}| = \frac{U}{h}z$, so $|\nabla \vec{v}| = \frac{U}{h}$. To find the total energy dissipated along the sliding length L , we need to integrate over the sliding time. The only variable in the equation that depends on time is U , that can be express as $U = at$, where a is the constant acceleration along the inclined plane and t is the time calculate at the measurement gate. Accordingly:

$$\begin{aligned} E_{fl} &= \int_{t_1}^{t_2} \dot{E}_{fl} dt = \frac{\mu A_c}{h} \int_{t_1}^{t_2} (at)^2 dt \\ &= \frac{\mu A_c}{h} a^2 (t_2^3 - t_1^3) \end{aligned} \quad (38)$$

The sum of equations (35) and (38) gives the total energy dissipation inside the drop. The total energy dissipation is the result of losses by pinning/depinning mechanism and by viscous flow inside the drop. Furthermore, the total energy dissipation has to be equal to the total energy consumed by the droplet while it moves from initial to final point of our inclined plane, see equation (31).

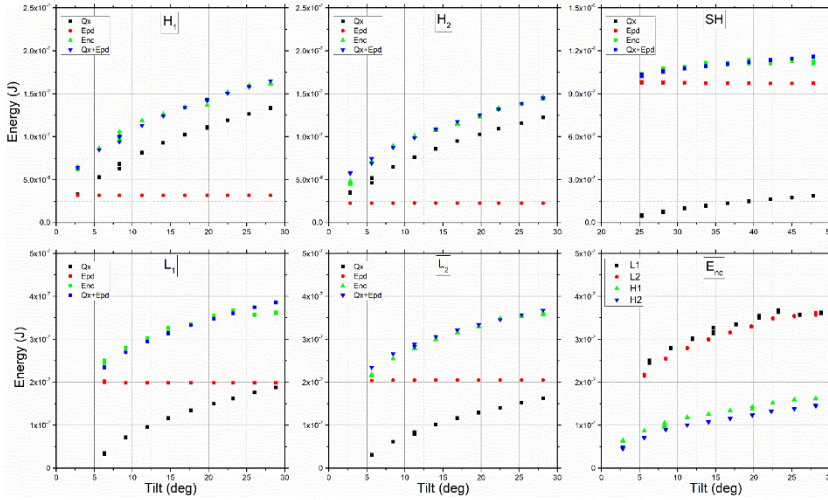


Figure 37: From right to left, top to bottom the graphs 1 to 5 compare for each surface the non-conservative energy (green triangles) with the total losses calculated for a sliding drop (blue inverted triangles). Each sub-plot shows the energy spent for pinning/depinning mechanism (red circles) and for shear stress inside the drop (black square). The last graph shows a comparison of the measured non-conservative energy in the system for the four superhydrophobic surfaces (L1, L2, H1 and H2).

The comparison between the non-conservative energy and the total losses of a moving drop are depicted in the Figure 37. Bottom-right plot shows the non-conservative energy of a moving drop on the four superhydrophobic surfaces: L1, L2, H1 and H2. The other five graphs show the comparison between the measured non-conservative energy and the sum of E_{pd} and E_{ff} .

The viscous forces act on a volume inside the drop that is characterized by a characteristic height, h . The value h is not known a priori so it has been used as a fitting value in our model. The parameter h has been fitted taking into consideration that at the lowest velocity (smaller angle) the viscous dissipations can be neglected to respect the dissipation from pinning/depinning.

A further consideration has to be done, since h is an effective value (Figure 38, left), useful to evaluate the velocity gradient where an effective no-slip condition is imposed at the solid-liquid boundary to simulate a more complex two parameter description (Figure 38, right).

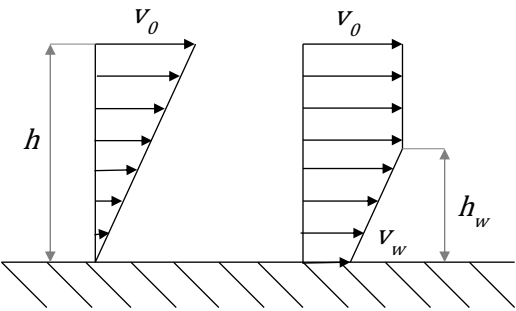


Figure 38: Scheme of water-solid surface interaction. On the left, a no-slip condition in which the gradient of velocity depends only on the velocity at the center of mass, v_0 , and the height, h . On the right velocity profile with slip velocity different to zero, the velocity gradient depends on the velocity of at the wall, v_w , the center of mass, v_0 , and the interaction height, h_w . Here we consider an effective h value describing both the two parameters h_w , v_w .

Table 6: Height of interaction, h , with the viscous loss inside the drops. This coefficient has been estimated from experimental data.

	L1	L2	H1	H2	Sh
H	41	50	43	54	110

In our experiments, the non-conservative energy starts to decrease at angles exceeding 30° . This behaviour can be explained by the dependency of the losses for pinning/depinning on velocity. In fact, the energy dissipated by the triple line should decrease with increasing speed. This depends on the fact that the water bridge between the pillar top and the drop has enough time to complete the elongation before rupture, and on the other hand it becomes “brittle” with speed [142]. Graphs 2 to 5 show the comparison between the non-conservative energy (E_{NC}) of the system with the losses of the moving drop ($E_{fl}+E_{PD}$) for each surface. Furthermore, also the energy dissipated for pinning/depinning and for internal losses is shown for each surface. A further step is still required in order to complete the understanding of surfaces with hierarchical structures: the energy dissipated by pinning/depinning depends linearly on the drop diameter (parallel to the drop motion). The apparent width of the drop has to be divided by factor three for our hierarchical surfaces. As a matter of fact, one third is the ratio between the actual width in which the drop is in contact with the second hierarchical level and the total width. Figure 39 shows the total width (continuous line) and the actual width (dashed line).

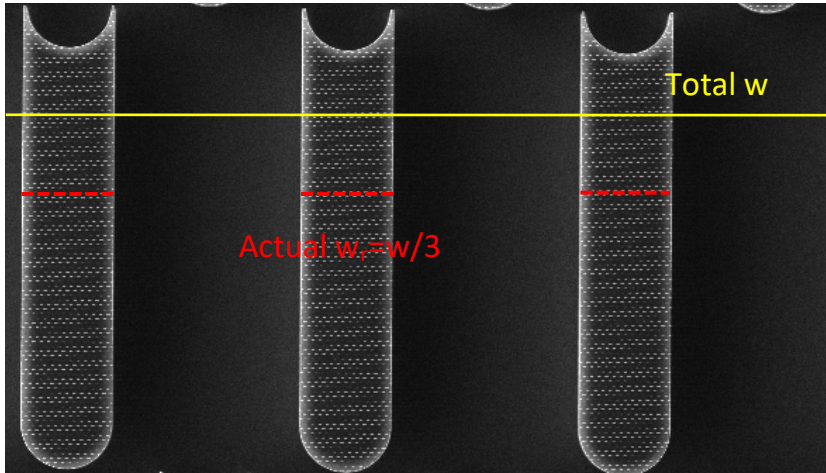


Figure 39: SEM image of the hierarchical surfaces (H2) taken parallel to the surface. The continuous yellow line represents the apparent width and the dashed red line the actual width used in Equation 3 to evaluate the pinning/depinning losses of a moving drop.

All the tests reported within this work evaluate different aspects of superhydrophobicity, however, each of these parameters alone is not sufficient to evaluate overall surface quality. Alternatively, some of them can be united, e.g. done by [19], providing a simpler way for cross comparison. In the work, authors introduced a new surface parameter,

b_{sh} , based on pinning/depinning energy. Following this idea, we introduced a similar coefficient c_{mf} , that depends on both surface energy (E_{pd}) and internal energy losses (E_{fl}).

The first part of the coefficient is linked to pinning/depinning energy. In order to obtain an experimental-independent value, the E_{pd} of a drop (equations (33) and (34)) was normalized by sliding area ($w \cdot l$): $c_{mf1} \sim (\cos \vartheta_r^{app} + 1)$.

The second part is related to the viscous losses. The total energy of the internal flow (eq. (38)) is normalized again by parameters that depend on experimental conditions, such as sliding area and drop velocity: $c_{mf2} \sim \frac{R}{h} \sin \vartheta_{app}$.

Since both of these parameters are dimensionless and monotonically decreasing (for angles between $\pi/2$ and π), we phenomenologically combined them as:

$$c_{mf} = (\cos \vartheta_r^{app} + 1) \frac{R \sin \vartheta_{app}}{h} \quad (39)$$

In ideal case, for a spherical drop with no contact angle hysteresis the coefficient will tend to zero, meaning that no energy would be required to move the drop.

In the following table the value of the coefficient is summarized for all the surfaces, confirming the superiority of sample H2.

Table 7: Multifunctional coefficient tabled for each surface.

	L1	L2	H1	H2	SH
C_{mf}	0.67	0.62	0.33	0.24	1.51

Chamber flow. The analysis of the surfaces under steady-stay flow in small rectangular channel shows how hierarchy is also useful to reduce skin-friction. The following analysis uses the drag resistance constant k and the slip length b as parameters to evaluate the performance of each surface.

Drag resistance constant. The drag resistance constant, k , obtained combining equation (a) and (2b) includes both the geometrical resistance of the chamber and the skin friction on the surface:

$$k = \frac{2\Delta p D_H^2}{\rho V L} \quad (40)$$

where V is the mean velocity in the chamber; obtained as the flow rate divided by the area of the cross-section. Since $\Delta p \sim V$ and all the other terms of the equation are constant for a fixed channel geometry, the drag resistance constant depends only on the skin friction of the different surfaces.

Table 8: Values of drag resistance constant k for different surfaces.

	<i>Th.</i>	<i>Flat</i>	<i>L1</i>	<i>L2</i>	<i>H1</i>	<i>H2</i>	<i>Sh</i>	<i>Sh</i>
	<i>Val.</i>							<i>Ph</i>
k	80.6	79.6	47.9	43.0	32.5	30.3	33.7	67.5

Table 8 reports the drag resistance constant calculated on the basis of a linearization of the data set, imposing that at zero flow rate the pressure drop is zero. It can be notice that an empirical correlation relates the friction coefficient of the single-level structures with respect to the hierarchical structures:

$$k_h \cong k_1 - \varphi_2 k_2 \quad (41)$$

where k_h is the drag resistance constant of the surface with hierarchical structure, k_1 the drag resistance constant of the single-level surface with only the base hierarchical level, φ_2 the area fraction of the single-level surface that compose the second hierarchical level, and k_2 the drag resistance constant on the second hierarchical level. The difference between k_{H1} and k_{H2} calculated with equation (41) and the experimental values are respectively 3.9% and 1.4% respectively.

Slip length. For viscous fluids in relative motion with respect to a flat surface it is often assumed that the relative velocity between wall and fluid at the interface is zero, the so called no-slip condition. The no-slip condition holds usually for hydrophilic and hydrodynamically flat surfaces [145]. In contrast, superhydrophobic surfaces have been observed to have nonzero slip length [65]. In our case the slip length for superhydrophobic

and sharkskin-inspired surfaces in rectangular channel and laminar flow [121] can be expressed as:

$$b = \frac{c\eta QL}{\Delta p WH^2} - \frac{H}{3} \quad (42)$$

The empirical constant c can be obtained by imposing the no-slip condition for the flat hydrophilic surfaces. In our case this results in $c = 4.4$; then the slip lengths for all the other surfaces (L1,1, H1,2 and Sh) using equation (42) with this value. The slip length, of a channel with a given geometry, is a property of the surface and does not depend of flow velocity, this can be observed considering $b \sim Q/\Delta p$ and $\Delta p \sim v \sim Q$.

Table 9: the table presents the slip length values b (μm) for the surfaces tested. For the flat hydrophilic surface the no-slip condition holds, and the slip length is equal zero.

	Flat	L1	L2	H1	H2	Sh	Sh philic
b	0	154.3	198.6	337.7	380.4	317.8	41.9

Table 9 shows the data of slip lengths for the surfaces analysed., Starting from the values of slip lengths of the single-level

surfaces it is possible to phenomenologically estimate the slip length of a hierarchical surface, as:

$$b_h \cong b_1 + \varphi_1 b_2 \quad (43)$$

The values of b_{h1} and b_{h2} calculated using this equation diverge from experimental results respectively of 7.2% and 0.8%.

4.6 Contact angle variation on directional patterns

In this paragraph, we will show interesting property of sessile drops deposited on non-isotropic composite interface. The term non-isotropic in this context means that the linear quantity of area fraction on x-direction is different from the one on y-direction, as the pattern depicted in Figure 40. We observed that a drop deposited on such pattern has different values of contact angle when measured along either x- or y- direction. Similar phenomenon has been observed in superhydrophobic surfaces with patterns that feature a wettability gradient along one direction [146]. On those surfaces the contact angle gradient allows the drop to move; in the case of non-isotropic wettability properties, the drop cannot move, but a contact angle gradient will still exist.

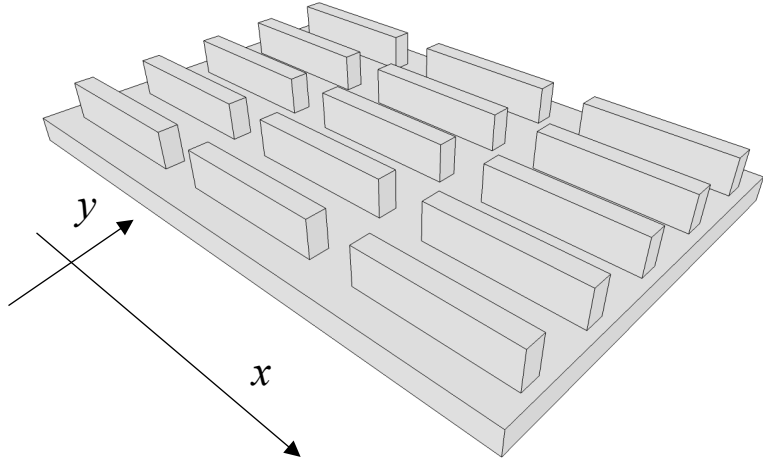


Figure 40: Representation of a non-isotropic pattern, in the picture, are shown the y-direction and x-direction.

This phenomenon is caused by the pitch distance difference and elements' length along the different axes. We suppose that observing the drop along one direction the contact angle value would be governed by the area fraction calculated along that direction, and not by the overall area fraction.

Supposing that L_x and L_y are the dimensions of the elements in x-direction and y-direction, and P_x and P_y the corresponding pitch distances, the solid-liquid area fraction of the surface is calculated as:

$$\varphi_{tot} = \frac{L_x L_y}{P_x P_y} \quad (44)$$

While on the x-direction we would calculate the fictitious solid-liquid area fraction as:

$$\varphi_x = \frac{L_x^2}{P_x^2} \quad (45)$$

And on y-direction we would calculate the fictitious solid-liquid area fraction as:

$$\varphi_y = \frac{L_y^2}{D P_y^2} \quad (46)$$

In our survey, we used three different surfaces Sh, R1, and R2. The first one has structures dimensions of 200 by 40 μm , while R1 and R2 have structures of 1.6 by 0.4 μm and different pitch distances. Table 10 shows the solid-liquid area fraction along with the corresponding Cassie-Baxter prediction, and the experimental values of contact angles measured in the two directions.

φ_{tot}	φ_x	φ_y	CA_{tot}	CA_x	CA_y	CA_{mx}	CA_{my}
-----------------	-------------	-------------	------------	--------	--------	-----------	-----------

S	0,4	0,8	0,2	133,	115,	145,	141.0±1	143,7±1
h	5	1	5	0	3	4	.2	.1
R	0,1	0,2	0,0	158,	145,	166,	157.6±1	160,9±1
1	0	5	4	3	4	3	.4	.3
R	0,0	0,1	0,0	163,	152,	170,	160.1±1	165.3±1
2	6	6	2	7	5	3	.2	.6

Table 10: In the table are shown the area solid-liquid solid fraction ϕ for each surface. The total area fraction represents the area fraction of the surface, while the x and y area fractions represent the area fraction as if the surface would be homogenous in the two directions with the geometrical parameter of the x or y -direction. The contact angle $CA_{tot,x,y}$ represent the Cassie-Baxter predictions to respect the different area fraction values. CA_{mx} and CA_{my} are the experimental values of CA of a 3 μ l drop deposited on the surface observed along the direction x and the direction y .

It can be observed that the measured contact angle are a weighted average of the prediction contact angles on the two direction, this can be explained taking into account the triple line tension [147], [148], that tends to maintain round the profile of small drops and fight against the contact angle hysteresis on the two directions.

4.7 Conclusion

Within our work a set of superhydrophobic and low drag surfaces was fabricated. In order to determine a correlation existing between these two properties, a series of experiments targeting both of them were performed. Beside the classical tests we measured the acceleration of a drop sliding on tilted plane at different angles.

According to previous theory, we identify two main energy dissipation mechanisms: pinning/ depinning of the triple line and viscous losses inside the sliding drop. Starting from this assumption we developed a model for discriminating between the different forms of energy dissipations.

This model shows good agreement with the experimental data. Furthermore, from the experimental results, a multifunctional coefficient (c_{mf}) was proposed for evaluating the overall superhydrophobic properties of a surface, including drag reduction. In our case hierarchical surfaces, that show superhydrophobicity and low drag properties, have lower c_{mf} values with respect to the other surfaces. Hierarchical surfaces H1 and H2 ($c_{ms}^{H1} = 0.33$ and $c_{ms}^{H2} = 0.24$) showed significant improvement over single level surfaces L1 and L2 ($c_{ms}^{L1} = 0.67$

and $c_{ms}^{L2} = 0.62$) - hierarchical surfaces show similar hydrophobic properties but have much better drag reduction. Similarly, compared to Sh ($c_{ms}^{Sh} = 1.51$), the hierarchical surfaces are more hydrophobic showing also improvement in drag reduction.

5 Homogeneous hydrophobic/hydrophilic surfaces for water harvesting

5.1 Abstract

sharkskin in and lotus leaf is here discussed. Similarly, we combine the typical heterogeneous chemical properties of the surface of the darkling beetle with the typical riblets structures of sharkskin. The assessment of static and dynamic wettability properties of such structures allows for an indirect measurement of their energy harvesting potential. Results seem to indicate that chemically heterogeneous surfaces, such as the hierarchical surfaces inspired by the sharkskin and lotus leaf, are particularly suitable for harvesting water.

5.2 Introduction

Several plants leaves and animals' skin have interesting properties such as superhydrophobicity, low adhesion, and water collecting properties [1], [2]. These properties arise from the combination of hierarchical micro-pattern and chemical properties of the substrate. A well-known example of a natural superhydrophobic surface is the lotus leaf with its self-cleaning and low adhesion properties [80], [110]. Instead, the darkling beetle uses the combination of superhydrophobic/hydrophilic properties to

harvest water in the Namib Desert [88], [149]. The hydrophilic bumps of its hardened forewings condense air humidity, and the water is then conveyed through superhydrophobic micro-size grooves directly into the beetle mouth.

Two kinds of surfaces have been realized. The first one is made of silicon oxide covered by a self-assembly monolayer of 1-1-2-2-perfluorodecyltrichlorosilane, PF3 [96]. The second surface is composed of pillars of silicon dioxide covered with PF3 only on the lateral side, and not on the top: as a consequence, the top part of the pillar is hydrophilic while the lateral side is hydrophobic. This particular setup stresses the concept of a chemically heterogeneous surface used by the Namib Desert beetle. In fact, instead of the hydrophobic substrate, we introduce the gap between two pillars, where the air has 180° of contact angle.

Firstly, in order to maximise hydrophobic properties of the surfaces we have designed single level structures to fit the Cassie-Baxter equation [1] being in a stable condition [22], while we have used an extension of the equation to support the design of hierarchical surface [2]:

$$\cos \vartheta_{CB} = \varphi^N (\cos \vartheta_0 + 1) - 1 \quad (47)$$

The equation is an implement of the Cassie-Baxter equation that predicts an increase in the wettability properties of the surface in relation to the number of hierarchical levels (N).

Secondly, the friction between the liquid drop and the superhydrophobic surfaces has been investigated basing on several tests on a superhydrophobic inclined plate. This second study aims to discover a correlation between the substrate hydrophobicity (contact angle and contact angles hysteresis) and the resistance of the liquid, moving on the solid interface. By knowing the contact angle and the volume of the drop, it is possible to find the apparent contact area that can be used to compute the resistance factors of the moving drop. The results show that two main factors reduce the speed of a water drop moving over a superhydrophobic surface: the contact angle hysteresis and the internal energy loss of the viscous flow inside the drop. This second factor depends both on the surface inclination and on the pattern of the superhydrophobic surface. This analysis has been validated using an energy approach in which the nonconservative energy (calculated as the difference between final total energy and initial total energy) corresponds with the sum of the two energies described before.

These analyses have been used as a basis for the third series of experiments of water harvesting. The ability of a surface to harvest water can be maximised by combining a hydrophilic surface, where the humidity nucleates and becomes water droplet, with low contact angle hysteresis, so that the drop can easily slide-off. These two concepts, usually opposite, are merged into the same surface thanks to the presence of a specific micropattern and a chemistry heterogeneous over the surface.

5.3 Materials and methods

The fabrication of surfaces has been carried out in a clean-room, class 100, 6'' wafer CMOS pilot line. All surfaces have been realized on silicon substrate, where the geometrical parameters are defined by soft-lithography and dry etching. The standard etching procedure has been adopted to obtain the one level structures, while a more complex procedure has been used to create the hierarchical surfaces. For the hierarchical surfaces, two lithography steps and several etching steps, both wet and dry have been used. The details of the process are described in the section dedicated to the microfabrication processes, paragraph 2.4.2. Through these processes, five single level surfaces and six hierarchical surfaces have been realized in which the hierarchical surfaces are the combination of one-level structures, where bigger pillars or riblets (first hierarchical level)

are used as the base for smaller pillars (second hierarchical level). Geometries and composition of one-level and hierarchical surfaces are described in Table 11 and Table 12.

	<i>Diameter - Lateral size (μm)</i>	<i>Pitch distance (μm)</i>
<i>L1</i>	1	3
<i>L2</i>	1.6x0.4	3.2x2
<i>L3</i>	5	10
<i>L4</i>	8	12
<i>S1</i>	180x40	200x80

Table 11: Geometrical characteristics of single level structures.

	<i>First level structures</i>	<i>Second Level structures</i>
<i>LH1</i>	L3	L1
<i>LH2</i>	L3	L2
<i>Lh3</i>	L4	L1
<i>LH4</i>	L4	L2
<i>Sh1</i>	S1	L1
<i>Sh2</i>	S1	L2

Table 12: Combination of structures used to realize hierarchical structures. Each hierarchical surface is identified by an acronym

(first column), and is composed of first hierarchical level (column 2) and second hierarchical level (column 3) structures.

The height of the pillars has been calculated to maintain the stability of the Cassie-Baxter state on the pillar-like structures and to maximize the water sliding in riblets inspired by sharkskin. Figure 41 reports SEM images of hierarchical structures composed of lotus leaf inspired structures, the base structures in these images are L3 and L4, while the second hierarchical level is composed of L1 (round pillars) and L2 (rectangular pillars).

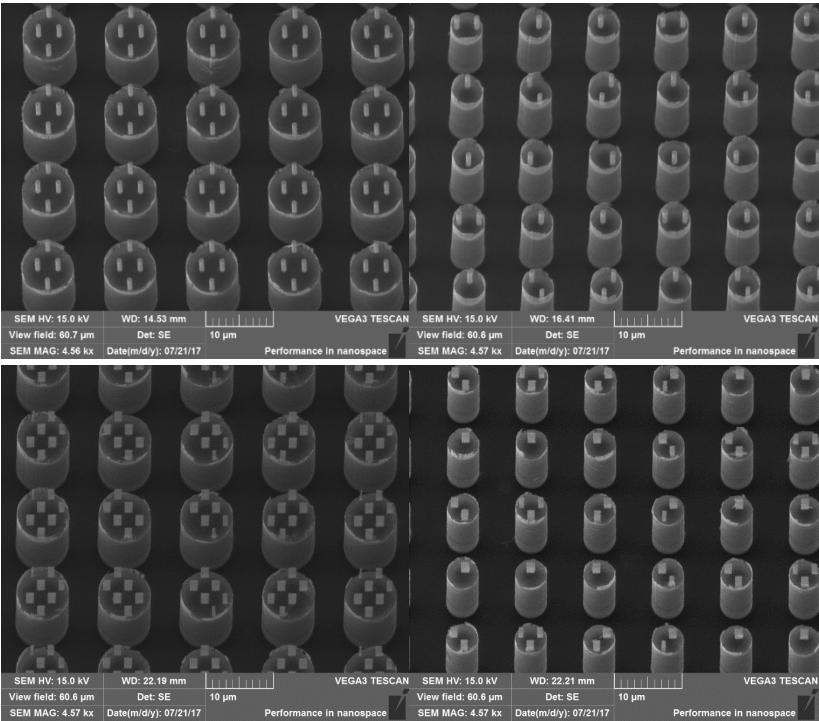


Figure 41: SEM images that represent the hierarchical surface realized for this study. The top images show the hierarchical structures with second hierarchical level composed of round pillars, while the bottom images show the hierarchical structures with second hierarchical level composed of rectangular pillars.

Surface chemistry of samples has been tuned in order to obtain an intrinsically hydrophobic, hydrophilic or heterogeneous substrate. The silicon substrate is composed of native dioxide (SiO_2), which makes the surface naturally hydrophilic. Furthermore, an oxygen plasma has been used as the last step during the fabrication process to clean the surface from all residual contaminants. This oxygen plasma guarantees the uniformity of the silicon dioxide thickness, 2-3 nm. To make the substrate hydrophobic, the silicon substrate has to be coated with a self-assembly monolayer of 1-1-2-2-perfluorodecyltrichlorosilane (PF3). After the coating with this hydrophobic silane, the contact angle on flat silicon surfaces has been measured to be 106.8° . For the fabrication of surfaces with heterogeneous chemistry, a hydrophilic spot on top of the pillars and hydrophobic properties on the side and bottom of the pillars have been created. The process consists in the realization of the pillars without stripping the residual resist on top of the pillars with oxygen plasma after the last etching step. The surface is then coated with PF3, cleaned with deionized water, with IPA-acetone-IPA. This allows the silane to settle on the side and bottom of the pillars, without touching the top of the pillars. Afterwards, the redundancy of silane is removed with water and IPA and the residual is stripped with acetone, and then cleaned with IPA. This cleaning process is performed in an ultrasound cleaner to guarantee its success. This step required a

modification of the lithography process, without using the hydrophobic primer before the resist deposition. This step is needed to avoid the hydrophobic primer to stay on the top of the pillars, which would vanish the whole procedure. The primer is fundamental to enhance the adhesion of the photoresist to the substrate, in particular when the diameter of the pillars is below 2 μm . To solve this technological problem, a dip in buffered oxide etch (BOE) of the silicon wafer has been performed just before the resist coating. This removes the small native oxide and temporarily hydrolyzes the silicon surface, making it hydrophobic for time needed to coat the substrate with resist.

The surfaces have been analysed using deionized water. The static contact angle of each surface has been tested on a goniometer with the sessile drop method. A small drop of water was settled with a Hamilton syringe which guarantees the repeatability of the drop volume, 3 μl . A dedicated plug-in of the software ImageJ has been used to evaluate the drop contact angle [114]. After the deposition of the water on the surfaces, vibration is used in order to allow the contact angle to relax and reach a value close to the static contact angle. The advancing and receding contact angle has been evaluated by using the dynamic sessile drop method as mentioned before. The method uses a

syringe vertically suspended over the surfaces to depose a drop on the surface so that the syringe needle remains in touch with the upper part of the drop. At this point, the drop has changed in volume by moving the syringe plunger. The maximum angle that the drop reaches before increasing its contact area is defined as the advancing angle while the minimum angle that the drop reaches before reducing its contact area is defined as the receding angle. The whole procedure is recorded by the camera of the goniometer and then analysed with the plug-in of ImageJ. Another dynamic test is performed on the surfaces where a drop is automatically settled on the inclined surface. Its acceleration is extrapolated from the detection of the passage of the drop in front of the gates composed of coupled photodiode-LED. The signal is analysed by a microcontroller and elaborated by the computer. The details of the procedure are described in Chapter 4, paragraph 3. To evaluate the ability to collect water over a surface, a direct test has been performed. The surfaces were placed on a rotating plate, faced by a commercial humidifier. The rotating plate was surrounded by a wall to maintain humidity over the plate. The plate rotates at a constant speed of 18 rad/s and the distance between the surfaces and the humidifier has been kept steady as well. The experiment lasted for six consecutive hours to reach the effect of rotation.

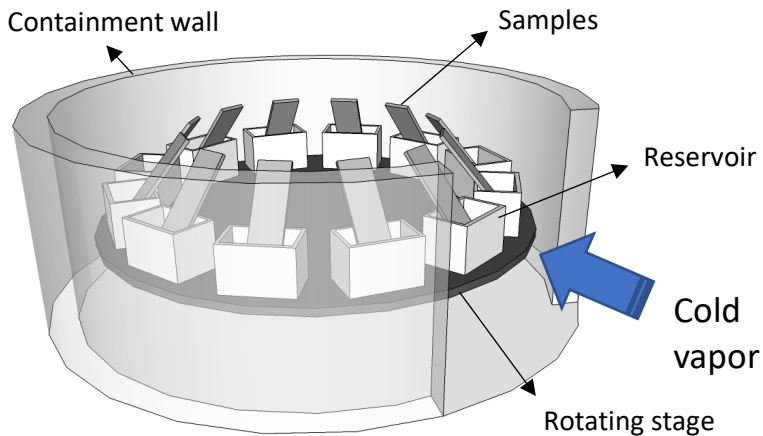


Figure 42: Experimental setup used to realize the water harvesting test.

The reservoirs have been weighted with a 3-digit precision scale before and after the test without the silicon sample because only the actual harvested water is to be taken into account in the experiment. Furthermore, an empty reservoir has been placed in the rotating plate and the amount of water collected by it has been subtracted from the volume of the harvested water since it has been harvested in by the reservoir itself and not by the surface.

5.4 Results

In this section, we propose the data collected during the characterization of our surfaces. We measured the static contact angle with a goniometer and the advancing and receding contact angles have been analyzed by filming the drop while water was pumped in and out it with the method called the dynamic sessile drop method. Furthermore, we analyzed the dynamics of the drop sliding down the inclined plane at different angles. This method had the advantage of adding a dynamic analysis of the surface and, in particular, provides relevant data used to predict the harvesting properties of each surface. A final analysis has been carried out to directly evaluate the ability of the surface of harvesting water.

5.4.1 Contact angle

The values of contact angles have been evaluating through the sessile drop method and are reported in Figure 43 along with the prediction of contact angle based on the Cassie-Baxter equation. Each surface is characterized by a two-digit code that identifies the geometrical parameters of the surface, plus a third digit that identifies the chemistry of the surface. “F” means that the surfaces are intrinsically hydrophobic, while “/” means that the chemistry of the surface is not homogenous. A slightly different inscription has been used in the case with hierarchical surfaces: the first digit indicates the geometry of the base structures while

the second digit indicates hierarchical surfaces and the third digit refers to the geometry of the second hierarchical level. No indication of surface chemistry has been given on this surface since only hydrophobic substrate has been used. All analysed surfaces have a composite air-solid interface under the drop and follow the Cassie-Baxter equation.

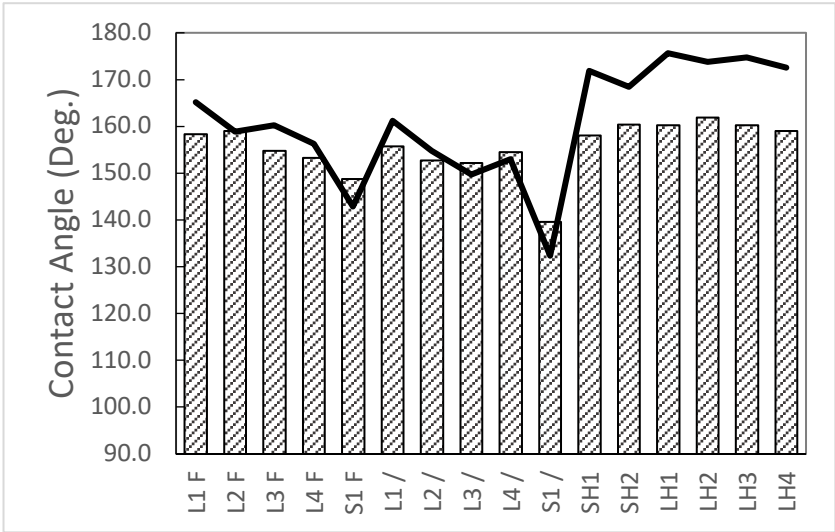


Figure 43: The graph reports contact angle values for different surfaces. The surfaces are geometrically defined by a two-digit code if they are composed of a single level of structures and if they are composed of hierarchical structures, they are defined by

three digits. An additional digit indicates the chemistry of the surface: “F” if the substrate is hydrophobic or “/” if the substrate is chemically heterogeneous. The black line indicates the Cassie-Baxter prediction of each surface.

It is evident that the chemistry of the surface is essential as the geometrical parameters in order to obtain superhydrophobic surfaces. In fact, surfaces with different chemistry and identical geometrical parameters show a considerable variation in terms of contact angle value. This difference becomes significant once the hysteresis is taken into account.

5.4.2 Contact angle hysteresis

The hysteresis of contact angle has been computed as the differences between the cosine of receding angle and cosine of advancing angle. On this basis, the values which have been calculated are directly linked with the intrinsic resistance of the surface to the drop movement [12]. As stated before, changing the chemistry of the top part of the pillars modifies the wettability of the surface. As a matter of fact, the surfaces that have an homogenous-hydrophobic chemistry offer lower resistance to water displacement (lower hysteresis) compared with some geometrically identical surfaces with heterogeneous chemistry.

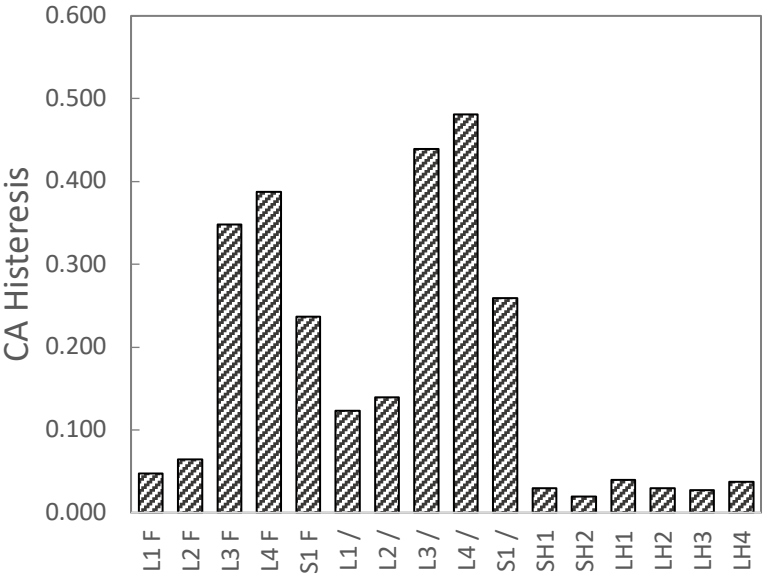


Figure 44: The graph reports values of contact angle hysteresis for different surfaces. The hysteresis is computed as the difference of the cosine of the receding and the cosine of the advancing angle. The surfaces are geometrically defined by a two-digit code if composed of a single level of structures and by three digits if composed of hierarchical structures. An additional digit indicates the chemistry of the surface: “F” if the substrate is hydrophobic, “/” if the substrate is chemically heterogeneous.

In particular, surfaces composed of hierarchical structures have low hysteresis. In hierarchical structures the wettability properties are enhanced compared to the ones of single-level structures. Furthermore, in nature the superhydrophobic natural surfaces have similar hierarchical structures than the ones we have produced. .

5.4.3 Dynamics of moving drops

In this section, the data collected from a drop sliding down the superhydrophobic inclined surfaces are collected to compute the energy lost by the drop itself during the sliding process. In the classical case a solid sphere rolls down an inclined plane; conversely, in this case the drop mainly slides. Furthermore, the energy lost by the drop cannot be only linked with the interaction between the drop triple line and the surface, but also with the energy lost by internal viscous forces of the liquid composing the drop (water). In our dissertation, the non-conservative energy, equation (48), has been modeled as the sum of a pinning-depinning energy loss, equation (49), and an internal flow energy loss, equation (50).

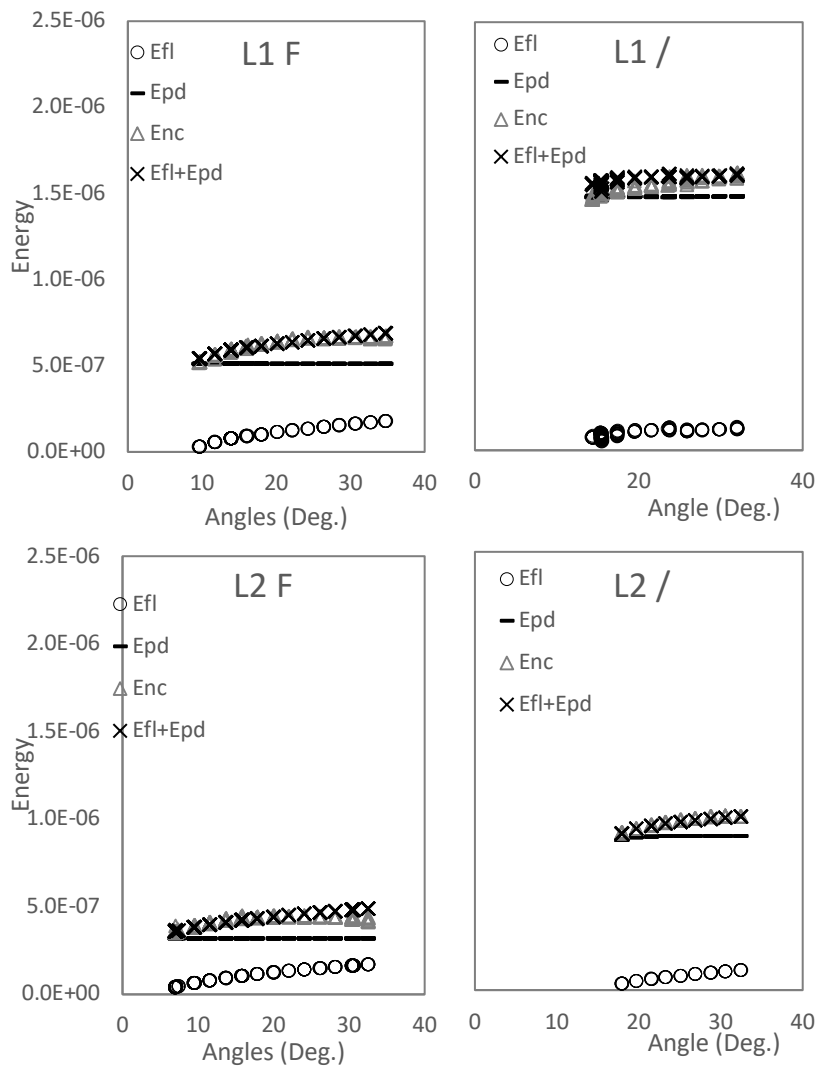
$$E_{NC} = \frac{1}{2}mv_f^2 - \frac{1}{2}mv_i^2 - mgl\sin\alpha \quad (48)$$

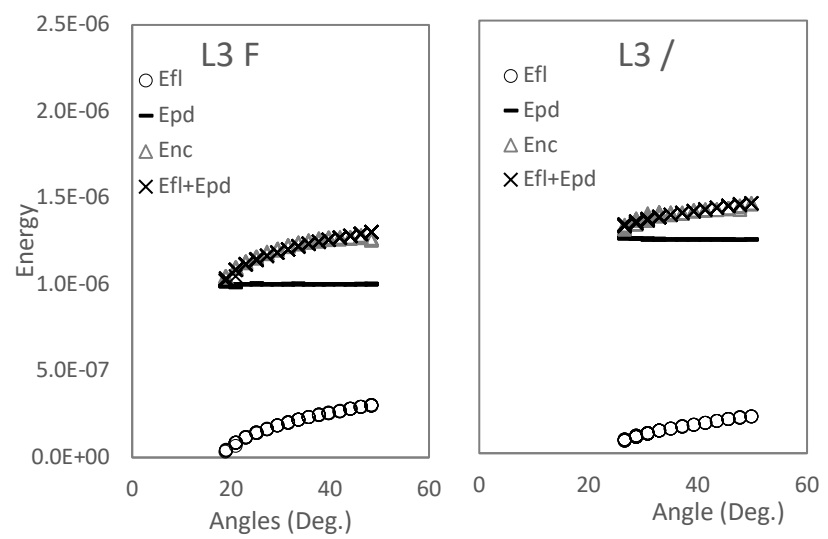
$$E_{pd} = \gamma(\cos\theta_r^{app} + 1)w\frac{a}{2}(t_f^2 - t_i^2) \quad (49)$$

$$E_{fl} = \frac{\mu A_c}{h} a^2 (t_f^3 - t_i^3) \quad (50)$$

The pinning-depinning energy loss depends on the radius of the contact region and on the receding angle, while the internal energy loss depends on the contact area between the drop and the surface, the liquid properties, and the lengths of interaction in which the viscous forces act. In Figure 45 and Figure 46 the energy consumed by a sliding drop for each surface is reported in the graphs.

Homogeneous hydrophobic/hydrophilic surfaces for water harvesting





Homogeneous hydrophobic/hydrophilic surfaces for water harvesting

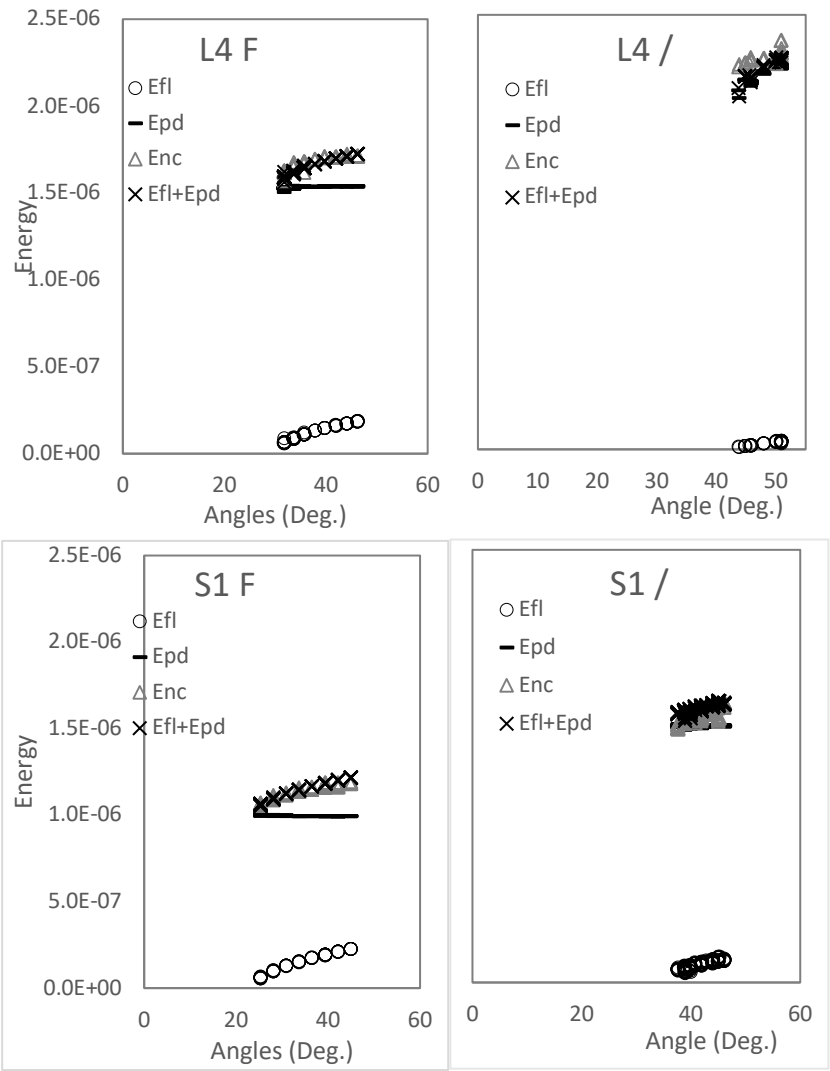
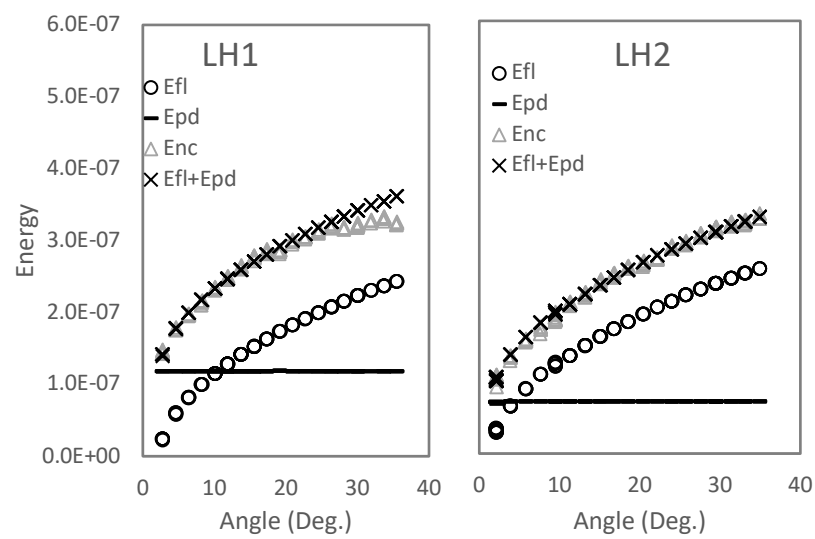


Figure 45: Graphs of energy consumed by a sliding drop over an inclined surface. On the left part, the graphs indicate the energy consumed over intrinsically hydrophobic surfaces, while on the right there are the corresponding surfaces: which have the same geometry but with heterogeneous chemistry.

In the graphs of Figure 45, thanks to a comparison between the surfaces with the intrinsically hydrophobic substrate and intrinsically hydrophilic/hydrophobic substrate it can be argued that the left-handside graphs (surfaces with intrinsically hydrophobic chemistry) report lower energy consumption compared with the right-handside (surfaces with heterogeneous chemistry). This difference is due to the hydrophilic spot on the top of each pillar. The moving drop is attracted with greater strength on the surface, and the pinning-depinning mechanism is stronger, demanding more energy to detach the drop from a spot and move it to another spot. On average five times less energy is required to move a drop on a superhydrophobic surface with hierarchical structures, Figure 46. The energy graphs of surfaces with hierarchical pillars show that for such surfaces the energy consumption is no longer led by the pinning-depinning mechanism. In fact, the losses of energy due to the viscous flow inside the drop are even at a small angle

comparable or even greater than the ones consumed by the pinning-depinning mechanism. Such a phenomenon did not happen on surfaces composed of a single-level structures, where the energy consumption was almost entirely due to the pinning-depinning mechanism.



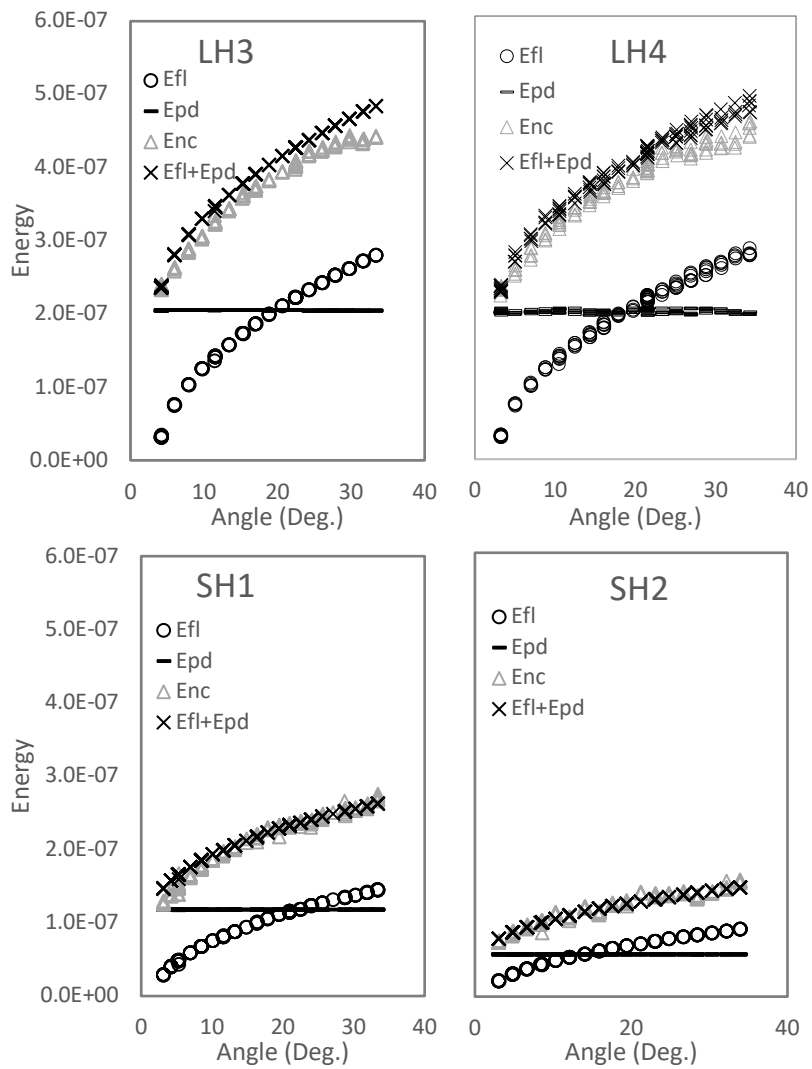


Figure 46: Energy consumption on hierarchical superhydrophobic surfaces.

5.4.4 Harvesting

The present section is dedicated to the data on water harvesting. The data proposed here have been collected using the procedure described in the methodology section, and are presented in centimetre cube. The six-hour experiment has been performed using a commercial humidifier. In total twenty-eight surfaces have been analyzed and one of them is a flat hydrophilic surface that has been used as a reference. Furthermore, an empty cup has been placed on the rotating stage to eliminate all possible external influences. The amount of water that has been collected during the experiment in the empty cup has been subtracted from the amount of water collected by each surface. In Figure 47 the results of the harvesting experiment for all the surfaces are showed. The geometry of the surface is defined by two-digit with regard to one level surfaces and by three-digits with regard to hierarchical surfaces. The digit following the name indicates the surface chemistry: “F” for hydrophobic, “P” for hydrophilic, and “/” for heterogeneous chemistry. From this graph, it is evident that L1/, SH1 F, and SH2 F are the best

surfaces for water harvesting. Apart from this piece of information, it seems hard to identify a precise trend in the data.

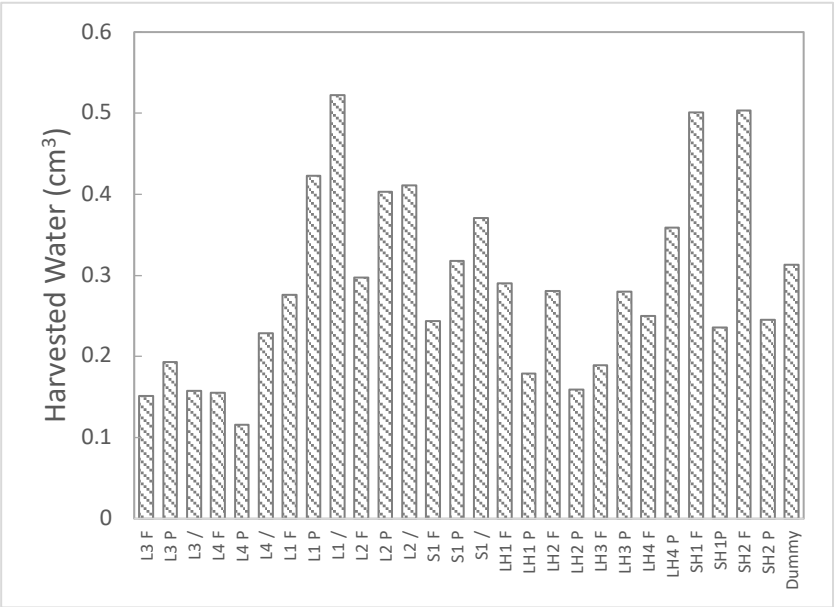


Figure 47: Sum of data about the ability of harvesting water of different surfaces. The bars indicate the volume of water that each surface managed to harvest in six hours in humid ambient.

In Figure 48, only the surfaces with one-level structure have been analyzed. A different scale colour has been used for the bars depending on the chemistry of the surface. Thanks to this graph, it is possible to see a first important feature that is the

surfaces with heterogeneous chemistry generally perform better than surfaces with homogenous chemistry (hydrophobic or hydrophilic). Furthermore, superhydrophilic surfaces are more advisable than superhydrophobic surfaces at harvesting water. Moreover, this result is in compliance with the theory and in reality there are several pieces of evidence, such as superhydrophobic surfaces proposed as anti-fogging devices [150]–[154].

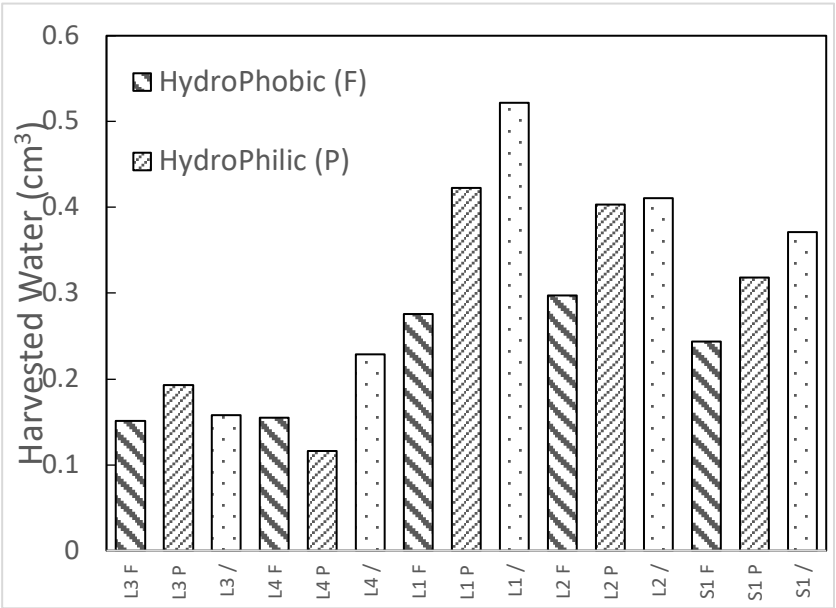


Figure 48: The graph shows the volume of water harvested by different surfaces. The main comparison is between hydrophobic, hydrophilic, and heterogeneous surfaces.

5.5 Conclusion

In this chapter, we realized a wide series of surfaces that have been tested with the goal of maximizing the water harvesting properties. For this reason, superhydrophobic hierarchical surfaces have been created, by taking inspiration from lotus leaf, sharkskin riblets surfaces, and surfaces with heterogeneous chemistry typical of the darkling beetle. Furthermore,

hierarchical surfaces combining sharkskin with lotus leaf have been realized as surfaces with heterogeneous chemistry and structures of the sharkskin structures. On these surfaces, several systematic tests have been performed and have produced a coefficient c_H , which indicates the ability of a surface of harvesting water. This coefficient has been positively compared with actual data of water harvesting on the surfaces. We finally showed how the heterogeneous chemistry is able to improve the water collecting performance of all surfaces with one single level structures, while hierarchical structures generally do not improve the ability of water harvesting. The only exception is the surface combining sharkskin and lotus leaf inspired structures.

6 From Hydrophilic to Superhydrophobic

6.1 Abstract

In this chapter silicon-based bioinspired, superhydrophobic surfaces are proposed. The fabrication of these surfaces has taken inspiration from butterfly wings. Furthermore, such surfaces are compared with lotus leaf-inspired, hierarchical and non-hierarchical surfaces. Butterfly wings inspired surfaces are composed of re-entrant structure. This peculiarity allows the surfaces to reach a stable superhydrophobic state even though the substrate is hydrophilic. In the following chapter, we coated the surfaces with a self-assembly monolayer which gives a contact angle value of 78° . Thanks to this contact angle value it is possible to observe metastable superhydrophobicity on all our samples. On this basis, we demonstrate that the butterfly-inspired surfaces are the only surfaces which can hold this metastable state thanks to their re-entrant surfaces. In fact, the re-entrance of the structures composing the butterfly wings surfaces acts as energy barriers to the surface liquid penetration. At last, a wear analysis of the butterfly-inspired surfaces has been carried out to observe the change of water repellence with wear.

6.2 Introduction

Butterfly wings are known in literature for their optical properties [155], [156], and, recently, for their wettability properties as well, such as super-hydrophobicity, low drag [122] and anti-fouling [157]. Interesting wettability properties in

several leaves of plants [104] and insects [2] have already been studied in numerous papers [1], [117], [158].

Since flat surfaces cannot reach contact angle (CA) greater than 125-130° [159], super-hydrophobicity can be obtained only from precise texturing of the surfaces. Wenzel equation can predict an increase in the contact angle on a surface by intensifying the area under the drop which generates an impalement of liquid on the structures. Wenzel equation predicts the increase in CA only due to geometrical parameters, equation (51) [19], [160].

$$\cos\vartheta_w = r_w \cos\vartheta_e \quad (51)$$

Where ϑ_w is the apparent contact angle predicted by Wenzel equation, r_w is the surface roughness and ϑ_e is the thermodynamic contact angle. Even though Wenzel state may lead to high contact angle measurement, it cannot lead to superhydrophobicity. Due to the impalement, the droplet cannot easily pour the surface. In fact, superhydrophobicity can be obtained only from the combination of high contact angle, generally higher than 150°, with low tilting angle, lower than 10° [124].

The only way to obtain superhydrophobicity is to reach the Cassie-Baxter state. Cassie-Baxter equation predicts that, under

certain conditions, the drop reaches a fakir state on the asperities of the surfaces. High contact angle is obtained because the droplet lies on a composite interface [21]. Equation (52) shows the relation, extrapolated by Cassie-Baxter, between base contact angle, surface area fraction and apparent contact angle.

$$\cos\vartheta_{CB} = f(\cos\vartheta_e + 1) - 1 \quad (52)$$

Both equations (51) and (52) lack of information about the stability of one state compared with the other. Under which circumstances does a certain pattern lead to Wenzel rather than Cassie-Baxter state? Several researchers tackle this problem from different points of view, [22], [45], [108], [161]–[164]. e.i. The robustness of the Cassie-Baxter state has been experimentally tested by applying vibrations at the structures [164]. Moreover, another controversial point can occur in the case of superhydrophobicity, which can arise from hydrophilic substrate. The claim that has been submitted in [165] is questionable, in which the author argued that superhydrophobicity on lotus leaf can arise from a hydrophilic substrate. Such a claim has caused some scepticism [166]. The key to generate superhydrophobic surfaces from intrinsic hydrophilic substrate is the employment of re-entrant structures [167], [168] such as the one found in butterfly wings rather than in lotus leaf.

The aim of our work is to combine hierarchical re-entrant structures to reach metastable, robust Cassie-Baxter state even with an intrinsic hydrophilic substrate. A series of silicon-based structures have been generated for this purpose and coated with trimethylchlorosilane (TMCS). TMCS leads to a measured contact angle of 77.5° . The analyses carried out in this work include measurements of contact and tilt angle. Three different surfaces have been realized: flat-topped post, hierarchical [169] and butterfly-inspired structures which are composed of a regular array of pillar with diameter of $5\text{ }\mu\text{m}$. For each surface, four different pitch distances have been taken into account, from $10\text{ }\mu\text{m}$ to $25\text{ }\mu\text{m}$.

Finally, the last paragraph deals with the wear analysis of the butterfly-inspired structures. Furthermore, in this last section, the surfaces are characterized before and after wear. Some considerations on the desirable design for a possible application in the business field are then stated.

6.3 Experimental Processes

In this chapter, the clean-room experimental processes used to generate the surfaces have been reported such as the coating method and the methodology used in wettability analysis.

6.3.1 Surface Fabrication

Four different patterns have been generated: the first one is a reference pattern of flat-topped post structures, while the second and third are two lotus leaf inspired structures and the last one is the butterfly inspired pattern. All structures have been realized on silicon mono-crystalline, grain orientation $\langle 100 \rangle$. Lotus leaf inspired patterns [169] have been realized with a combination of soft lithography with dry plus wet processes. Instead, combination of soft lithography with dry Bosch and isotropic processes have been used to generate the butterfly inspired structures. The average depth of pillars is about 15 μm . All surfaces have a diameter of pillars of 5 μm and a pitch distance from 10 to 25 μm with four regular steps.

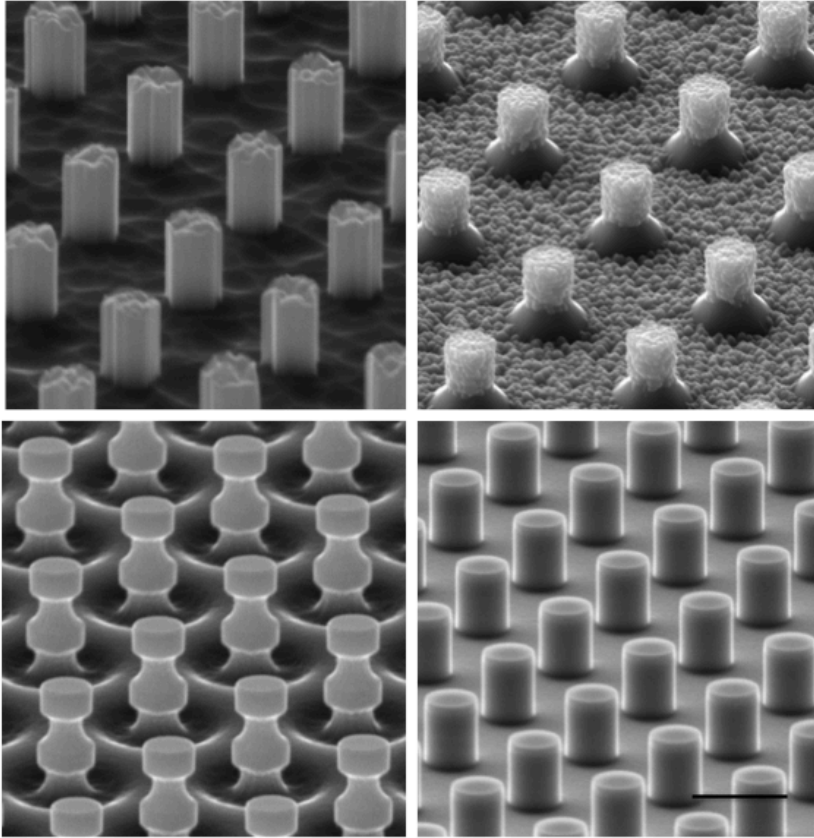


Figure 49: SEM images of the different structures analysed in the chapter. On the top, the surfaces inspired lotus leaf [26]. On the

bottom, butterfly-inspired structures and flat-tapered post structures.

Silicon surfaces have native oxide that shows a base CA lower than 30 °. For our purpose, the surface needs to be coated with a monolayer of trimethylchlorosilane (TMCS) that gives slightly hydrophilic properties to the highly hydrophilic substrate of silicon oxide. Contact angle measured on a lapped surface on coated silicon wafer ($R_a=0.3\text{nm}$) is equal to 77.5 °.

6.3.2 Wettability test

Contact angle analysis has been carried out with Hamilton syringe; the drop size is 3 μl and the liquid used is deionized water of resistance 18 M Ω . The software “drop analysis” is then used to detect the contact angle of the drop [114]. Sliding angle is measured by tilting manually the sample until the drop rolls off.

6.4 Theory prediction and analysis

In this section, the experimental data of contact angles measurement of flat-topped pillars have been compared with the Cassie-Baxter and Wenzel predictions. This comparison proves the experimental method used in the surfaces analysis. Furthermore, these data are used to understand if any composite interface exists under the liquid drop.

The graph in Figure 50a displays the comparison between experimental data and theoretical predictions. Wenzel curve increases increasing the pitch distance between the pillars, due to the hydrophilicity of the substrate. This means that increasing the roughness reduces the contact angle. Hence, if this contact angle is greater than the base contact angle (77.5°), a composite interface occurs.

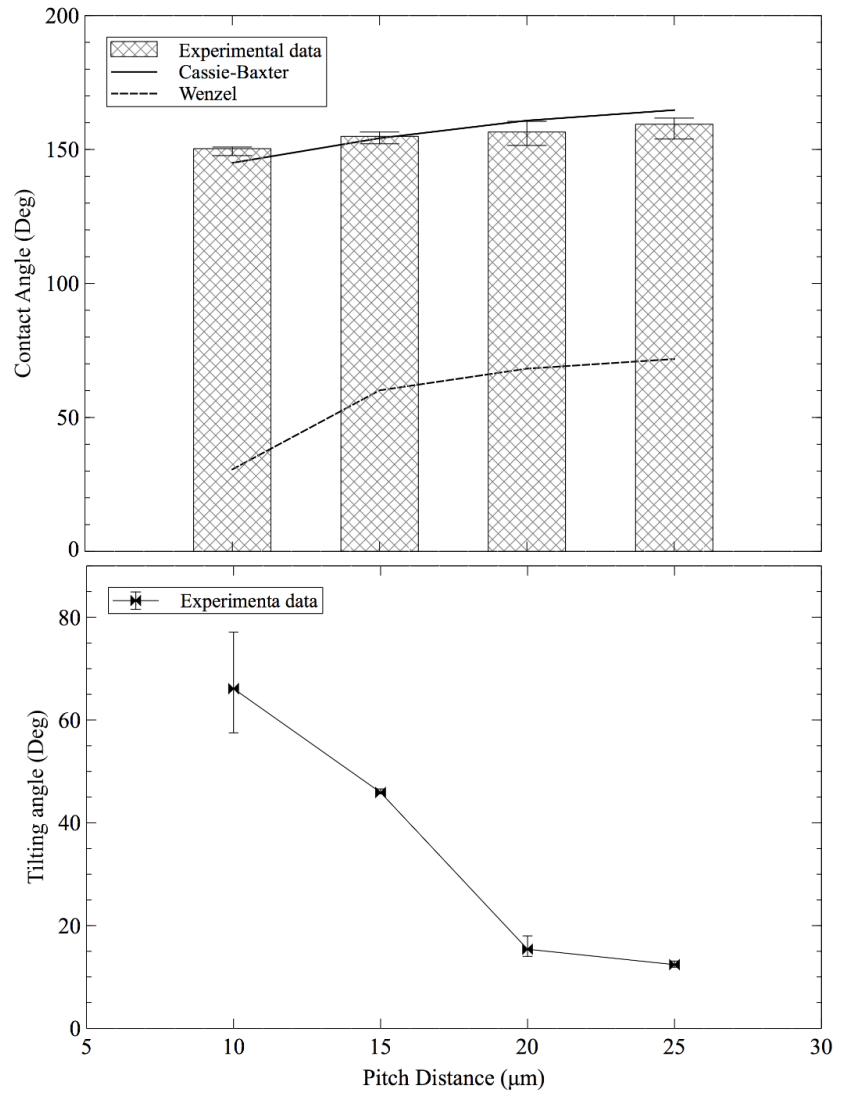


Figure 50: The upper graph shows the comparison between experimental contact angle data on flat-topped post structures with Cassie-Baxter and Wenzel prediction at different pitch distances. The lower graph shows tilt angle data for the flat-topped post structures at different pitch distance.

Experimental data are in compliance with the values of Cassie-Baxter prediction. Then a composite interface holds under the liquid drop. This hypothesis is also supported by the fact that the tilting angle decreases when the pitch distance between surfaces increases. On the other hand, for flat surfaces the drop is stuck to the surface no matter how the surface is placed. The fact that patterned surfaces have low TA means that they are not in an impaled state, such as Wenzel state.

6.5 Results

Butterfly-inspired, bumpy surfaces have already demonstrated in [167] to have metastable super-hydrophobic state with a hydrophilic substrate that holds thanks to the energy barriers. Following this lead, we have designed and generated micro-structured surfaces to have them experimentally tested along with other hierarchical structures [169] and reference flat-topped structures.

Since the hydrophilic substrate is slightly hydrophobic ($CA=77.5^\circ$), all surfaces analysed have a metastable, highly hydrophobic behaviour. However, only few of them manage to reach a super-hydrophobic behaviour for both contact and tilting angles.

The composite interface shows better results when the liquid-air area fraction is greater. In regular patterns, this occurs when the pitch distance between structures is as large as possible. In our particular case, surfaces with 25 μm of pitch distance prove better results. For this reason, in the following analysis we consider these surfaces.

Figure 51 sums up the wettability properties for each of the four analysed surfaces, by showing the contact and tilt angle analysis of surfaces composed of pillars with diameter of 5 μm and pitch distance of 25 μm . As in the paper [169], the two hierarchical structures have been named Wet+dry and Dry+wet, after their production methods.

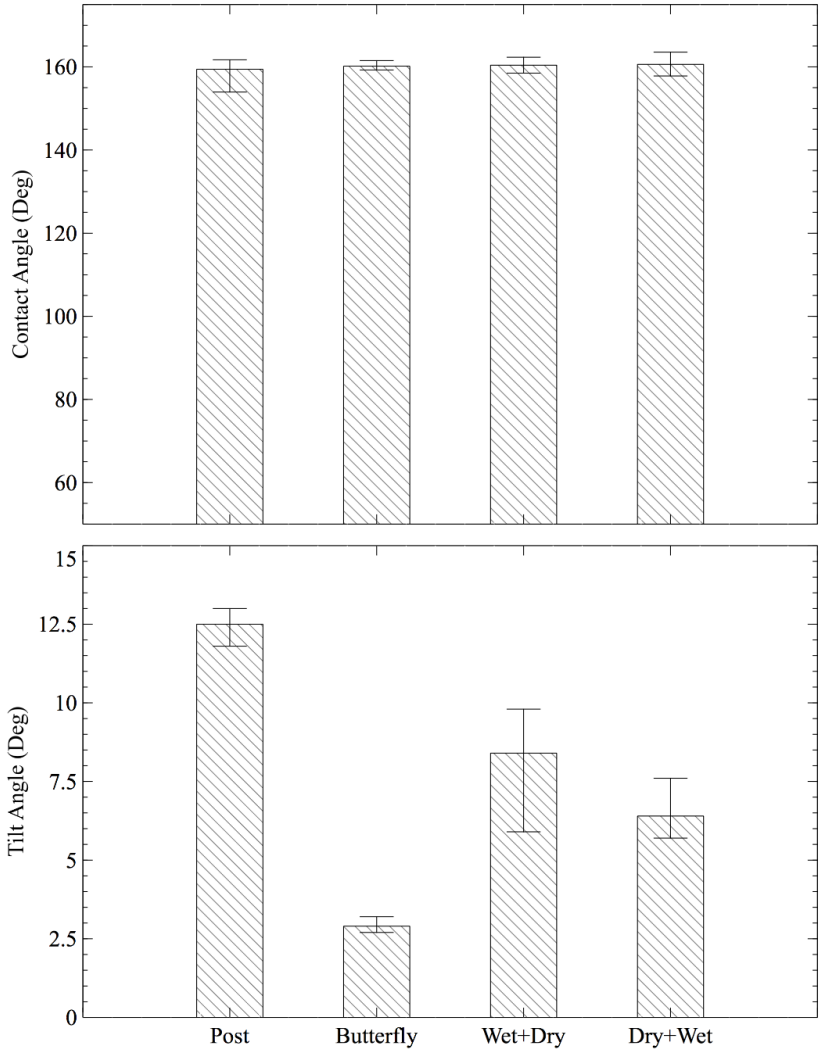


Figure 51: The two graphs show contact angle and tilt angle data for different surfaces. All surfaces have the pillar diameter of 5 μm and the pitch distance of 25 μm .

By analysing the graphs, it is evident that between the four surfaces no relevant difference between contact angles values can be found, especially considering errors bar. A greater difference can be seen in the tilt angle analysis. In fact, only hierarchical structures can hold super-hydrophobicity, since the flat-topped pillars have sliding angle greater than 10 °. Similar values can be reached by the textured hierarchical structures. Butterfly inspired surface is the only surface that reaches fairly low tilting angle of about 3 °.

6.6 Theoretical dissertation

In this section, the structures previously experimentally analysed have been tested with an analytical method based on pre-existing theory [164].

6.6.1 Flat-topped cylindrical pillars

Surfaces composed of flat-topped cylindrical pillars have been analysed in Afferrante & Carbone's paper [164]. They analytically demonstrated that these structures have not a stable composite interface for values of base contact angle lower than $\pi/2$. Flat structures of this chapter show temporary state of high contact

angle and fairly low tilting angle but, for the above reason, they cannot be considered as superhydrophobic stable surfaces.

6.6.2 Textured hierarchical pillars

Textured surfaces have been analysed in compliance with the equation for conical pillar that has been modified to fit pyramidal square-base pillars, as TMAH wet etching generates pyramidal square-based geometries.

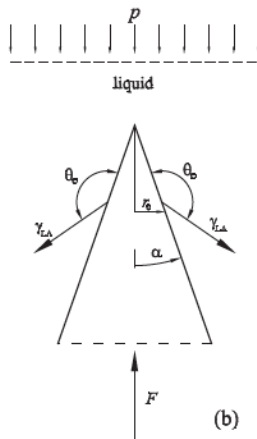


Figure 52: The forces acting on the conical pillar [21]. This image does not vary if we consider a conical pillar or a square base pyramidal.

The dimensionless liquid drop pressure, \hat{p} , for a square base pyramid can be written as it follows:

$$\hat{p} = -\frac{2\hat{r} \cos(\theta_e - \alpha)}{1 - \hat{r}^2} \quad (53)$$

Where \hat{r} is the dimensionless pillar radius, θ_e the thermodynamic contact angle and α is half of the opening angle of conical pillar.

This equation leads to the same conclusion for a conical pillar than [164]. In order to guarantee stability to the system, the dimensionless pressure has to increase as radius increases. Since it is not possible to ensure the inequality $0 < \alpha < \vartheta_e - \pi/2$, it is neither possible to have a stable composite interface with TMAH texturing. In fact, TMAH wet etching generates an intrinsic base angle of 54.74° that leads to an $\alpha=35.26^\circ$. The TMAH coating on silicon has base contact angle of 77.5° . By applying this last value at ϑ_e , the inequality $\alpha < \vartheta_e - \pi/2$ would require a negative α . Indeed, textured surface and for extension hierarchical structures, cannot have a stable composite interface.

1.1.1 Butterfly re-entrant inspired structures

In case of butterfly-inspired structures the liquid encounters at first the top of the pillars, which can be analysed as flat-topped pillars. Since the above part of the pillar follows the same rules

applied to flat-topped cylindrical pillars, these surfaces have not a stable composite interface.

For this reason, the equilibrium equation of the butterfly-inspired pillar takes into account at first the pinning point of the triple line, as shown in Figure 53.

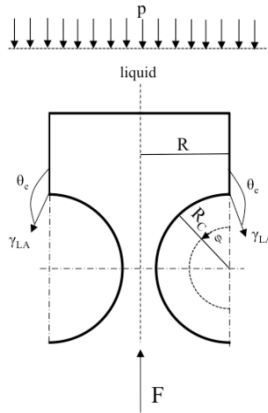


Figure 53: The forces acting on the upper part of the butterfly-inspired pillar.

Vertical equilibrium can be written as follows:

$$2\pi(R - R_c \sin\varphi) \sin(\varphi - \vartheta_e) \gamma_{LA} + F - \pi R^2 p + 2\pi p R_c \varphi \left(R - R_c \sin\left(\frac{\varphi}{2}\right) \right) \cos\left(\frac{\varphi}{2}\right) = 0 \quad (54)$$

Where γ_{LA} is the liquid-air surface tension, R is the pillar radius, R_c is internal curvature radius, φ is the angular coordinate of the liquid-pillar triple line corresponding to the impalement transition and p is the liquid drop pressure defined as the difference between the absolute drop pressure and the environmental pressure.

It is important to stress that the pressure of the liquid does not act only on the top-flat part of the pillar, but also on the circular lower part of the pillar. $2\pi p R_c \varphi \left(R - R_c \sin\left(\frac{\varphi}{2}\right) \right) \cos\left(\frac{\varphi}{2}\right)$ is the equation describing this last contribution.

$$\hat{p} = - \frac{\frac{\pi}{2} \sin(\varphi - \vartheta_e) (\hat{R} - \hat{R}_c \sin\varphi)}{1 - \frac{\pi}{2} \hat{R}_c \varphi \cos\left(\frac{\varphi}{2}\right) (R - R_c \sin\left(\frac{\varphi}{2}\right)) - \pi \left(\frac{\hat{R}}{2}\right)^2} \quad (55)$$

Where in the equation we used $F = pA$, $\hat{p} = p\lambda/\gamma_{LA}$, $\lambda = A^{\frac{1}{2}}/2$, $\hat{R} = R/\lambda$ and $\hat{R}_c = R_c/\lambda$.

Fixing the load, the stability condition requires that pressure intensifies as the angle φ grows/increases. This is true if $d\hat{p}/d\varphi > 0$, while $d\hat{p}/d\varphi \leq 0$ implies that the system is not stable by imposing $d\hat{p}/d\varphi = 0$, the results is

$$\begin{aligned}
 & -\pi \sin(\theta_e - \varphi) \left(\hat{R} - \hat{R}_c \sin(\varphi) \right) \left(\frac{1}{4} \pi \hat{R}^2 \varphi \cos^2 \frac{\varphi}{2} \right. \\
 & \quad + \frac{1}{4} \pi \hat{R} \varphi \sin \frac{\varphi}{2} \left(\hat{R} - \hat{R}_c \sin \frac{\varphi}{2} \right) \\
 & \quad \left. - \frac{1}{2} \pi \hat{R} \cos \frac{\varphi}{2} \left(\hat{R} - \hat{R}_c \sin \frac{\varphi}{2} \right) \right) = 0
 \end{aligned} \tag{56}$$

The important domain here is between 0 and π . In this gap the above equation is below zero when it is between $\frac{\pi}{3}$ and θ_e . This implies that two energy barriers occur at the complete wetting of the structures.

In the pinning point, there is a discontinuity. The equation of the impalement transition for the Wenzel state is the same than the previous one found on the pinning point:

$$\hat{p}_w = -\cos(\vartheta_e) \frac{\pi \hat{R}/2}{1 - \hat{R}^2 \pi/4} \tag{57}$$

The pressure that equation 7 predicts in our specific case is, in the worst scenario, 7.5 times greater than the pressure measured for a 3 μl water drop. When the liquid exceeds the pinning point it reaches the condition $\varphi = 0^+$, so the previous equation becomes as follows:

$$\hat{p} = \sin(\vartheta_e) \frac{\pi \hat{R}/2}{1 - \pi \left(\frac{\hat{R}}{2}\right)^2} \quad (58)$$

It is noteworthy to see that equation 8 predicts a pressure even higher than equation 7. Hence, we can assume that the re-entrances present on the structures generate an energy barrier that stabilizes the liquid in Cassie-Baxter state.

6.6.3 Experimental test

In order to experimentally test the theoretical results about the stability of the fakir state, we have performed an experiment to overcome the energy barrier and promote the transition from Cassie-Baxter to Wenzel state. The experiment consisted of attaching the surface on a vibrational plane and measuring the contact angle before and after vibration effects. The table 2 shows how the contact angles were affected.

	CA _B	CA _A
FLAT TOP PILLARS	164.3°	109.0°
WET+DRY	157.8°	126.0°
DRY+WET	159.15°	118.5°
BUTTERFLY INSPIRED	158.9°	148.5°

Table 13: Contact angle measurement before (CAB) and after (CAA) vibration effects.

Surfaces decrease the contact angle thanks to the introduction of vibration. Only the butterfly inspired structure did not pass a complete Wenzel state.

In fact, thanks to the equation (59) which combines Wenzel and Cassie-Baxter states, it [116] is possible to predict at which level the impalement the triple line stopped.

$$\cos\vartheta_{Mix} = \varphi(h)(R\cos\vartheta_0 + 1) - 1 \quad (59)$$

The first three structures have the almost complete wetting state and move from a superhydrophobic composite state to an impalement state. On the other hand, butterfly inspired structures have only a penetration of about 2 μm . This value can be found by solving the equation above. The value of 2 μm represents the height of the top part of the butterfly inspired structures. It is then possible to conclude that the theoretical dissertation has been here demonstrated with the experimental counterpart.

6.6.4 Butterfly inspired wear test

In order to test the wear resistance of surfaces a simple test has been performed. Butterfly-inspired surfaces have been rubbed with a cotton cloth. Although cotton fibres are expected to get stuck into the gap between pillars and tear them down or fibres

broke and stay stack into those gaps. These features cause a critical decrease in the wettability properties of the surface.

Figure 49 shows SEM and optic microscope enlargements of surfaces after rubbing. By rubbing the surfaces, several pillars broke at the weakest point that is located near the pillar base, for both position and diameter dimension. Contact motion has been applied only along one direction. Hence, pillars broke along lines parallel to the rubbing motion.

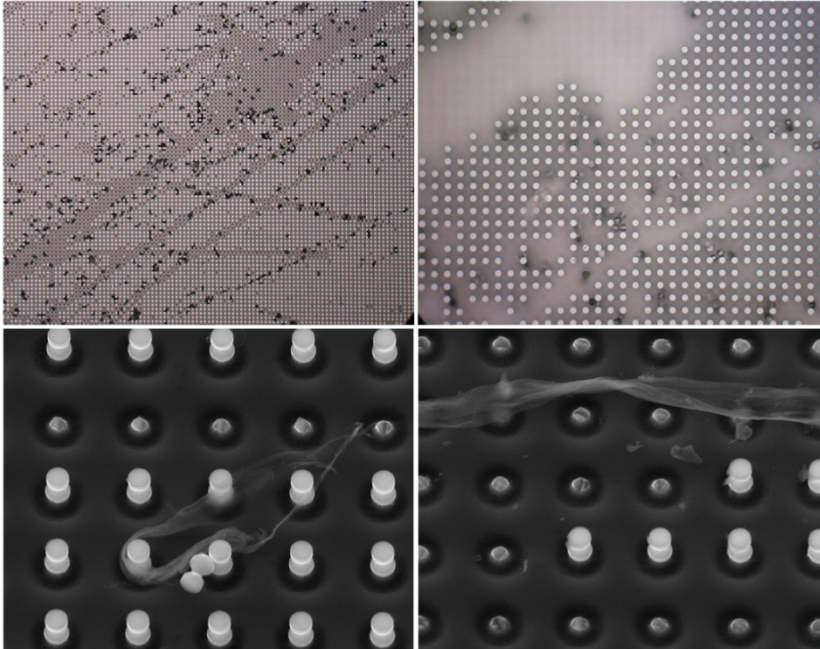


Figure 54: On the upper part: image of the damaged surface through wear (optic microscope). On the lower part: SEM images of fibre stuck in pillars and damaged surface.

As it has been stated at the beginning of the chapter, from Figure 54 it is clear that cotton cloth rubbing test has an impact on the surfaces at two different levels: by broking the pillars and by

letting the fibres stack into the pillar array generating a bridge for water to reach the base of the structure.

From these observations, it can be claimed that wettability properties of surfaces will be affected. Indeed, both contact and tilt angles of those surfaces have been reduced. Table 14 and Table 15 report the values of contact and tilting angles of the four different geometries which have been taken into account. The top diameter of the pillars has been fixed at 5 μm and the pitch distance varies from 10 to 25 μm in four regular steps according to the type of surface.

DIAMETER X PITCH DISTANCE	CA BEFORE WEAR	PERCENTAGE OF LOST IN CA	CA AFTER WEAR
5X10	148.5	-14%	127.8
5X15	155.3	-20.5%	123.5
5X20	158.6	-36.7%	100.4
5X25	160.1	-37.7%	87.2

Table 14: Contact angle values before and after wear analysis. The percentage of loss of performance is reported as well.

DIAMETER X PITCH DISTANCE	TA BEFORE WEAR	PERCENTAGE OF GAIN IN TA	TA AFTER WEAR
5X10	28.4	69.4%	48.1

5X15	18.9	250.7%	66.3
5X20	10.4	/	Sticky condition
5X25	2.9	/	Sticky condition

Table 15 Tilt angle values before and after wear analysis. The percentage of loss of performance is reported as well.

According to with Cassie-Baxter theory, the greater the pitch distance, the higher the contact angle. At the same time, the performance rapidly decreases with wear for both contact and tilt angles. In particular, it is remarkable that, for surfaces with a pitch distance of 20 and 25 μm , the tilt angle moves from a very low value to a sticky condition after wear.

Figure 55 reports the change of contact and tilt angles with wear.

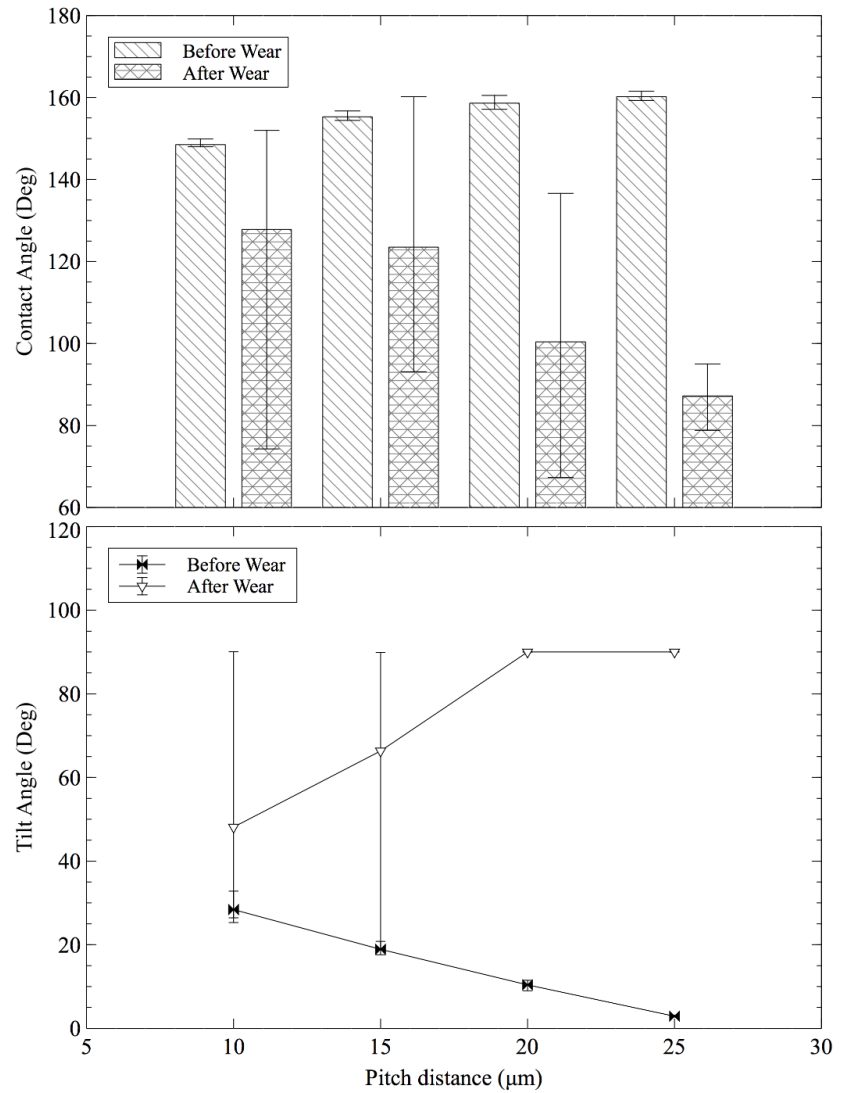


Figure 55: Graph shows the contact angle and the tilt angle of the butterfly-inspired structure before and after wear.

As previously stated, the butterfly inspired surface, with 25 μm of pitch distance, is considered the most desirable surface. Contact angle is over 160 degree and tilt angle is lower than 3 degrees. Although these values are quite interesting, they drop critically with wear. However, it is remarkable to consider the surfaces with a pitch distance of 10 μm , since, as demonstrated, they are the least easily influenced by wear. These latter have initially been discharged as being not super-hydrophobic.

Nevertheless, if we consider the analysis with a more commercial goal, surfaces with 10 μm pitch distance are becoming of great interest compared with the other three surfaces.

6.7 Mushrooms like re-entrant surfaces

The biphasic surfaces with re-entrant structures (described in paragraph 2.4.3.1.1) are analysed in this paragraph. The contact angle values of different surfaces are shown in Figure 56. All surfaces have the same base contact angle of 28° , and same top-structures diameter (10 μm). Four different pitch distances are considered for each surface; hence four different solid fractions

are considered in the analysis. Since the structures that compose the surfaces have a re-entrant shape, these surfaces present a composite interface that can be studied with the Cassie-Baxter equation.

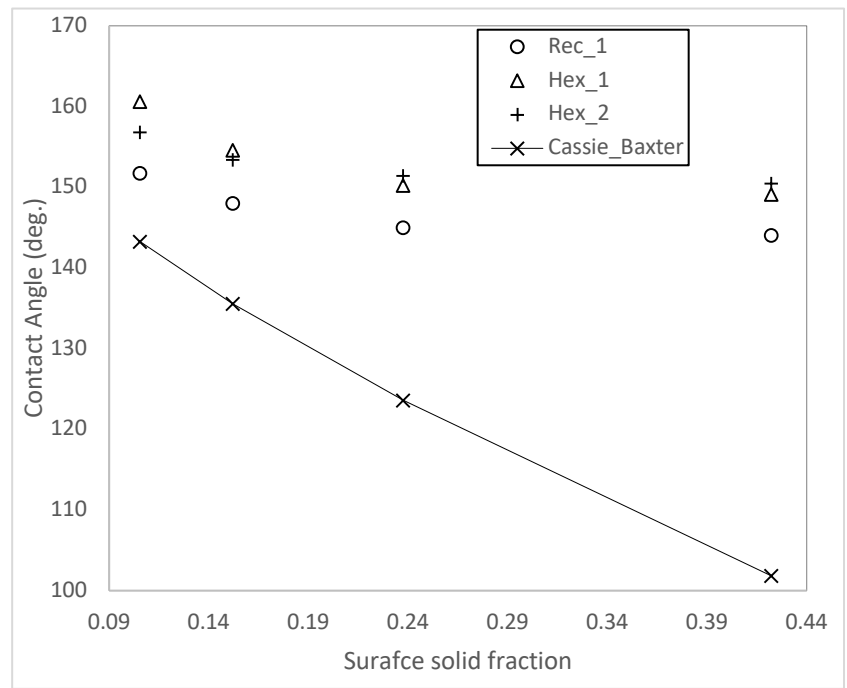


Figure 56: Contact angle values of mushrooms like structures. The Cassie-Baxter equation is implemented considering the geometries of the structures that compose the surfaces and their base contact angle.

From Figure 56 it can be inferred that all surfaces have a composite interface under the drop, Cassie-Baxter state. The values of contact angles measured are even larger than the ones calculated with the Cassie-Baxter equation. In the case of intrinsically hydrophobic surfaces this increase of contact angle can be explained with a partial impalement of the drop on the structures, but this explanation cannot be applied for intrinsically hydrophilic surfaces. In fact, a partial impalement of the drop would not be physically possible as a jump from the composite interface to complete wetting would occur, even if possible, it would lower the values of contact angle down rather than increasing it. A more realistic explanation relates with the deformation of the membrane composing the upper part of the pillars. As a matter of fact the membrane may undergo elasto-capillarity in contact with the drop [170], since the silicon dioxide membrane is 100 nm thick. This explanation is verified by the values of contact angles: in fact, Hex_1 and Rec_1 have the exact same membrane geometry and material, but they have different contact angle values. The only difference between the two surfaces is that the stem that holds the dioxide membrane is about 0.7 μm thicker on the Rec_1 structures. This difference allows the membrane to deform more on the Hex_1 mushroom structures rather than on Rec_1, allowing the Hex_1 to reach higher contact angle values to respect Rec_1. On the other hand,

Hex_2 has been realized with a slightly different process that produces structures almost identically to the Hex_1 structures, as can be observed in contact angle values.

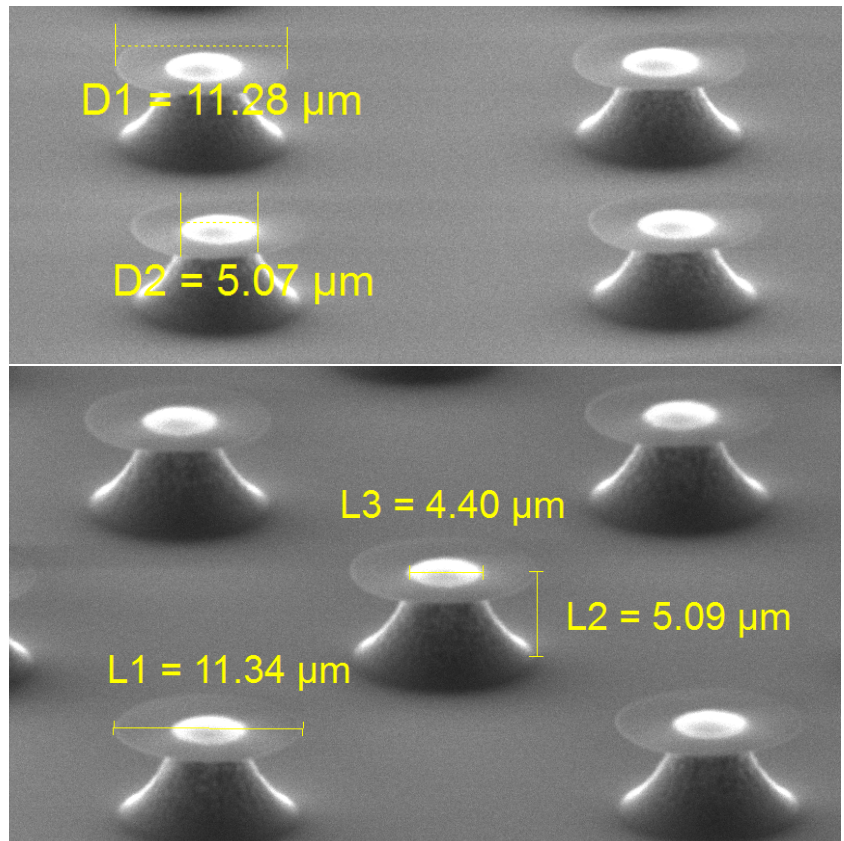


Figure 57: SEM images of Rec_1 surfaces (top) and Hex_1 surface (bottom), with the relative measurements on the microstructures.

6.8 Conclusions

In this chapter, we have analysed and compared the wettability properties with the stability of different hierarchical surfaces, coated with a slightly hydrophilic self-assembly monolayer. Butterfly inspired surfaces, composed of hierarchical re-entrant structures, are compared with geometrically similar lotus leaf inspired surfaces. We have demonstrated that all these surfaces can reach superhydrophobicity under a metastable condition. Only butterfly-inspired surfaces, thanks to their re-entrant structures, demonstrated to have an energy barrier that allows the metastable Cassie-Baxter state to hold in hard condition. Our best surface, from hydrophilic substrate, reached a CA of 160° , and a sliding angle of 3° . We have introduced a brief wear analysis of our butterfly-inspired surfaces. Thanks to this analysis, we have illustrated the importance of the wear resistance during surface design. In conclusion, we have demonstrated that with a hydrophilic substrate it is not possible to obtain a robust composite interface without re-entrance structures.

7 Water-walking-like tuneable surfaces

7.1 Abstract

In this chapter, we analyse the possibility of tuning the wettability properties of polydimethylsiloxane (PDMS) microstructured surfaces through stretching. We have realized surfaces inspired by the hairy leg of some water walking insects on a thin PDMS-membrane. The membranes have then been stretched, and the change in contact angle observed. The pyramidal elements composing the microstructured-PDMS membranes increase in their vertex angle as the membrane is stretched. This allows the drop to progressively impale on the structures. The stability of the wettability state on these structures has been analysed both theoretically and experimentally. We have further observed how the elasto-capillarity of the soft-substrate influences the metastability of Cassie-Baxter state over Wenzel state. Moreover, we have created spike-like structures to prove with experiments the theory used. A test has been performed to evaluate the robustness of the Cassie-Baxter state of the surfaces. The test consists in the physical compression of the drop on the surfaces in order to promote the transition from Cassie to Wenzel. As it is argued in theory, PDMS surfaces do not pass the stability test while silicon spike-like surfaces do.

7.2 Introduction

For more than two decades natural surfaces with superhydrophobic and self-cleaning properties have drawn the attention of scientists. Nowadays this is partially caused by the potential commercial application of synthetic surfaces which such properties. The most

common example of natural superhydrophobic surfaces is the leaf of lotus plant (*Nelumbo nucifera*). Along with lotus leaf, other examples can be reported, such as the leaf of *Salvinia molesta*, red rose petal, and hawkmoth or butterfly wings [171]. All these surfaces have in common pillar-like structures which often are characterized by a hierarchical level or even particular properties, such as hydrophilicity, on top of the hydrophobic structure [172]. Another kind of structure is proposed by the hairy legs of water-walking arthropods [173]. In particular, these insects are known to be able to walk, hunt and jump on the water surface. Apart from the robustness of the Cassie-Baxter state, what is interesting in these hairy structures is the need of having a low pull-off pressure from the water surface. As a matter of fact, hydrophobic conical structures – similar to one of water-walking insects' hair- are able, theoretically speaking, to reduce the pull-off pressure, [164]. This becomes more evident for slender structures where the vertex angle is low, as the one observed in Figure 58h.

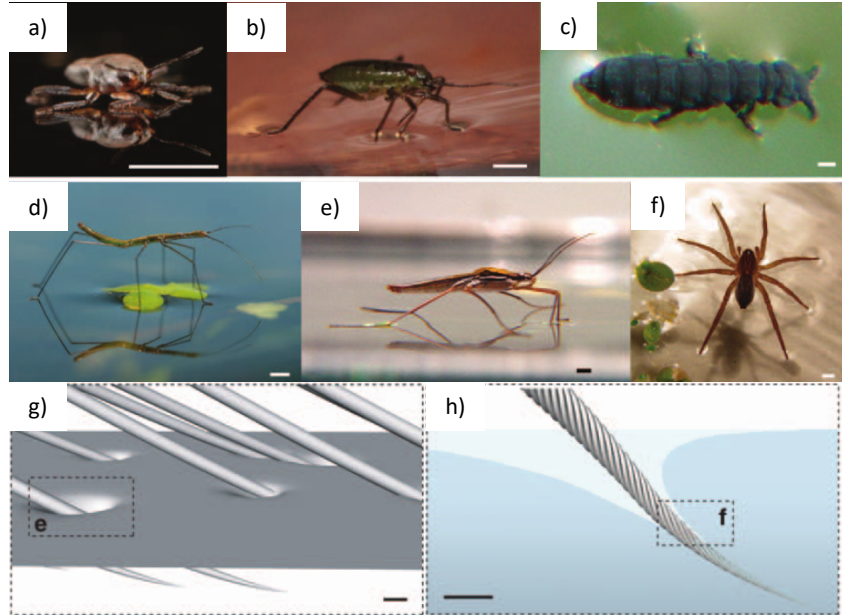


Figure 58: a)-f) images of insects able to walk on water (water-walking arthropods). Scale bar 1 mm. g)-h) representation of hydrophobic air of water-walking arthropods at different magnification. Scale bar 1 μm . Image adapted from [173].

In fact, it is possible to change the vertex angle of an array of conical pillars to precisely tune the wettability properties of the surface. Different and rather complex techniques have been used to tune the wettability of a surface such as optic, magnetic, mechanical, chemical, thermal or electric [174]. What we propose in this chapter is a simple method to tune the contact angle by stretching along one direction the sample. The polydimethylsiloxane (PDMS) sample has been

microstructured by direct moulding, where the microstructures of surfaces are pyramidal-like structures. While the sample is stretched, the vertex angle of each pyramidal element varies and the wettability of the substrate varies as a consequence. In the chapter, we have also realized silicon-based surfaces with pyramidal pillars to use them as reference with respect to the PDMS one and silicon-based spike-like surfaces which manage to reach high contact angle and great water-penetration resistance.

7.3 Polydimethylsiloxane samples with pyramidal pillars.

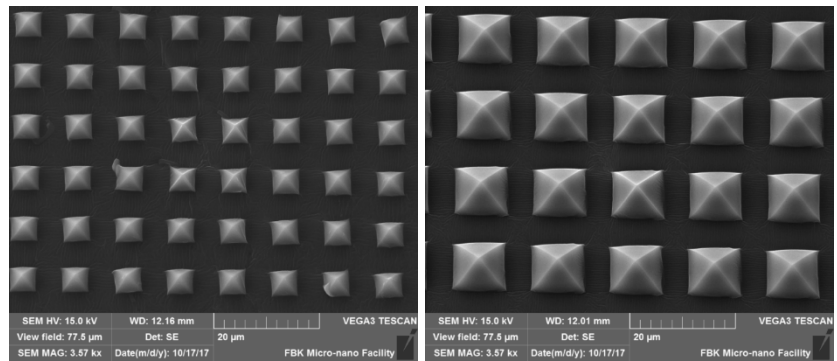
7.3.1 Samples Preparation

Polydimethylsiloxane (PDMS - Sylgard 184®) samples have been realized through a direct copy of a microstructured silicon substrate.

The microstructured pattern has been realized on a silicon mono-crystal wafer, grain orientation 100, through a MOS-like process. The process consists in the following steps: thermal oxidation, photolithography, dry etching of silicon dioxide, and silicon wet etch. The silicon dioxide is used as hard mask for the silicon wet etch of tetramethylammoniumhydroxide (TMAH), while the photolithography defines the microstructures and the dry etch removes the silicon dioxide where it is not covered with the photoresist. TMAH is used to obtain pyramidal structures, thanks to its extreme selectivity on silicon-dioxide and on <111> plane of silicon. As the last step, silicon dioxide mask has been removed with a wet etch of BHF. This etch

allows to remove the dioxide without further etching the silicon substrate. To avoid stitching of PDMS during the moulding process, the surface has been then coated with methyltrichlorosilane (MTCS). PDMS has been degassed both before and after deposition on the silicon substrate and then cured at 120 °C for 30 min.

Every tested pattern has been impressed on a square area of 1 cm² and at the end four different patterns have been realized: pyramidal pillars with basis 5, 10, 15 or 20 µm which have a constant gap of 5 µm, Figure 59.



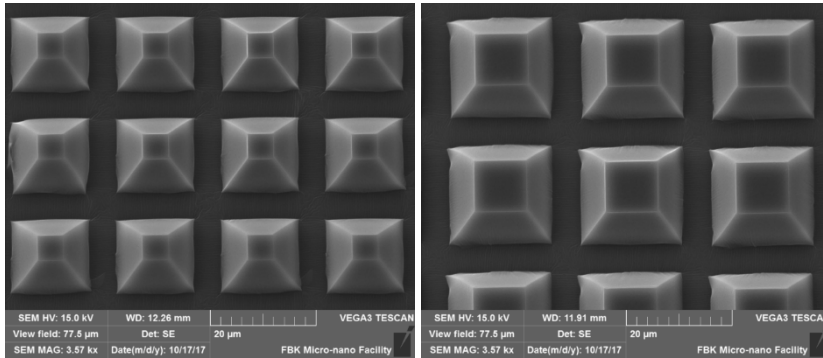


Figure 59: SEM images of PDMS samples. The samples have been coated with chrome, images have been taken after the stretch procedure. The stretch line between the pyramidal pillars can be easily found in the images. CW from top left surfaces 5x10, 10x15, 15x20 and 20x25 where the numbers are in micron. The first one indicates the dimension of the pyramidal pillar while the second the pitch distance between the pyramids.

7.3.2 Wettability test under stretch condition

The contact angle analysis has been performed on each surface at six different stretches: from no stretch up to 40% of elongation. Figure 60 shows the device used to stretch the PDMS samples. Each sample had a testing area of 100 mm², two clamps hold the two extremities of each sample. Precise measurement of the elongation was possible thanks to the precise roller instrument, since, by rotating it, the central piston moves to the right, displacing the right part of the clamp. A camera

opposed to a LED light source was able to capture some images of the drop settled on the microstructured-PDMS samples at different stretching conditions. For each measurement, four different drops have been settled on the surface. Then, a free software has analysed the contact angles of drops [114].

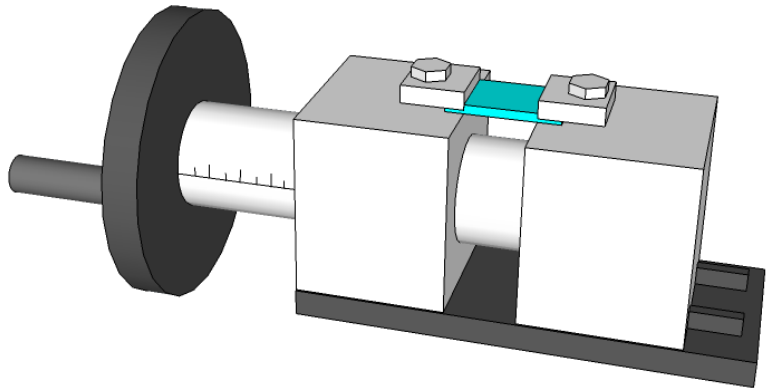


Figure 60: Device used to stretch PDMS sample. The left part of the device is fixed and by rotating the crank, the left part moves to the right. The sample, integrated with the fix and moving part of the device, is stretched when the right part moves.

7.3.3 Data analysis of pyramidal soft pillars

The graph in Figure 61 reports the contact angles value of each surface at different elongation. At resting position, with no-stretch, the surfaces are at Cassie-Baxter state. As a matter of fact, at a Wenzel

state, the values of contact angle for each surface would be much lower, as showed in Table 18.

As the stretch increases, both the pitch distance and the vertex angle increase. The combination of these two factors allows the drop to penetrate in greater depth into the pyramidal elements of the surface. By increasing the pitch distance, the pressure supported by each element increases as well, while by increasing the vertex angle, each pyramidal element causes penetration of the water drop. The resulting contact angle is the combination of these two phenomena.

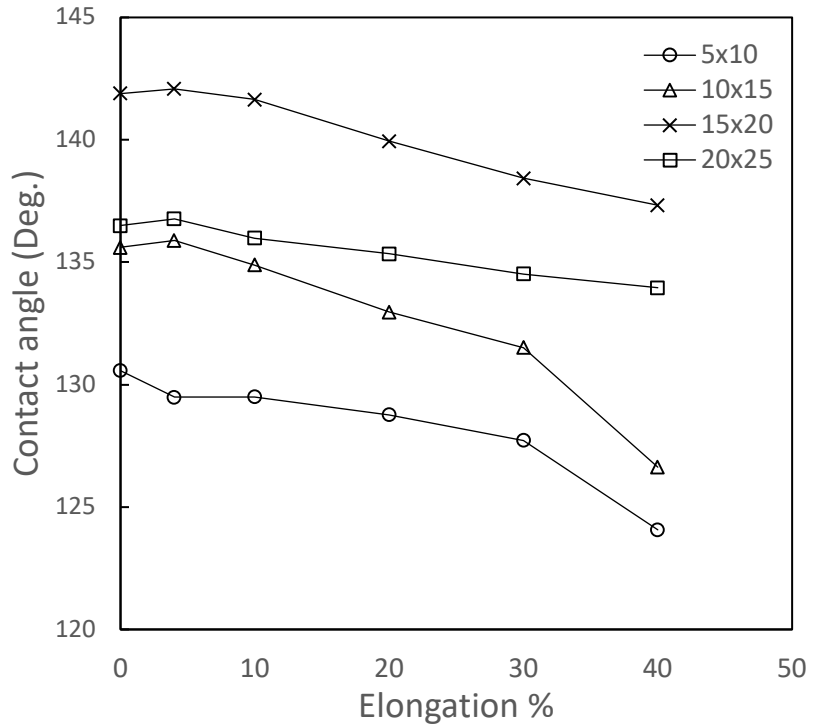


Figure 61: Graph of contact angle values varying with elongation. The trend tends to decrease as stretch increases due to the stretch of the pyramidal elements that cause top angle aperture.

From Figure 61, it is possible to observe how the contact angle measurement of PDMS-microstructured surfaces changes as the stretch increases. Contact angle decreases in all surfaces as the stretch increases mainly due to the increase of the vertex angle of the pyramidal elements. Second orders phenomena can influence this

behaviour, such as the elasto-capillarity [170] or the contraction of the direction which is perpendicular to the stretching direction, paragraph 0.

7.3.4 Stability of pyramidal pillars

The contact angle analysis demonstrates the possibility to tune the wettability of a surface by simply tracing a soft substrate made of pyramidal pillars along one dimension.

As the surface is stretched, so are the pyramidal pillars, and their vertex angle aperture increases. As shown theoretically, the bigger the aperture angle on top of conical pillars, the less hydrophobic the surface [164] and, as a result, the greater the stretch, the larger the vertex angle, the lower the contact angle.

Hence, the overture of the vertex angle of the pyramidal pillars defines the value of the contact angle of the surface. Since, we have realized these surfaces through a precise microfabrication process in which the base contact angle of pyramids is equal to 54.7° , implying that the vertex angle is 70.6° . In order to support a positive pressure and still keep a stable Cassie-Baxter state, the difference between the base contact angle and half of the vertex angle has to be greater than a right angle, $(\theta_e - \alpha) > 90^\circ$ [164]. The base contact angle of a flat surface of polydimethylsiloxane is around 107° , allowing a maximum vertex angle of 34° . This value lies below the half of the vertex angle of the considered pyramidal pillars, causing the metastability of the Cassie-

Baxter state. The plausible reason of this metastable state is the violation of the hypothesis of rigid substrate made in the theoretical calculation. As a matter of fact, PDMS produces an elasto-capillary effect in contact with water droplet [170], [175], [176]. In order to our thesis, we have firstly realized silicon based surfaces composed of pyramidal pillars and coated with a self-assembly monolayer of PF3. The realization of this surfaces has been rather simple and implied a process similar to the one used to obtain the matrix of PDMS moulding. The flat surface of silicon coated with PF3 has a contact angle of 106.8° , which is almost the same of flat PDMS. Furthermore, the silicon substrate can be considered rigid for the elasto-capillarity theory. Secondly, we have measured the contact angle on surfaces with pyramidal pillars and geometrical properties similar to the one of the PDMS. The value of contact angles measured on the surfaces indicates that the drop is in an impaled state, and that the surfaces are not in a metastable Cassie-Baxter state.

	<i>R1</i>	<i>R2</i>	<i>R3</i>
<i>Roughnes value</i>	1.07	1.11	1.16
<i>Wenzel CA</i>	107.4	108.0	109.0
<i>Measured CS</i>	107.5±0.43	108.7±0.41	109.2±0.36

Table 16: In the table the roughness factor, CA prediction with Wenzel equation, and measured CA value for three different reference silicon surfaces are reported.

These experimental data prove the hypothesis of elasto –capillarity effects influencing the stability of the Wenzel and Cassie-Baxter state. Furthermore, we calculate the amplitude of the meniscus produced by

the tension of the surface on the PDMS-pyramidal structures. The amplitude of the deformation at the triple line can be estimated by simply knowing Young's modulus of the substrate, liquid-air surface tension, and the base contact angle of the substrate [170] with the equation:

$$\delta \cong \frac{\gamma}{E} \sin \theta_b \quad (60)$$

This equation reveals a deformation of 70 nm for PDMS substrate which would be enough to generate a meniscus around each pyramidal pillar and to realize a physical barrier to the Cassie-Wenzel transition. In order to overcome this problem, we have realized an experimental setup that allows to force the drop inside the pillar and find the stable Wenzel state.

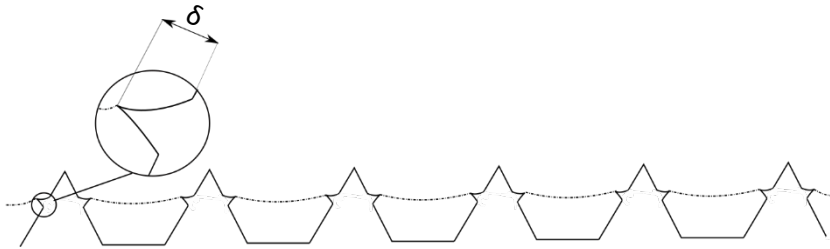


Figure 62: The sketch represents the pyramidal pattern deformed by the elasto capillarity of the water, the amplitude of the deformation where δ is represented as well.

7.4 Small angle spikes

As stated before, to have a stable Cassie-Baxter state over conical or pyramidal pillar the vertex angle has to observe the condition [164]:

$$(\theta_e - \alpha) > 90^\circ \quad (61)$$

Where θ_e is the base contact angle and α is half of the vertex angle, this condition comes from the equation defining the maximal pressure that a superhydrophobic surface can stand. The pressure is defined by the differences between internal pressure of the drop and external pressure:

$$\hat{p} = - \frac{\pi \left(\frac{\hat{r}}{2}\right) \cos(\theta_e - \alpha)}{1 - \pi \left(\frac{\hat{r}}{2}\right)^2} \quad (62)$$

Where \hat{p} is the pressure normalized by the linear semi-spacing between pillars λ and the liquid-air surface tension γ , and \hat{r} is the radius normalized by λ . The minimum requirement for a surface to sustain a positive pressure is to observe the condition of equation (61). In our specific case, the base contact angle of silicon substrate coated with SAM of PF3 is $\theta_e = 106.8^\circ$, leading to a semi-vertex angle $\alpha \leq 16.8^\circ$. We have realized spike like structures with semi-vertex angle of 2° , Figure 63, where the vertex of each structure is flat with a diameter of $1.5 \mu\text{m}$. These features introduce few differences with respect to a perfect conical surface. Other relevant differences are further explained.

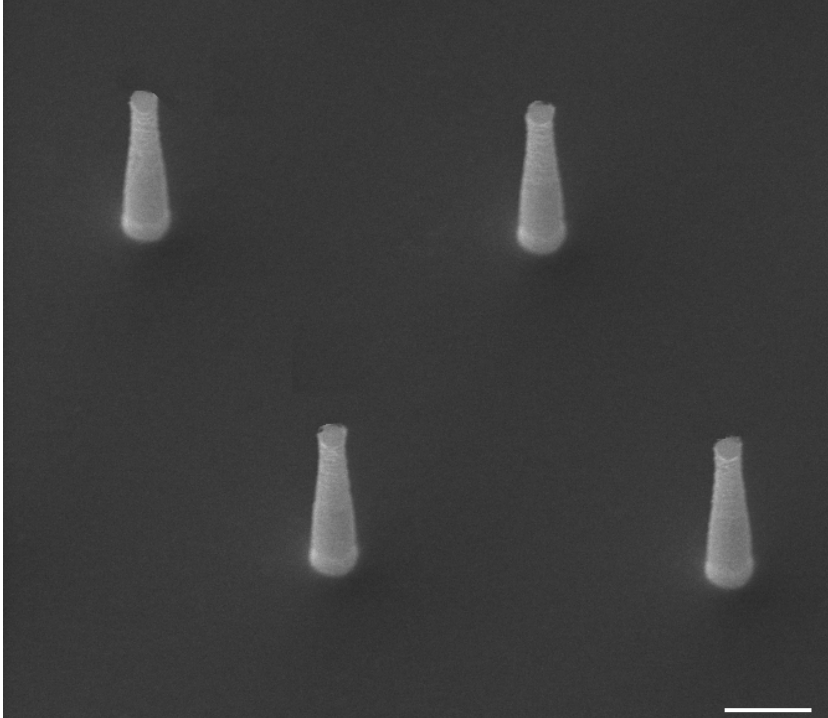


Figure 63: SEM image of the surface with spikes-like structures, which are not ideal conical structures but truncated cones with the upper diameter of $1.5\ \mu\text{m}$.

7.4.1 Stability of spikes pillars

In this paragraph, we analyze the stability of Cassie-Baxter state of surfaces Sk1 and Sk2 referring to the drop pressure [164]. Both

surfaces are composed of truncated cone structures, with upper diameters of $1.5\text{ }\mu\text{m}$, a semi-vertex angle of 2° , and $23\text{ }\mu\text{m}$ tall. The pitch distance of Sk1 structures is $20\text{ }\mu\text{m}$ and for Sk2 structures is $25\text{ }\mu\text{m}$. In our experiments, we used a $3\text{ }\mu\text{l}$ drop of deionized water and for theoretical analysis the air-liquid surface tension with the value $\gamma=72.75\text{ mN/m}$. By considering the water drop on a superhydrophobic surface with a shape of a perfect sphere, we calculate its radius as $r_{sp} = \sqrt[3]{\frac{3V}{4\pi}} \cong 0.89\text{ mm}$. Since this value is much smaller than the capillary length, k^{-1} , our assumption of a perfect spherical drop is accurate. From these data, we compute the pressure inside the drop, $p = \frac{2\gamma}{r_{sp}} = 162.6\text{ Pa}$. In order to check if the drop settled on the surface gets partially impaled on the spike-like structures, we have to compute the pressure that the upper part of the truncated cone can stand thanks to the equation (62), as reported in Table 17.

	Pressure
Sk1	249.1 Pa
Sk2	159.2 Pa

Table 17: In the table the maximal pressure values that the upper-flat part of the truncated cone can stand for each configuration are presented. The pressure that Sk1 is higher than the one reached on the drop, while the pressure on Sk2 is lower, meaning that the drop settled on surface Sk2 experiences a partial impalement on the structures.

The pressure of the top part of the surface Sk1 structure is sensibly higher than the one of the drop, meaning that the drop should not

experience impalement on the surface. On the other hand, the surfaces Sk2 cannot stand the pressure of the drop on the flat top part of the truncated cone structures, meaning that a partial impalement is required to achieve the stable condition.

By inverting the equation (62), we can compute the radius at which the triple line stand the pressure of the drop. From the value of the radius, the depth of impalement of the drop can be measured as well, and, consequentially, the value of contact angle. This value has been calculated using a modified Cassie-Baxter equation [163], [169], [177]:

$$\cos \theta_{app} = \varphi(r_f \cos \theta_0 + 1) - 1 \quad (63)$$

Where r_f is the roughness factor that, in our case, depends on the depth of impalement of the drop. We used the equation (63) to measure the theoretical contact angle value for the surface Sk2 and the standard Cassie-Baxter equation to measure the contact angle value for the surfaces Sk1, these values are reported in Figure 64.

7.4.2 Data analysis of spike pillars

Static contact angles (CA) of the two different surfaces (Sk1 and Sk2) are proposed, Figure 64, along with the value of advancing and receding contact angles, Figure 65. Static contact angles are compared with the Cassie-Baxter [21] and Wenzel [19], [20] predictions. Cassie-Baxter prediction has been modified in order to consider a penetration of the drop in the spikes structures [164], as expected from our calculations. We have observed that the Cassie-Baxter's CA prediction

is almost perfectly in compliance with our experimental data, the Cassie-Baxter state is stable for these two surfaces. Both static contact angle of the observed surfaces are really closed to 180°, suggesting a high level of hydrophobicity and hence a low hysteresis.

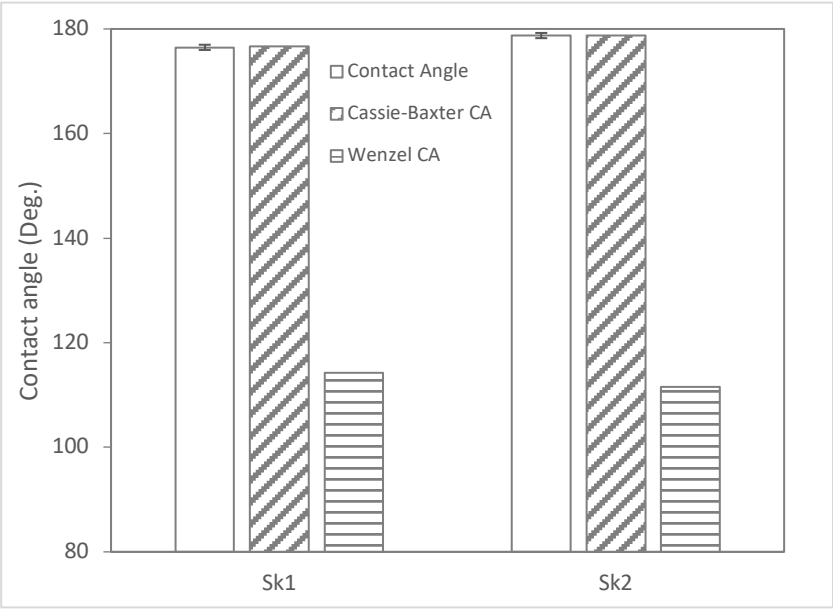


Figure 64: Static contact angle value, empty bars represent the measured contact angles with relative error bars. While the bars with the skew line refer to the prediction of contact angle according to Cassie-Baxter state for spike structures, the bars with the horizontal line refer to the Wenzel state.

In Figure 65, the value of advancing and receding contact angles are reported for the two surfaces Sk1 and Sk2, with the related standard deviation. From the value of the static contact angle, we expected a better behavior of the surface that has a greater contact angle that is Sk2. As a matter of fact, Sk2 has a greater area fraction with respect to Sk1, and this generally brings to a higher hydrophobic state. Both surfaces have values of advancing and receding contact angle close to the static contact angle. This situation makes hard to evaluate which surface is more hydrophobic. In order to find the difference between the two surfaces, we have to evaluate the contact angle hysteresis, defined as the difference between the cosine of the receding angle and the cosine of the advancing angle [12].

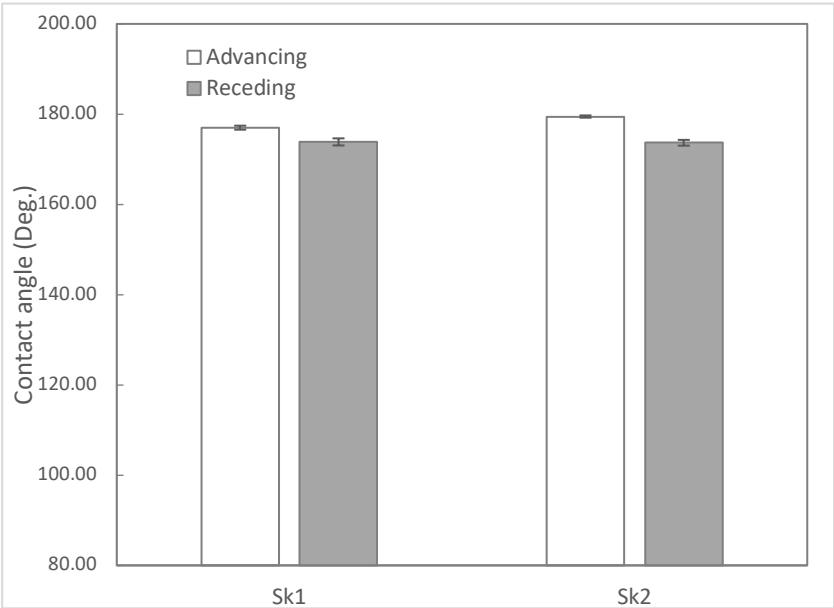


Figure 65: Values of advancing (empty bars) and receding (grey bars) contact angles, the errors bars represent the standard deviation of the dataset.

The contact angle hysteresis of the two surfaces Sk1 and Sk2 is here analysed. As stated in the previous section, Sk2 seems to have better wettability properties than Sk1.

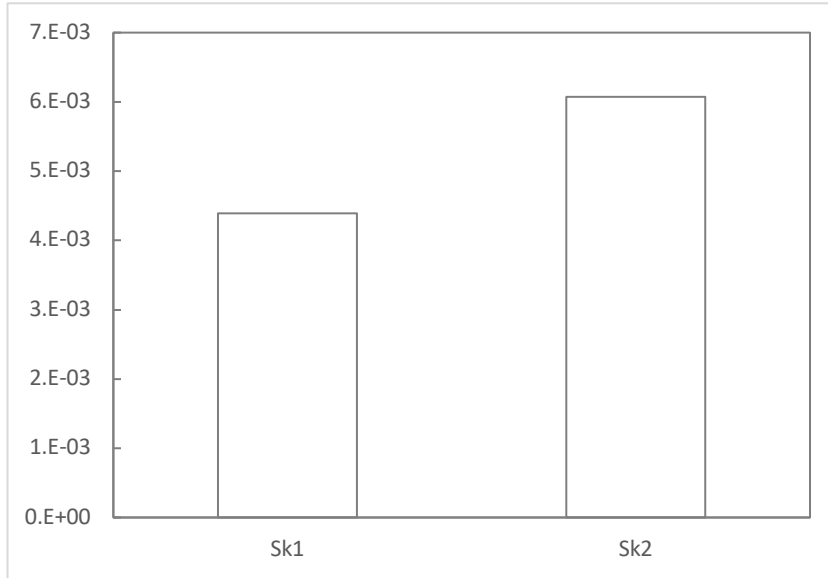


Figure 66: Contact angle hysteresis of the two surfaces Sk1 and Sk2. The hysteresis is calculated as $\Delta \cos \vartheta = \cos \theta_r - \cos \vartheta_a$.

The superhydrophobic properties of a surface cannot be evaluated just considering the contact angle value since the hysteresis plays a fundamental role in the evaluation process. By observing Figure 66, the hysteresis of Sk1 is lower than the hysteresis of Sk2. Even though both values are really low, the one with better properties is Sk1 due to the fact that the water drop does not penetrate the spike-like structures, but stays on the top. Actually, the pitch distance in Sk2 is

too large to guarantee a high enough pressure to maintain the drop only on the top of the structures. The water penetrates the spikes like structures of few microns and, then, it is partially impaled. This particular status generates a higher contact angle value for the Sk2 surface, but it negatively influences the hysteresis by making the surface less superhydrophobic. Both surfaces are highly hydrophobic, but the Sk1 would be a better choice rather than Sk2 for application where superhydrophobicity is required.

7.5 Cassie-Wenzel transition through compression

This test has been performed to experimentally ensure the stability of the Cassie-Baxter state over the Wenzel state. The procedure consists in compressing the drop between two superhydrophobic surfaces and observing the Contact angle value before and after the compression. During the process, the drop distorts as the two plates get closer to each other [178], supporting the Cassie to Wenzel transition. The experimental setup consists in a mobile plate controlled by a manual roller. The stage translates vertically to squeeze the water droplet settled on the sample surface. The surface of the moving stage in contact with the water droplet is superhydrophobic in order to avoid the drop to stick on it. Figure 67 shows the sketch of the setup used to perform the experiment. The procedure has been standardized to achieve good repeatability: first, the deionized water drop is settled by using a syringe on the planar sample, then a gentle shake allows the drop to reach a local minimum. Afterwards, the moving stage is brought in contact with the upper part of the drop and lowered further to squeeze the drop. As soon as the drop moves to Wenzel state, the

experiment stops and the stage is raised up. If the transition does not occur, the stage is lowered to an arbitrary low point and raised back up. A camera and a homogenous light source are perpendicularly placed to observe and record the processes.

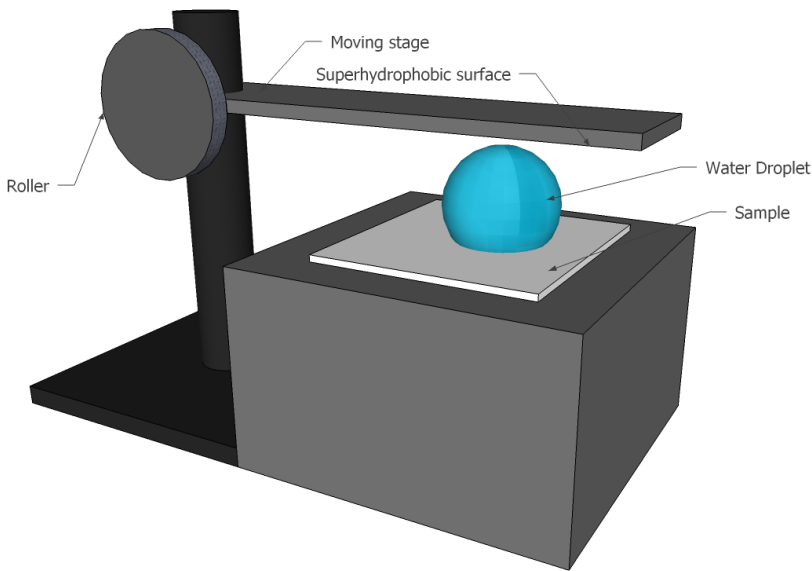


Figure 67: Sketch of the experimental setup used to compress the water droplet on the analyzed sample.

7.5.1 Compression of PDMS pyramidal pillars

Contact angles measured on the PDMS samples show the presence of an air cussing under the drop. This state is supposed to be a metastable state, since the vertex angle of the pyramidal pillar, of 70.6 degrees, is large enough to impose the Wenzel state at the surface. The theory used to perform this calculation [164] is efficient only with rigid substrate, while the PDMS, like other elastomers [175], is known to undergo phenomena of elasto-capillarity [170] and locally deform in contact with water [176]. By taking into account the Young's modulus of the substrate, the deformation at the triple line given by the water surface tension is roughly calculated to be 70 nm. This deformation is on each pillar and generates a barrier blocking the advancement of the triple line, this geometrical deformation of the substrate represents a physical barrier between Cassie-Baxter and Wenzel state. In order to overcome this barrier the drop is compressed into the surface. Figure 68 shows the sequence of the squeezing process: the drop is first settled on the surface to analyze, then squeezed till the Cassie to Wenzel transition occurs, the upper stage is moved away and the image of the drop is recorded again.

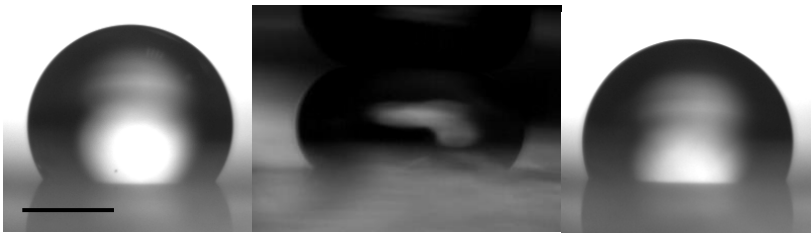


Figure 68: The sequence of images shows the time lapse of a water drop compressed on the micro-structured PDMS surfaces. The contact angle of the drop before the compression is of 125 degrees and switches to 111 degrees after compression. The first value involves the presence of air under the drop (Cassie-Baxter state), while the second value refers to a full wetting of the surface (Wenzel state). Scale refers to 0.8 mm, the drop volume is of 2 μl .

This procedure has been performed three times on each PDMS-microstructured surface and a sequence of images of drop before and after squeezing has been recorded. Thanks to a specialized software [114], the contact angles have been measured and then compared with the Wenzel prediction for each geometry. Table 18 reports the value of contact angle before and after the squeezing for each surface and the contact angle calculated with the Wenzel equation.

	CA before	CA after	CA Wenzel
A	125,4 \pm 4.8	111,3 \pm 0.9	114,8
B	127,0 \pm 5.6	113,4 \pm 2.32	118,3

<i>C</i>	132,8±2.1	118,3±1.7	123,0
<i>D</i>	135,2±3.9	118,1±3.7	122,4

Table 18: results of contact angle values on microstructured-PDMS samples before and after the squeezing procedure compared with the contact angle prediction with Wenzel equation. Mistakes linked with experimental data represent the standard deviation of each dataset.

The contact angles value measured on the drops after the squeezing procedure indicates that the drop completely pours the surface. The values differ slightly from the Wenzel prediction, being systematically lower. The main reason justifying the presence of this gap is not to be searched in the elasto-capillarity phenomenon, but rather in the contact angle hysteresis. In fact, as the drop is pressed into the surface, it increases in his contact area as a consequence. When the upper stage has removed the change of wet area below, the drop depends on the contact angle hysteresis. This influences the contact angle value by slightly shifting it towards the receding angle.

7.5.2 Compression of silicon low angle spikes

The contact angles measurements performed on the surfaces composed of spike-like structures with low top angle, 4°, show an air cussing under the drop. The analytical calculation demonstrates the stability of this state for both the considered surfaces. The silicon can be considered rigid for elasto-capillarity, and the validity of this theory perfectly complies with these surfaces. In order to prove the stability of these surfaces, we have performed the compression tests above described. Figure 69 shows the time lapse of the experimental procedure.



Figure 69: The images sequence shows the time lapse of a water drop compressed on the microstructured silicon surface. The contact angle of the drop before and after the compression does not change meaning that the air cussing under the drop resists the pressure of squeezing and that the Cassie-Baxter state is stable, as analytically predicted. Scale refers to 0.8 mm, the drop volume is of 3 μ l.

Contact angle values measured before and after the squeezing show how both surfaces, Sk1 and Sk2, have stable Cassie-Baxter state. The Contact angle does not vary in a significant way before and after the compression tests, Table 19.

	CA before	CA after	CA Wenzel
Sk1	176,48 \pm 0.52	175,31 \pm 0.54	114,23
Sk2	178,74 \pm 0.46	178,02 \pm 0.20	111,59

Table 19: results of contact angle values before and microstructured silicon base surfaces after the squeezing procedure compared with the

contact angle prediction with Wenzel equation. Mistakes linked with experimental data are the standard deviation of each dataset.

The experimental procedure demonstrates that the Cassie-Baxter state is stable for both surfaces, Sk1 and Sk2. The contact angle values measured after compression are lower than the one measured before compression, reinforcing the previous hypothesis formulated about contact angle value being shifted towards the receding angle.

7.6 Conclusion

In the chapter, we presented different surfaces composed of pyramidal or spike-like structures, two materials have been used to realize the surfaces: polydimethylsiloxane and silicon coated with a hydrophobic self-assembled monolayer. The pyramidal-like structures made of PDMS have a metastable Cassie-Baxter state and, thanks to this, it is possible to vary their wettability properties by stretching the membrane. This metastable Cassie-Baxter state is due to an elasto-capillarity phenomenon that involves every single pillar under by the water droplet. By using a simple technique, we have promoted on the PDMS surfaces the transition from Cassie to Wenzel state. The technique consists in compressing the drop on the surface thanks to a superhydrophobic surface positioned parallel to the tested surface. Furthermore, silicon-based spikes-like structures have been realized and tested. Thanks to their small vertex angle, these surfaces maintain superhydrophobic properties even under compression.

8 Conclusion

This work depicts and discusses the design, fabrication, and characterization of a range of bioinspired and multifunctional microstructured surfaces, particularly focusing on bioinspired surfaces with specific properties related to their interaction with water.

Several features of natural surfaces are of interest for industrial application. Self-cleaning, low adhesion and reduced fluid drag of superhydrophobic materials, inspired e.g. from lotus leaves or sharkskin, are some of the properties studied and depicted by this work. Such natural surfaces with their peculiar properties have been imitated to produce synthetic surfaces with these advanced functionalities. This work further describes methods and results targeting the combination of such natural surface topographies in order to achieve multifunctional properties into a single substrate.

All the work was carried out in a class 100 clean room for CMOS-compatible lithography, typically used for fabrication of microelectronic devices, e.g. silicon detectors and MEMS. This process, carried out on 6 inch wafers, features horizontal submicrometric precision (in the order of 365 nm) and

repeatability allowing for the fabrication of high aspect ratio structures, maintaining similar precision along the vertical direction as well. The caveats of this choice are the fact that the starting substrate for the fabrications is necessarily a silicon wafer (with the necessity of flat area), and the cost of the related microfabrication pilot line.

8.1 Artificial surfaces

A series of surfaces with single-level or hierarchical structures have been designed, fabricated and characterized in order to obtain a set of multifunctional surfaces for different practical applications. The stability of the Cassie-Baxter state of each set of structures has been analysed with *ad hoc* mathematical models. An energy base approach has been proposed to compare the superhydrophobic level of the realized surfaces.

8.1.1 Lotus leaf-inspired random hierarchical surfaces

The first set of realized surfaces features a hierarchical combination of pillar-like structures with surface texturing. The texturing, realized with a fast wet etching technique, has been used as a second hierarchical level. It further improves the contact angle of about 6.5%, reaching up to 171°. Despite this asset, the textured surfaces have some drawbacks such as pyramidal roughness which could not guarantee the stability of the Cassie-Baxter state.

8.1.2 Lotus leaf-inspired deterministic hierarchical surfaces

Thus, in order to improve the Cassie-Baxter stability, the second set of surfaces has been fabricated with precise hierarchical pillar-like structures using double lithography CMOS techniques. The fabricated structures show stable contact angle values higher than 160° with a contact angle hysteresis of about 1° , five-time lower than the single-level structures.

8.1.3 Sharkskin-inspired structures

A surface with sharkskin-inspired structure, designed with the geometrical parameters suggested by other researches to have the best performance, have been fabricate using CMOS techniques. This surface, even if not superhydrophobic, is able to reduce of about three times the pressure drop (linked to skin-friction), as observed during a test with a water flow along a rectangular channel with or without such texturing.

8.1.4 Hierarchical combination of sharkskin and single-level lotus leaf surfaces

Another pilot run of double lithography CMOS process was used for the fabrication of a hierarchal combination of sharkskin and single-level lotus leaf-inspired pillared structures. These superhydrophobic multifunctional surfaces combine the skin-friction reduction properties of both lotus leaf and sharkskin. The

hierarchical surfaces have been compared with the aforementioned sharkskin-inspired structure and two different single-level superhydrophobic surfaces inspired by lotus leaf. Characterisation results show that the best hierarchical surface manages to reduce pressure drop by 10% compared to the sharkskin-inspired surface and 40% compared to the best result for the lotus leaf-inspired surfaces.

8.1.5 Namib Desert beetle-inspired surfaces, with heterogeneous chemistry

The fifth set of surfaces was realized using a CMOS process modified to imitate the chemically heterogeneous surface that the Namib Desert beetle uses to harvest water from environmental fog. The presence of a heterogeneous chemistry over each pillar of the produced surfaces enhances this property. In fact, the surfaces are composed of pillar-like structures which have both a hydrophilic chemistry on the top part and a hydrophobic chemistry on the side and bottom parts. These surfaces have been cross-compared with geometrically identical structures which have an intrinsically hydrophobic or hydrophilic chemistry. The surfaces with a heterogeneous chemistry show better results in collecting water than both chemically homogeneous surfaces. The heterogeneous surface with best-collecting property manages to harvest up to 24% more water (per unit area and time) with respect to its hydrophilic

corresponding surface and 85% more with respect to the hydrophobic one.

8.1.6 Butterfly-inspired surfaces, with re-entrant structures

The sixth set of surfaces was realized based on a concept that an intrinsically hydrophilic substrate can generate a superhydrophobic surface due to presence of re-entrant structures, e.g. as found on butterfly wings. Surfaces with re-entrant structures have been fabricated using a combination of anisotropic and isotropic dry etchings. These surfaces show superhydrophobic properties arising from hydrophilic substrates. The re-entrant part present on each structure causes an energy barrier to water penetration, which cannot pass from a superhydrophobic metastable composite interface to a stable full-wet state. Moreover, several tests have been performed to verify the robustness of the Cassie-Baxter state and the mechanical resistance of the structure itself. In our tests, some of the surfaces have reached contact angle values higher than 160° and tilting angles lower than 3° ; these properties arise from a base contact angle of 77.5° .

8.1.7 Water walking-inspired stretchable surfaces, with pyramidal-like structures

The seventh set of surfaces consists of micropatterned pyramidal-like elastomer structures produced using a patterned silicon wafer as a mould. In these surfaces, the contact angle of elastic structures inspired by hairs on the legs of water-walking insects has been studied as a function of pyramidal-pillars vertex angle. The micropatterned soft-substrates have a composite interface at the triple line, and it was possible to observe a contact angle variation on the surfaces upon stretching. In contact with water, the surfaces of the soft substrates are affected by elasto-capillarity as well. This phenomenon influences the wettability properties of the patterned surfaces by forming a metastable composite interface.

8.1.8 Water walking-inspired surfaces, with truncated-conical silicon structures

The eight set of surfaces consists of silicon truncated conical structures fabricated with CMOS-like process that includes a semi-isotropic dry etching. Test results showed stability of Cassie-Baxter state as expected from a mathematical model. They also revealed higher resistance to water penetration and superhydrophobic properties with respect to the stretchable pyramidal-pillar structures reported in the previous section.

8.2 Outlook and future work

The results of this work provide a new approach of the design and fabrication of multifunctional bioinspired surfaces. In particular, the fabricated hierarchical combined structures show combined properties even superior than their not-combined counterparts; this paves the way for future developments in surface engineering of multifunctional surfaces, and allows to use the data and results of this work to fasten the design cycle of multifunctional surfaces.

The use of the processes and materials of this R&D activity perfectly fits with the laboratory scale, e.g. lab on chip and microfluidics apparatus. Nevertheless, it needs further work to be applied on an industrial scale.

9 References

- [1] W. Barthlott and C. Neinhuis, "Purity of the sacred lotus, or escape from contamination in biological surfaces," *Planta*, vol. 202, no. 1, pp. 1–8, 1997.
- [2] T. Darmanin and F. Guittard, "Superhydrophobic and superoleophobic properties in nature," *Mater. Today*, vol. 18, no. 5, pp. 273–285, 2015.
- [3] S. Wang and L. Jiang, "Definition of superhydrophobic states," *Adv. Mater.*, vol. 19, no. 21, pp. 3423–3424, 2007.
- [4] X.-M. Li, D. Reinhoudt, and M. Crego-Calama, "What do we need for a superhydrophobic surface? A review on the recent progress in the preparation of superhydrophobic surfaces," *Chem. Soc. Rev.*, vol. 36, no. 8, p. 1350, 2007.
- [5] J. B. Brzoska, I. Ben Azouz, and F. Rondelez, "Silanization of Solid Substrates: A Step toward Reproducibility," *Langmuir*, 1994.
- [6] G. D. Nadkarni and S. Garoff, "Reproducibility of Contact Line Motion on Surfaces Exhibiting Contact Angle Hysteresis," *Langmuir*, 1994.
- [7] A. DeSimone, N. Grunewald, and F. Otto, "A new model for contact angle hysteresis," *Networks Heterog. Media*, 2007.
- [8] H. Kusumaatmaja and J. M. Yeomans, "Modeling contact angle hysteresis on chemically patterned and superhydrophobic surfaces," *Langmuir*, 2007.
- [9] G. McHale, N. J. Shirtcliffe, and M. I. Newton, "Contact-angle

hysteresis on super-hydrophobic surfaces,” *Langmuir*, 2004.

- [10] C. W. Extrand, “Model for contact angles and hysteresis on rough and ultraphobic surfaces,” *Langmuir*, 2002.
- [11] S. Brandon, A. Wachs, and A. Marmur, “Simulated Contact Angle Hysteresis of a Three-Dimensional Drop on a Chemically Heterogeneous Surface: A Numerical Example,” *J. Colloid Interface Sci.*, 1997.
- [12] M. Reyssat and D. Quéré, “Contact Angle hysteresis generated by strong dilute defects,” *J. Phys. Chem. B*, vol. 113, no. 12, pp. 3906–3909, 2009.
- [13] F. Schellenberger, N. Encinas, D. Vollmer, and H. J. Butt, “How Water Advances on Superhydrophobic Surfaces,” *Phys. Rev. Lett.*, vol. 116, no. 9, pp. 2–7, 2016.
- [14] L. Gao and T. J. McCarthy, “The ‘lotus effect’ explained: Two reasons why two length scales of topography are important,” *Langmuir*, vol. 22, no. 7, pp. 2966–2967, 2006.
- [15] T. Nishino, M. Meguro, K. Nakamae, M. Matsushita, and Y. Ueda, “The lowest surface free energy based on -CF₃ alignment,” *Langmuir*, 1999.
- [16] M. Nosonovsky, “On the range of applicability of the Wenzel and Cassie equations,” *Langmuir*. 2007.
- [17] G. McHale, “Cassie and Wenzel: Were they really so wrong?,” *Langmuir*, 2007.

-
- [18] D. Kim, N. M. Pugno, and S. Ryu, "Wetting theory for small droplets on textured solid surfaces," *Sci. Rep.*, vol. 6, no. 1, p. 37813, 2016.
- [19] R. N. Wenzel, "Resistance of solid surfaces to wetting by water," *Ind. Eng. Chem.*, vol. 28, no. 8, pp. 988–994, 1936.
- [20] R. N. Wenzel, "Surface Roughness and Contact Angle," *J. Psychosom. Res.*, vol. 53, no. 9, pp. 1466–1467, 1949.
- [21] B. D. Cassie, A. B. D. Cassie, and S. Baxter, "Wettability of porous surfaces," *Trans. Faraday Soc.*, vol. 40, no. 5, pp. 546–551, 1944.
- [22] J. Bico, U. Thiele, and D. Quéré, "Wetting of textured surfaces," *Colloids Surfaces A Physicochem. Eng. Asp.*, vol. 206, no. 1–3, pp. 41–46, 2002.
- [23] K. Tsougeni, N. Vourdas, A. Tserepi, E. Gogolides, and C. Cardinaud, "Mechanisms of oxygen plasma nanotexturing of organic polymer surfaces: From stable super hydrophilic to super hydrophobic surfaces," *Langmuir*, 2009.
- [24] C. F. Lin, C. H. Wu, and Z. N. Onn, "Degradation of 4-chlorophenol in TiO₂, WO₃, SnO₂, TiO₂/WO₃ and TiO₂/SnO₂ systems," *J. Hazard. Mater.*, 2008.
- [25] F. Bottiglione, R. Di Mundo, L. Soria, and G. Carbone, "Wenzel to Cassie Transition in Superhydrophobic Randomly Rough Surfaces," *Nanosci. Nanotechnol. Lett.*, vol. 7, no. 1, pp. 74–78, 2015.
- [26] M. Nosonovsky and B. Bhushan, "Stochastic model for metastable wetting of roughness-induced superhydrophobic

- surfaces," *Microsyst. Technol.*, vol. 12, no. 3, pp. 231–237, 2006.
- [27] A. Giacomello, M. Chinappi, S. Meloni, and C. M. Casciola, "Metastable wetting on superhydrophobic surfaces: Continuum and atomistic views of the cassie-baxter-wenzel transition," *Phys. Rev. Lett.*, vol. 109, no. 22, pp. 1–4, 2012.
- [28] Y. Li, W. Z. Jia, Y. Y. Song, and X. H. Xia, "Superhydrophobicity of 3D porous copper films prepared using the hydrogen bubble dynamic template," *Chem. Mater.*, 2007.
- [29] E. Bormashenko *et al.*, "Superhydrophobic Metallic Surfaces and Their Wetting Properties," *J. Adhes. Sci. Technol.*, 2008.
- [30] N. a Patankar, "On the Modeling of Hydrophobic Contact Angles on Rough Surfaces On the Modeling of Hydrophobic Contact Angles on Rough," *Society*, vol. 19, no. January, pp. 1249–1253, 2003.
- [31] C. Ishino, K. Okumura, and D. Quéré, "Wetting transitions on rough surfaces," *Europhys. Lett.*, vol. 68, no. 3, pp. 419–425, 2004.
- [32] G. Whyman and E. Bormashenko, "Wetting Transitions on Rough Substrates: General Considerations," *J. Adhes. Sci. Technol.*, vol. 26, no. 20, pp. 207–220, 2012.
- [33] N. A. Patankar, "Transition between superhydrophobic states on rough surfaces," *Langmuir*, 2004.

-
- [34] L. Barbieri, E. Wagner, and P. Hoffmann, "Water wetting transition parameters of perfluorinated substrates with periodically distributed flat-top microscale obstacles," *Langmuir*, 2007.
- [35] R. David and A. W. Neumann, "Energy barriers between the Cassie and Wenzel states on random, superhydrophobic surfaces," *Colloids Surfaces A Physicochem. Eng. Asp.*, 2013.
- [36] M. E. Kavousanakis, C. E. Colosqui, I. G. Kevrekidis, and A. G. Papathanasiou, "Mechanisms of wetting transitions on patterned surfaces: continuum and mesoscopic analysis," *Soft Matter*, 2012.
- [37] N. T. Chamakos, M. E. Kavousanakis, and A. G. Papathanasiou, "Enabling efficient energy barrier computations of wetting transitions on geometrically patterned surfaces," *Soft Matter*, 2013.
- [38] S. E. Friberg, "Wetting of Real Surfaces, Edward Yu. Bormashenko. De Gruyter, Berlin (2013)," *J. Colloid Interface Sci.*, 2014.
- [39] Y. C. Jung and B. Bhushan, "Dynamic effects of bouncing water droplets on superhydrophobic surfaces," *Langmuir*, 2008.
- [40] D. Bartolo, F. Bouamrène, É. Verneuil, A. Buguin, P. Silberzan, and S. Moulinet, "Bouncing or sticky droplets: Impalement transitions on superhydrophobic micropatterned surfaces," *Europhys. Lett.*, 2006.
- [41] M. Nosonovsky and B. Bhushan, "Patterned Nonadhesive surfaces: Superhydrophobicity and wetting regime transitions," *Langmuir*, vol. 24, no. 4, pp. 1525–1533, 2008.

- [42] S. Moulinet and D. Bartolo, “Life and death of a fakir droplet: Impalement transitions on superhydrophobic surfaces,” *Eur. Phys. J. E*, 2007.
- [43] Y. C. Jung and B. Bhushan, “Wetting transition of water droplets on superhydrophobic patterned surfaces,” *Scr. Mater.*, 2007.
- [44] G. McHale, S. Aqil, N. J. Shirtcliffe, M. I. Newton, and H. Y. Erbil, “Analysis of droplet evaporation on a superhydrophobic surface,” *Langmuir*, 2005.
- [45] A. Lafuma and D. Quéré, “Superhydrophobic states,” *Nat. Mater.*, vol. 2, no. 7, pp. 457–460, 2003.
- [46] Y. Wang, L. Zhang, J. Wu, M. N. Hedhili, and P. Wang, “A facile strategy for the fabrication of a bioinspired hydrophilic–superhydrophobic patterned surface for highly efficient fog-harvesting,” *J. Mater. Chem. A*, vol. 3, no. 37, pp. 18963–18969, 2015.
- [47] N. a Patankar, “Hydrophobicity of Surfaces with Cavities: Making Hydrophobic Substrates from Hydrophilic Materials?,” *J. Adhes. Sci. Technol.*, vol. 23, no. October, pp. 413–433, 2009.
- [48] G. Whyman and E. Bormashenko, “How to make the cassie wetting state stable?,” *Langmuir*, vol. 27, no. 13, pp. 8171–8176, 2011.
- [49] M. Nosonovsky and B. Bhushan, “Superhydrophobic surfaces

- and emerging applications: Non-adhesion, energy, green engineering," *Curr. Opin. Colloid Interface Sci.*, vol. 14, no. 4, pp. 270–280, 2009.
- [50] A. Tuteja, W. Choi, G. H. McKinley, R. E. Cohen, and M. F. Rubner, "Design Parameters for Superhydrophobicity and Superoleophobicity," *MRS Bull.*, vol. 33, no. 8, pp. 752–758, 2008.
 - [51] A. Tuteja *et al.*, "Designing Superoleophobic Surfaces," *Science (80-.)*, vol. 318, no. 5856, pp. 1618–1622, 2007.
 - [52] D. W. Bechert, M. Bruse, W. Hage, and R. Meyer, "Fluid Mechanics of Biological Surfaces and their Technological Application," *Naturwissenschaften*, vol. 87, no. 4, pp. 157–171, 2000.
 - [53] M. Sbragaglia and A. Prosperetti, "A note on the effective slip properties for microchannel flows with ultrahydrophobic surfaces," *Phys. Fluids*, vol. 19, no. 4, 2007.
 - [54] E. LAUGA and H. A. STONE, "Effective slip in pressure-driven Stokes flow," *J. Fluid Mech.*, vol. 489, p. S0022112003004695, 2003.
 - [55] A. M. J. Davis and E. Lauga, "Geometric transition in friction for flow over a bubble mattress," *Phys. Fluids*, vol. 21, no. 1, pp. 1–5, 2009.
 - [56] C. Cottin-Bizonne, B. Cross, A. Steinberger, and E. Charlaix, "Boundary slip on smooth hydrophobic surfaces: Intrinsic effects and possible artifacts," *Phys. Rev. Lett.*, 2005.
 - [57] J. Baudry, E. Charlaix, A. Tonck, and D. Mazuyer,

- “Experimental evidence for a large slip effect at a nonwetting fluid-solid interface,” *Langmuir*, 2001.
- [58] C. Neto, D. R. Evans, E. Bonaccorso, H.-J. Butt, and V. S. J. Craig, “Boundary slip in Newtonian liquids: a review of experimental studies,” *Reports Prog. Phys.*, 2005.
- [59] A. Maali and B. Bhushan, “Nanorheology and boundary slip in confined liquids using atomic force microscopy,” *J. Phys. Condens. Matter*, 2008.
- [60] E. LAUGA and H. A. STONE, “Effective slip in pressure-driven Stokes flow,” *J. Fluid Mech.*, 2003.
- [61] J. Ou, B. Perot, and J. P. Rothstein, “Laminar drag reduction in microchannels using ultrahydrophobic surfaces,” *Phys. Fluids*, 2004.
- [62] C. H. Choi and C. J. Kim, “Large slip of aqueous liquid flow over a nanoengineered superhydrophobic surface,” *Phys. Rev. Lett.*, 2006.
- [63] W.-E. Reif, “Squamation and ecology of sharks,” *Cour. Forsch.-Inst. Seckenb.*, 1985.
- [64] A. Dinkelacker, P. Nitschke-Kowsky, and W.-E. Reif, “On the possibility of drag reduction with the help of longitudinal ridges in the walls,” in *Turbulence Management and Relaminarisation: Proceedings of the IUTAM Symposium, Bangalore, India, 1987*, 1988.

- [65] B. Bhushan, "Biomimetics inspired surfaces for drag reduction and oleophobicity/philicity," *Beilstein J. Nanotechnol.*, vol. 2, pp. 66–84, 2011.
- [66] G. D. Bixler and B. Bhushan, "Fluid drag reduction and efficient self-cleaning with rice leaf and butterfly wing bioinspired surfaces," *Nanoscale*, vol. 5, no. 17, p. 7685, 2013.
- [67] A. Lee, M. W. Moon, H. Lim, W. D. Kim, and H. Y. Kim, "Water harvest via dewing," *Langmuir*, vol. 28, no. 27, pp. 10183–10191, 2012.
- [68] A. M. K. Seely, "International Association for Ecology Irregular Fog as a Water Source for Desert Dune Beetles Published by : Springer in cooperation with International Association for Ecology Stable URL : <http://www.jstor.org/stable/4215923> for Desert Dune Beetles," vol. 42, no. 2, pp. 213–227, 2016.
- [69] W. J. Hamilton, J. R. Henschel, and M. K. Seely, "Fog collection by Namib Desert beetles," *South African Journal of Science*, vol. 99, no. 3–4, p. 181, 2003.
- [70] F. T. Malik, R. M. Clement, D. T. Gethin, W. Krawszik, and A. R. Parker, "Nature's moisture harvesters: a comparative review," *Bioinspir. Biomim.*, vol. 9, no. 3, p. 31002, 2014.
- [71] C. Dietz, K. Rykaczewski, A. G. Fedorov, and Y. Joshi, "Visualization of droplet departure on a superhydrophobic surface and implications to heat transfer enhancement during dropwise condensation," *Appl. Phys. Lett.*, 2010.
- [72] J. B. Boreyko and C. H. Chen, "Vapor chambers with jumping-drop liquid return from superhydrophobic condensers," *Int. J. Heat Mass Transf.*, 2013.

- [73] T. Humplik, J. Lee, S. C. O'Hern, and B. A. Fellman..., "Nanostructured materials for water desalination," ..., 2011.
- [74] A. D. Khawaji, I. K. Kutubkhanah, and J. M. Wie, "Advances in seawater desalination technologies," *Desalination*, 2008.
- [75] A. Dehbi and S. Guentay, "A model for the performance of a vertical tube condenser in the presence of noncondensable gases," *Nucl. Eng. Des.*, 1997.
- [76] P. Dimitrakopoulos and J. J. L. Higdon, "On the gravitational displacement of three-dimensional fluid droplets from inclined solid surfaces," *J. Fluid Mech.*, 1999.
- [77] S. Kim and K. J. Kim, "Dropwise Condensation Modeling Suitable for Superhydrophobic Surfaces," *J. Heat Transfer*, 2011.
- [78] J. W. Rose, "On the mechanism of dropwise condensation," *Int. J. Heat Mass Transf.*, 1966.
- [79] Y. Liu, L. Moevius, X. Xu, T. Qian, J. M. Yeomans, and Z. Wang, "Pancake bouncing on superhydrophobic surfaces," no. June, pp. 1–5, 2014.
- [80] K. M. Wisdom, J. A. Watson, X. Qu, F. Liu, G. S. Watson, and C.-H. Chen, "Self-cleaning of superhydrophobic surfaces by self-propelled jumping condensate," *Proc. Natl. Acad. Sci.*, 2013.
- [81] J. Feng, Z. Qin, and S. Yao, "Factors affecting the spontaneous motion of condensate drops on superhydrophobic copper

- surfaces,” *Langmuir*, 2012.
- [82] K. Rykaczewski *et al.*, “How nanorough is rough enough to make a surface superhydrophobic during water condensation?,” *Soft Matter*, 2012.
- [83] J. B. Boreyko and C. H. Chen, “Self-propelled dropwise condensate on superhydrophobic surfaces,” *Phys. Rev. Lett.*, 2009.
- [84] K. K. Varanasi, M. Hsu, N. Bhate, W. Yang, and T. Deng, “Spatial control in the heterogeneous nucleation of water,” *Cit. Appl. Phys. Lett. Appl. Phys. Lett. Appl. Phys. Lett. Appl. Phys. Lett. J. Chem. Phys. Kinet. Heterog. Nucleation J. Chem. Phys. Appl. Phys. Lett.*, 2009.
- [85] C. Dorrer and J. R  he, “Some thoughts on superhydrophobic wetting,” *Soft Matter*, 2009.
- [86] K. Rykaczewski, A. T. Paxson, S. Anand, X. Chen, Z. Wang, and K. K. Varanasi, “Multimode multidrop serial coalescence effects during condensation on hierarchical superhydrophobic surfaces,” *Langmuir*, 2013.
- [87] R. Enright, N. Miljkovic, A. Al-Obeidi, C. V Thompson, and E. N. Wang, “Condensation on superhydrophobic surfaces: the role of local energy barriers and structure length scale,” *Langmuir*, 2012.
- [88] A. R. Parker and C. R. Lawrence, “Water capture by a desert beetle,” *Nature*, 2001.
- [89] H. Bai, L. Wang, J. Ju, R. Sun, Y. Zheng, and L. Jiang, “Efficient water collection on integrative bioinspired surfaces with star-

- shaped wettability patterns,” *Adv. Mater.*, vol. 26, no. 29, pp. 5025–5030, 2014.
- [90] Y. Hou *et al.*, “Recurrent Filmwise and Dropwise Condensation on a Beetle Mimetic,” no. 1, pp. 71–81, 2015.
- [91] X. Chen *et al.*, “Nanograssed micropyrnidal architectures for continuous dropwise condensation,” *Adv. Funct. Mater.*, 2011.
- [92] D. Beysens, “Dew nucleation and growth,” *Comptes Rendus Physique*. 2006.
- [93] F. Laermer and A. Schilp, “Method of anisotropically etching silicon,” 1996.
- [94] A. Bagolini, S. Ronchin, P. Bellutti, M. Chiste, M. Verotti, and N. P. Belfiore, “Fabrication of Novel MEMS Microgrippers by Deep Reactive Ion Etching With Metal Hard Mask,” *J. Microelectromechanical Syst.*, vol. 26, no. 4, pp. 926–934, 2017.
- [95] J. T. L. Thong, W. K. Choi, and C. W. Chong, “TMAH etching of silicon and the interaction of etching parameters,” *Sensors Actuators A Phys.*, 1997.
- [96] T. Kasai, B. Bhushan, G. Kulik, L. Barbieri, and P. Hoffmann, “Micro/nanotribological study of perfluorosilane SAMs for antistiction and low wear,” *J. Vac. Sci. Technol. B*, vol. 23, no. 3, p. 995, 2005.
- [97] B. Bhushan, “Nanotribology and nanomechanics in nano /

- biotechnology Nanotribology and nanomechanics in nano / biotechnology," *Society*, no. November 2009, pp. 1499–1537, 2008.
- [98] J. C. McDonald and G. M. Whitesides, "Poly(dimethylsiloxane) as a material for fabricating microfluidic devices," *Acc. Chem. Res.*, 2002.
- [99] Y. Xia and G. M. Whitesides, "Soft lithography," *Annu. Rev. Mater. Sci.*, 1998.
- [100] A. Bagolini, M. Boscardin, and M. Balucani, "Realization of 3D silicon structures using a DRIE technique," *Proc. 2015 18th AISEM Annu. Conf. AISEM 2015*, pp. 3–5, 2015.
- [101] M. Ghulinyan, R. Guider, G. Pucker, and L. Pavesi, "Monolithic whispering-gallery mode resonators with vertically coupled integrated bus waveguides," *IEEE Photonics Technol. Lett.*, vol. 23, no. 16, pp. 1166–1168, 2011.
- [102] M. Ghulinyan, D. Navarro-Urrios, A. Pitanti, A. Lui, G. Pucker, and L. Pavesi, "Whispering-gallery modes and light emission from a Si-nanocrystal-based single microdisk resonator.," *Opt. Express*, vol. 16, no. 17, pp. 13218–24, 2008.
- [103] M. Ghulinyan, A. Pitanti, and G. Pucker, "Whispering-gallery mode micro-kylix resonators," vol. 17, no. 11, pp. 1172–1176, 2009.
- [104] C. NEINHUIS, "Characterization and Distribution of Water-repellent, Self-cleaning Plant Surfaces," *Ann. Bot.*, vol. 79, no. 6, pp. 667–677, 1997.
- [105] E. Lepore and N. Pugno, "Superhydrophobic Polystyrene by

Direct Copy of a Lotus Leaf,” *Bionanoscience*, 2011.

- [106] E. Lepore, P. Faraldi, D. Bongini, L. Boarino, and N. Pugno, “Plasma and thermoforming treatments to tune the bio-inspired wettability of polystyrene,” *Compos. Part B Eng.*, 2012.
- [107] N. M. Pugno, “Towards a Spiderman suit: large invisible cables and self-cleaning releasable superadhesive materials,” *J. Phys. Condens. Matter*, 2007.
- [108] N. M. Pugno, “Mimicking lotus leaves for designing super-hydrophobic/hydrophilic and super-attractive/repulsive nanostructured hierarchical surfaces Nicola,” vol. 661, no. 2, pp. 1–9, 2007.
- [109] Y. Su, B. Ji, K. Zhang, H. Gao, Y. Huang, and K. Hwang, “Nano to micro structural hierarchy is crucial for stable superhydrophobic and water-repellent surfaces,” *Langmuir*, vol. 26, no. 7, pp. 4984–4989, 2010.
- [110] B. Bhushan, Y. C. Jung, and K. Koch, “Micro-, nano- and hierarchical structures for superhydrophobicity, self-cleaning and low adhesion,” *Philos. Trans. R. Soc. A Math. Phys. Eng. Sci.*, vol. 367, no. 1894, pp. 1631–1672, 2009.
- [111] B. Bhushan and Y. C. Jung, “Natural and biomimetic artificial surfaces for superhydrophobicity, self-cleaning, low adhesion, and drag reduction,” *Prog. Mater. Sci.*, vol. 56, no. 1, pp. 1–108, 2011.

-
- [112] K. Koch, A. Dommisse, and W. Barthlott, "Chemistry and crystal growth of plant wax tubules of lotus (*Nelumbo nucifera*) and nasturtium (*Tropaeolum majus*) leaves on technical substrates," *Cryst. Growth Des.*, 2006.
- [113] P. Papet *et al.*, "Pyramidal texturing of silicon solar cell with TMAH chemical anisotropic etching," *Sol. Energy Mater. Sol. Cells*, 2006.
- [114] A. F. Stalder, G. Kulik, D. Sage, L. Barbieri, and P. Hoffmann, "A snake-based approach to accurate determination of both contact points and contact angles," *Colloids Surfaces A Physicochem. Eng. Asp.*, vol. 286, no. 1–3, pp. 92–103, 2006.
- [115] D. Quéré, "Non-sticking drops," *Reports Prog. Phys.*, vol. 68, no. 11, pp. 2495–2532, 2005.
- [116] B. Bhushan and M. Nosonovsky, "The rose petal effect and the modes of superhydrophobicity," *Philos. Trans. R. Soc. A Math. Phys. Eng. Sci.*, vol. 368, no. 1929, pp. 4713–4728, 2010.
- [117] Y. Xiu, "Fabrication of surface micro- and nanostructures for superhydrophobic surfaces in electric and electronic applications," *ProQuest Diss. Theses*, p. 287, 2008.
- [118] X. Pu, G. Li, and H. Huang, "Preparation, anti-biofouling and drag-reduction properties of a biomimetic shark skin surface," *Biol. Open*, vol. 5, no. 4, pp. 389–396, 2016.
- [119] M. Ma and R. M. Hill, "Superhydrophobic surfaces," *Curr. Opin. Colloid Interface Sci.*, vol. 11, no. 4, pp. 193–202, 2006.
- [120] P. Luchini, F. Manzo, and A. Pozzi, "Resistance of a grooved surface to parallel flow and cross-flow," *J. Fluid Mech. Digit.*

Arch., vol. 228, no. 1991, p. 87, 1991.

- [121] J. Ou, B. Perot, and J. P. Rothstein, "Laminar drag reduction in microchannels using ultrahydrophobic surfaces," *Phys. Fluids*, vol. 16, no. 12, pp. 4635–4643, 2004.
- [122] G. D. Bixler and B. Bhushan, "Rice- and butterfly-wing effect inspired self-cleaning and low drag micro/nanopatterned surfaces in water, oil, and air flow," *Nanoscale*, vol. 6, no. 1, pp. 76–96, 2014.
- [123] B. Dean and B. Bhushan, "Shark-skin surfaces for fluid-drag reduction in turbulent flow: a review," *Philos. Trans. R. Soc. A Math. Phys. Eng. Sci.*, vol. 368, no. 1933, pp. 5737–5737, 2010.
- [124] A. Marmur, "The lotus effect: Superhydrophobicity and metastability," *Langmuir*, 2004.
- [125] H. Knight, "Lotus effect," *Engineer*. 2002.
- [126] A. Marmur, "From hygrophilic to superhydrophobic: Theoretical conditions for making high-contact-angle surfaces from low-contact-angle materials," *Langmuir*, vol. 24, no. 14, pp. 7573–7579, 2008.
- [127] L. Afferrante and G. Carbone, "Statistical theory of wetting of liquid drops on superhydrophobic randomly rough surfaces," *Phys. Rev. E - Stat. Nonlinear, Soft Matter Phys.*, vol. 92, no. 4, pp. 1–5, 2015.
- [128] P. Olin, S. B. Lindström, T. Pettersson, and L. Wågberg, "Water

- drop friction on superhydrophobic surfaces," *Langmuir*, vol. 29, no. 29, pp. 9079–9089, 2013.
- [129] "<http://mtlabportal.fbk.eu/SitePages/Home.aspx>."
- [130] A. F. Stalder, T. Melchior, M. Müller, D. Sage, T. Blu, and M. Unser, "Low-bond axisymmetric drop shape analysis for surface tension and contact angle measurements of sessile drops," *Colloids Surfaces A Physicochem. Eng. Asp.*, vol. 364, no. 1–3, pp. 72–81, 2010.
- [131] R. D. Blevins, *Applied fluid dynamic handbook*. New York: Van Nostrand Reinhold Co., 1984.
- [132] L. Feng *et al.*, "Super-Hydrophobic Surfaces: From Natural to Artificial," *Adv. Mater.*, vol. 14, no. 24, pp. 1857–1860, 2002.
- [133] D. Quéré, "Surface chemistry: Fakir droplets.," *Nat. Mater.*, vol. 1, no. 1, pp. 14–15, 2002.
- [134] E. B. Dussan, "On the ability of drips or bubblers to stick to non-horizontal surfaces of solids," *J. Fluid Mech.*, vol. 151, pp. 1–20, 1985.
- [135] AUSSILLOUS, PASCALE and D. QUERE, "Shapes of rolling liquid drops," *J. Fluid Mech*, vol. 512, pp. 133–151, 2004.
- [136] D. Richard and D. Quéré, "Viscous drops rolling on a tilted non-wettable solid," *Europhys. Lett.*, vol. 48, no. 3, pp. 286–291, 1999.
- [137] L. Mahadevan and Y. Pomeau, "Rolling droplets," *Phys. Fluids*, vol. 11, no. 9, pp. 2449–2453, 1999.
- [138] S. Suzuki *et al.*, "Slipping and Rolling Ratio of Sliding

Acceleration for a Water Droplet Sliding on Fluoroalkylsilane Coatings of Different Roughness,” *Chem. Lett.*, vol. 37, no. 1, pp. 58–59, 2008.

- [139] M. Sakai, J. H. Song, N. Yoshida, S. Suzuki, Y. Kameshima, and A. Nakajima, “Direct observation of internal fluidity in a water droplet during sliding on hydrophobic surfaces,” *Langmuir*, vol. 22, no. 11, pp. 4906–4909, 2006.
- [140] P. Hao, C. Lv, Z. Yao, and F. He, “Sliding behavior of water droplet on superhydrophobic surface,” *EPL (Europhysics Lett.)*, vol. 90, no. 6, p. 66003, 2010.
- [141] S. P. Thampi, R. Adhikari, and R. Govindarajan, “Do liquid drops roll or slide on inclined surfaces?,” *Langmuir*, vol. 29, no. 10, pp. 3339–3346, 2013.
- [142] H.-J. Butt, N. Gao, P. Papadopoulos, W. Steffen, M. Kappl, and R. Berger, “Energy Dissipation of Moving Drops on Superhydrophobic and Superoleophobic Surfaces,” *Langmuir*, vol. 33, no. 1, pp. 107–116, 2017.
- [143] M. Sbragaglia *et al.*, “Sliding drops across alternating hydrophobic and hydrophilic stripes,” *Phys. Rev. E - Stat. Nonlinear, Soft Matter Phys.*, vol. 89, no. 1, pp. 1–12, 2014.
- [144] S. Varagnolo *et al.*, “Tuning drop motion by chemical patterning of surfaces,” *Langmuir*, vol. 30, no. 9, pp. 2401–2409, 2014.
- [145] J.-J. Shu, J. Bin Melvin Teo, and W. Kong Chan, “Fluid Velocity

- Slip and Temperature Jump at a Solid Surface," *Appl. Mech. Rev.*, vol. 69, no. 2, p. 20801, 2017.
- [146] S. Daniel and M. K. Chaudhury, "Rectified Motion of Liquid Drops on Gradient Surfaces Induced by Vibration," *Langmuir*, no. 8, pp. 3404–3407, 2002.
- [147] A. Amirfazli and A. W. Neumann, "Status of the three-phase line tension: A review," *Advances in Colloid and Interface Science*. 2004.
- [148] A. Marmur, "Line tension effect on contact angles: Axisymmetric and cylindrical systems with rough or heterogeneous solid surfaces," *Colloids Surfaces A Physicochem. Eng. Asp.*, 1998.
- [149] W. J. Hamilton, J. R. Henschel, and M. K. Seely, "Fog collection by Namib Desert beetles," *South African Journal of Science*. 2003.
- [150] P. Varshney, S. Mohapatra, and A. Kumar, "Fabrication of Mechanically Stable Superhydrophobic Aluminium Surface with Excellent Self-Cleaning and Anti-Fogging Properties," *Biomimetics*, 2017.
- [151] D. Nanda, P. Varshney, M. Satapathy, S. S. Mohapatra, B. Bhushan, and A. Kumar, "Single step method to fabricate durable superliquiphobic coating on aluminum surface with self-cleaning and anti-fogging properties," *J. Colloid Interface Sci.*, 2017.
- [152] Z. C. Yuekun Lai, Yuxin Tang, Jiaojiao Gong, Dangguo Gong, Lifeng Chi, Changjian Lin, "Transparent superhydrophobic/superhydrophilic TiO₂- based coatings for

self-cleaning and anti-fogging,” *J. Mater. Chem.*, 2012.

- [153] Y. Chen *et al.*, “Transparent superhydrophobic/superhydrophilic coatings for self-cleaning and anti-fogging,” *Appl. Phys. Lett.*, 2012.
- [154] Q. Shang and Y. Zhou, “Fabrication of transparent superhydrophobic porous silica coating for self-cleaning and anti-fogging,” *Ceram. Int.*, 2016.
- [155] P. Vukusic and D. . Stavenga, “Physical methods for investigating structural colours in biological systems,” *J. R. Soc. Interface*, vol. 6, no. Suppl_2, pp. S133–S148, 2009.
- [156] S. Zhang and Y. Chen, “Nanofabrication and coloration study of artificial Morpho butterfly wings with aligned lamellae layers,” *Sci. Rep.*, vol. 5, p. 16637, 2015.
- [157] G. D. Bixler, A. Theiss, B. Bhushan, and S. C. Lee, “Anti-fouling properties of microstructured surfaces bio-inspired by rice leaves and butterfly wings,” *J. Colloid Interface Sci.*, vol. 419, pp. 114–133, 2014.
- [158] S. Ghio, G. Paternoster, R. Bartali, P. Belluti, M. Boscardin, and N. M. Pugno, “Fast and large area fabrication of hierarchical bioinspired superhydrophobic silicon surfaces,” *J. Eur. Ceram. Soc.*, 2015.
- [159] T. Young, “An Essay on the Cohesion of Fluids.” *Philosophica Transactions of the Royal Society of London*, pp. 65–87, 1805.

-
- [160] R. N. Wenzel, "Surface roughness and contact angle," *J. Phys. Colloid Chem.*, 1949.
- [161] B. He, N. A. Patankar, and J. Lee, "Multiple equilibrium droplet shapes and design criterion for rough hydrophobic surfaces," *Langmuir*, 2003.
- [162] M. Sun *et al.*, "Artificial lotus leaf by nanocasting," *Langmuir*, 2005.
- [163] A. Marmur, "Wetting on hydrophobic rough surfaces: To be heterogeneous or not to be?," *Langmuir*, 2003.
- [164] L. Afferrante and G. Carbone, "Microstructured superhydrorepellent surfaces: effect of drop pressure on fakir-state stability and apparent contact angles.," *J. Phys. Condens. Matter*, vol. 22, no. 32, p. 325107, 2010.
- [165] Y. T. Cheng and D. E. Rodak, "Is the lotus leaf superhydrophobic?," *Appl. Phys. Lett.*, 2005.
- [166] C. Della Volpe and S. Siboni, "Use, Abuse, Misuse and Proper Use of Contact Angles: A Critical Review," *Rev. Adhes. Adhes.*, vol. 3, no. 4, pp. 365–385, 2015.
- [167] M. Nosonovsky, "Multiscale roughness and stability of superhydrophobic biomimetic interfaces," *Langmuir*, 2007.
- [168] H. Belanger, T. Darmanin, E. Taffin de Givenchy, and F. Guittard, "Chemical and Physical Pathways for the Preparation of Superhydrophobic Surfaces and Relatrid Wetting Theories," *Chem. Rev.*, vol. 114, no. 5, pp. 2694–2716, 2014.
- [169] S. Ghio, G. Paternoster, R. Bartali, P. Belluti, M. Boscardin, and

- N. M. Pugno, "Fast and large area fabrication of hierarchical bioinspired superhydrophobic silicon surfaces," *J. Eur. Ceram. Soc.*, vol. 36, no. 9, pp. 2363–2369, 2015.
- [170] B. Roman and J. Bico, "Elasto-capillarity: Deforming an elastic structure with a liquid droplet," *J. Phys. Condens. Matter*, vol. 22, no. 49, 2010.
- [171] T. Darmanin and F. Guittard, "Superhydrophobic and superoleophobic properties in nature," *Mater. Today*, vol. 18, no. 5, pp. 273–285, 2015.
- [172] O. Tricinci, T. Terencio, B. Mazzolai, N. M. Pugno, F. Greco, and V. Mattoli, "3D Micropatterned Surface Inspired by *Salvinia molesta* via Direct Laser Lithography," *ACS Appl. Mater. Interfaces*, vol. 7, no. 46, pp. 25560–25567, 2015.
- [173] J. W. M. Bush, D. L. Hu, and M. Prakash, *The Integument of Water-walking Arthropods: Form and Function*, vol. 34, no. 7, 2007.
- [174] N. Verplanck, Y. Coffinier, V. Thomy, and R. Boukherroub, "Wettability switching techniques on superhydrophobic surfaces," *Nanoscale Res. Lett.*, vol. 2, no. 12, pp. 577–596, 2007.
- [175] R. Pericet-Cámara, A. Best, H. J. Butt, and E. Bonaccorso, "Effect of capillary pressure and surface tension on the deformation of elastic surfaces by sessile liquid microdrops: An experimental investigation," *Langmuir*, vol. 24, no. 19, pp. 10565–10568, 2008.

- [176] Y. S. Yu and Y. P. Zhao, "Deformation of PDMS membrane and microcantilever by a water droplet: Comparison between Mooney-Rivlin and linear elastic constitutive models," *J. Colloid Interface Sci.*, vol. 332, no. 2, pp. 467–476, 2009.
- [177] M. Miwa, A. Nakajima, A. Fujishima, K. Hashimoto, and T. Watanabe, "Effects of the surface roughness on sliding angles of water droplets on superhydrophobic surfaces," *Langmuir*, 2000.
- [178] Y. Li, D. Quéré, C. Lv, and Q. Zheng, "Monostable superrepellent materials," *Proc. Natl. Acad. Sci.*, vol. 114, no. 13, pp. 3387–3392, 2017.